High aspect-ratio MEMS devices for the next generation of THz/MHz passive components

Giuseppe Fiorentino

High aspect ratio MEMS devices for the next generation of THz/MHz passive components

PROEFSCHRIFT

ter verkrijging van de graad van doctor
aan de Technische Universiteit Delft,
op gezag van de Rector Magnificus Prof. ir. K. C. A. M. Luyben,
voorzitter van het College voor Promoties,
in het openbaar te verdedigen

op dinsdag 16 Juni 2015 om 15.00 uur

door

Giuseppe Fiorentino

Physicist, Naples University Federico II
geboren te Napels

Dit proefschrift is goedgekeurd door de promotor:
Prof. dr. P.M. Sarro

Samenstelling promotiecommissie:

Rector Magnificus	voorzitter	Delft University of Technology
Prof. dr. P. M. Sarro	promotor	Delft University of Technology
Prof. dr. A. Neto		Delft University of Technology
Prof. dr. P. French		Delft University of Technology
Prof. dr. G. Gerini		Technical University of Eindhoven
Prof. dr. A. Freni		University of Florence
Dr. G. Pandraud		Delft University of Technology
Dr. Jean-Francois Lampin		IEMN, Lille

Giuseppe Fiorentino,
High aspect ratio MEMS devices for the next generation of THz/MHz passive components,
Ph.D. Thesis Delft University of Technology,
with summary in Dutch.

The work presented in this thesis has been performed at TU-Delft and financed by STW under the project code 10709.

Keywords: Artificial Dielectric Layer, Terahertz Antennas, High dielectric constant, Atomic Layer Deposition, Carbon nanotubes, 3D integration, supercapacitors, electrical characterization.

ISBN: 978-94-6186-478-9

Design of the cover page by Giuseppe Fiorentino.
Published by: Uitgeverij BOXPress, 's-Hertogenbosch

To my family and to who believes in friendship

Table of contents

1

Introduction

1.1 Thesis motivations

The author believes that a famous sentence can well illustrate the spirit of this work:

> *"Give me a lever long enough, and I will move the world."*
> — Archimedes of Syracuse

Archimedes perceived that the need of a specific tool or, more in general, a specific technology, could determine the accomplishment of complex tasks otherwise unachievable.

Historically, the development of new tools and technologies has determined incredible advances in sciences. A suitable example is represented by the microscope, that since its first applications by Antoni van Leeuwenhoek (1632 - 1723), gave priceless contribution to medicine, biology, metallurgy and much more.

Moving closer to our field, the invention of the transistor in 1947 by Shockley, Brattain and Bardeen has been the starting point for the development of an entire new generation of electronic devices. It is impossible to enumerate the amount of tools and different technologies developed starting from this simple device, but we can definitively state that nothing as the science of electronics has changed so much our lifestyle in the last 60 years.

The enormous (social, industrial, economical) potential of IC technology has been the main force that motivated companies, research centers and

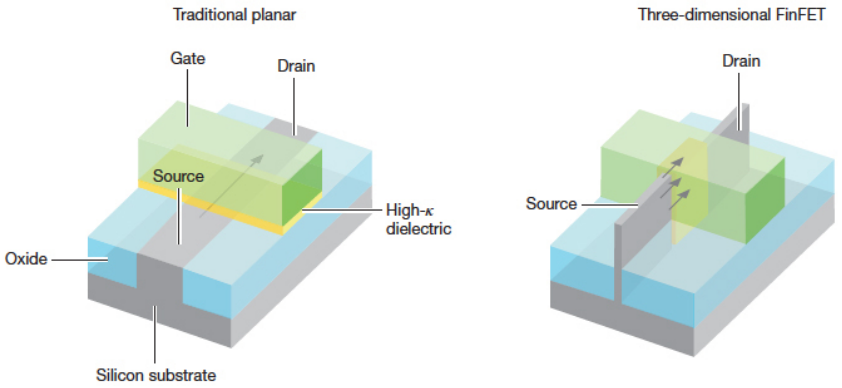

Figure 1.1: FinFET transistors possess a much wider gate dielectric layer (surrounding the fin shape) than do MOSFET transistors and can use multiple fins [1].

scientists towards the fabrication of new, low cost and better performing electronic devices. This continuous growth can be effectively summarized by the Moore's law, according to which the number of transistors in an integrated ciruit will double every 2 years.

Although true for many years, it is now clear that the route of the scaling can not be pursued anymore. New paradigms have to be explored to overcome intrinsic material physical limitations causing electrical and thermal leakages, easy breakdown a.o., and fabrication tool limitations, lithography resolution above all.

As already shown by Intel [1], new transistor architectures, such as the Three-dimensional FinFET (see Fig. 1.1), represent a feasible solution to overcome some of the above mentioned issues .

These serious limitations affect not only digital components, but also, and in a more stringent way, analog devices, particularly passives. Indeed, in such class of components, the performance are mainly driven by physical parameters that can not be easily scaled. For example, the performance of a capacitor can be enhanced, in a first approximation, either using new materials with higher dielectric constant (k) value, or reducing its thickness. However, as already shown in 2009 by Banerjee [2], on chip large capacitance can be achieved also using new 3D high aspect-ratio capacitor architectures in combination with special deposition techniques, such as Atomic Layer Deposition (ALD). As shown for the FinFET transistor, the new 3D high aspect-ratio capacitor architecture opened a viable route to overcome typical capacitor limitations [3].

Other passive devices that strongly suffer from intrinsic physical limitations are high frequency (THz or sub-THz) antennas. The need for higher frequencies working communication links, as well as the fascinating scenario opened by the terahertz sensing potential, are currently driving the research for highly efficient, low losses and miniaturized planar antennas. The fabrication of such (integrated) components working at these frequencies has to deal with the extremely large losses typical of the conventional materials (dielectric and silicon substrates) used in Complementary metal-oxide-semiconductor (CMOS) technology. Therefore, it is clear that to overcome the intrinsic limitations of currently used configurations and materials, new engineering approaches have to be explored.

In this thesis the advantages of conventional CMOS techniques in combination with specific functionalities and characteristics provided by nanotechnologies are exploited for the realization of innovative passive devices. Although working in completely different frequency range, these components can both fulfill a fundamental role in providing efficient solutions in their respective field of application.

1.2 Planar antennas for mm and sub-mm wavelengths

Nowadays, planar antennas working at mm or sub-mm wavelength are quite attractive in applications such as short-range communication [4], automotive radars [5] and, more recently, imaging radars [6] (see Fig. 1.2,1.3,1.4). Despite the advanced design of these systems, RF front-ends and antenna are still realized on two different substrates and then connected. Since all the electronic is realized by means of Monolithic Microwave Integrated Circuits (MMIC), an ideal solution would be to fabricate the antenna directly on the same substrate. This architecture has many benefits such as the reduced request of space, lower integration costs and less weight. Miniaturization of such components has an enormous advantage in terms of functionalities as well, since it strongly reduces the losses (conduction losses given by the finite conductivity of conventional materials). Moreover, considering that losses increase with frequency, the miniaturization becomes especially relevant in the growing field of THz sensing.

From the fabrication point of view, the integration of such antennas in an IC process presents also other advantages. By exploiting the extremely high resolution of conventional lithographic system, thin and complex antenna structures can be effectively realized. Moreover, the high reproducibility in accuracy of the IC lithography allows the fabrication of large antenna arrays directly on a single wafer, thus further reducing the overall system

Figure 1.2: An antenna in package designed to work in around 60 GHz [4].

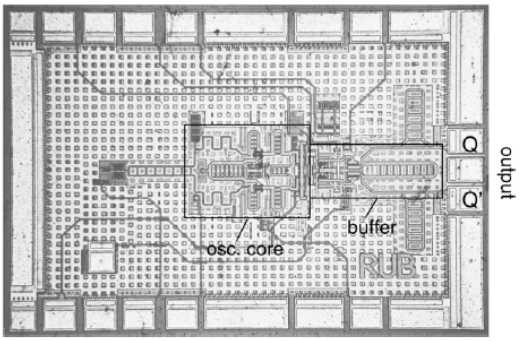

Figure 1.3: A micrograph of a Voltage Controlled Oscillator at 77 GHz [5].

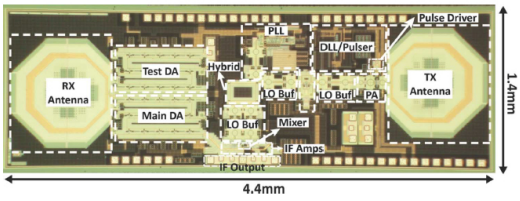

Figure 1.4: A chip micrograph of the antenna receiver at 90 GHz [6].

costs.

However, the fabrication of planar antennas still presents many fundamental issues, such as the radiation efficiency. A typical planar antenna fabricated in a IC process is first patterned on a metal substrate with conventional lithographic/etching techniques and, eventually, is suspended on a membrane by releasing the substrate (usually silicon). This architecture, however, offers a very poor efficiency, since the antenna radiates its energy 50% in the positive z direction and 50% in the negative z direction. Half of the power send to or received from this device is then lost. Especially at very high frequency (i.e. Terahertz) where the power generated is already very limited and the losses are higher, the antenna efficiency decreases dramatically.

A solution to this limitation, would be the insertion of an artificially engineered layer with high dielectric constant (so called Artificial Dielectric Layer) on top of the antenna. The fabrication of a new type of Artificial Dielectric Layers by using CMOS compatible technology represents one of the main topic of this dissertation.

1.3 Miniaturized solid state supercapacitors

As mentioned in the first section, also other passive devices, such as capacitors, can greatly benefit from new design strategies. Due to the growing demand for high performance, light and portable electronic devices (such as mobile phones) and wireless sensor networks, there is the need for small, powerful and reliable supercapacitors directly integrated in the system.

Nowadays these supercapacitors are realized in many different ways, generally combining a conventional design with high surface-area electrodes to enhance the charge storage area. Usually, as in the case of electrochemical supercapacitors, this solution implies the use of porous nanostructured electrodes, mostly based on carbon [7–9].

However, as explained in more detail in Chapter 6, the use of electrochemical supercapacitors is still problematic for many applications. In fact, these components are usually bulky and realized with hazardous liquid materials, that also poses issues to their integration in proximity of electronics. For this reason, it would be interesting to realize fully solid state supercapacitors, with a small footprint and fabricated with IC compatible materials, so to benefit from available large volume manufacturing capabilities. Recently, it has been shown that with these devices very high capacitance can be indeed achieved but their fabrication process is far from being scalable [7, 8, 10–13]. .

In the last two decades, by using a technique called Atomic Layer Deposition (now also adopted in many CMOS fabrication processes) very thin,

conformal and high quality solid dielectric thin layers, such as Aluminum Oxide and Hafnium Oxide, can be achieved. If used in combination with high aspect ratio conductive nanostructures (realized on a large scale) and a second conductive and conformal counter electrode, this would allow the realization of fully solid state dielectric supercapacitors. With the introduction of a new generation of commercial PECVD tools (such as the Aixtron reactors), wafer-scale fabrication of nanostructures, such as carbon nanotubes, can be achieved and at a relatively low temperature ($\leq 500\,^{\circ}\mathrm{C}$). The high surface area offered by carbon nanotubes bundles can be effectively used as frame to build a high aspect-ratio solid-state supercapacitor. By coating the tubes surface with a dielectric and a conductive layer, the large surface area provided by the CNT bundles can be exploited for the capacitance enhancement.

1.4 Thesis Outline

This thesis can be considered as divided in two parts. In the first one, the fabrication of an Artificial Dielectric Layer (ADL) for antennas working in the Terahertz frequency range will be presented. In Chapter 2, the reader will be introduced to the main fields of application of THz sensing. Particular relevance will be given to the sources and detectors developed during the last decades. In Chapter 3 we introduce an artificially engineered material, fabricated by conventional silicon processing techniques, that enhances the dielectric constant of a conventional dielectric layer. Due to the extreme difficulties in the measurements of the material properties in the THz frequency range, different techniques need to be used to fully characterize both conventional and engineered materials. For this reason, two completely different approaches have been used to study the optical properties of the ADL and the results are reported in Chapter 4. In Chapter 5, an alternative material is introduced as dielectric layer in the ADL fabrication, to further explore the properties of CMOS compatible materials in the THz frequency range.

While the first part of this work is related to the realm of the very high frequencies, the second part is related to the lower frequency range (up to 1 MHz). In the sixth chapter a new concept of supercapacitors, based on the coating of high aspect ratio carbon nanotubes forest with a solid dielectric layer is presented. This device shows a very high capacitance density while keeping its characteristic capacitive impedance up to 1 MHz. Similar devices [14] cease to work as they are supposed to, at much lower frequencies (10-20kHz). In Chapter 7, a complete electrical analysis and modelling is carried out, to illustrate the performance of the presented capacitor and its working principle. Due to the innovative fabrication process required to achieve a

large electrode surface area, a detailed analysis of the coating process of the Carbon nanotubes is reported as well. Finally, the conclusions and suggestions for the future work are presented in Chapter 8.

2

Terahertz sensing technology

In this chapter Terahertz (THz) radiation for sensing application is introduced. The most interesting phenomena related to its generation and sensing are presented and two of the most important application areas, i.e. space science and life science, are illustrated. A brief overview of THz sources and detectors currently available is given, trying to indicate the major breakthroughs in the generation and detection of this radiation. The challenges in the fabrication and use of THz devices, especially antennas, will be discussed and a particular class of engineered materials, called Artificial Dielectric Layers (ADL), will be be proposed as possible solution to overcome some of the antenna limitations.

2.1 Terahertz radiation

Historically, the term terahertz refers to the wavelength range between $1000 - 100\mu$m (300 GHz - 3 THz) [15]. Due to the fact that terahertz radiation begins at a wavelength that goes from one millimeter to shorter wavelengths, it is sometimes referred as the submillimeter band.

Falling between infrared and microwave radiation, THz radiation shares some properties with each of them. Like the infrared and microwave radiation, its propagation follows a line of sight and due to the low energy it is non-ionizing. Like microwaves, terahertz radiation can penetrate a large number of non-conducting materials (i.e. clothing, paper, cardboard, wood, plastic and ceramics).

As its photon energy spans from 1.2 to 12.4 meV (see Fig. 2.1), THz radiation is related to a wide amount of natural phenomena, going from the molecular vibrational modes of many molecules [16, 17] to the emission of cold interstellar gas and dust clouds and to the universe very first light. THz frequency range remains one of the least tapped regions of the electromagnetic spectrum, being for long time a prerogative of astronomers, chemists, planetery and space scientists to detect and catalog lines for lightweight molecules.

2.1.1 Terahertz radiation sensing for space application

It is correct to state that the whole Universe bathes in terahertz energy, although only a fairly little part of it is revealed and cataloged [15].

The wavelength covered by the THz spectrum corresponds to a photon energy between $1.2 - 12.4$ meV or to an equivalent black body of $14 - 140$K.

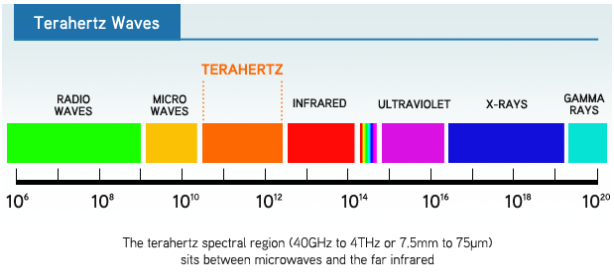

Figure 2.1: The electromagnetic spectrum from radio frequencies to gamma rays. Terahertz radiation bridges the gap between the microwaves and the infrared, covering a very wide portion of the whole spectrum

.

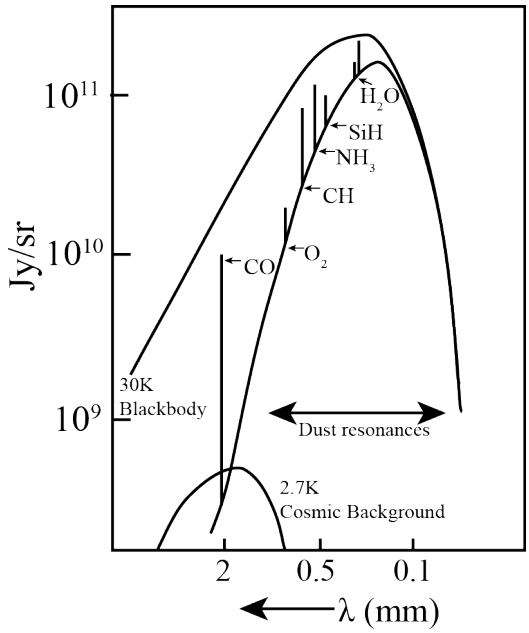

Figure 2.2: Radiated energy versus wavelength showing 30-K blackbody, a typical interstellar dust and some key molecular line emissions in the submillimter range [15].

As showed in Fig. 2.2, the emissions from interstellar clouds, light and heavy molecules lie between these energies. Recently, it has been estimated that almost 40000 individual spectral lines can be distinguished in this frequency region, and most of them are still not related to a precise chemical compound [15].

Probably, one of the most outstanding results concerning the universe observation in THz frequency is the mapping of the cosmic microwave background (CMB) radiation. This radiation is assumed to be the thermal radiation remnant of the Universe formation event, the Big Bang. Its photons are the oldest light observable, the first to escape from the plasma of electrons, protons and photons that populated our universe for $3.79 \cdot 10^5$ years after the Big Bang.

The newest set of images of the CMB radiation are coming from the Planck ESA satellite, launched in 2009 and deactivated in 2013. This satellite covered the visible sky in 9 different bands, from 20 to 857 GHz, giving a map of the CMB radiation with unprecedent resolution (see Fig. 2.3).

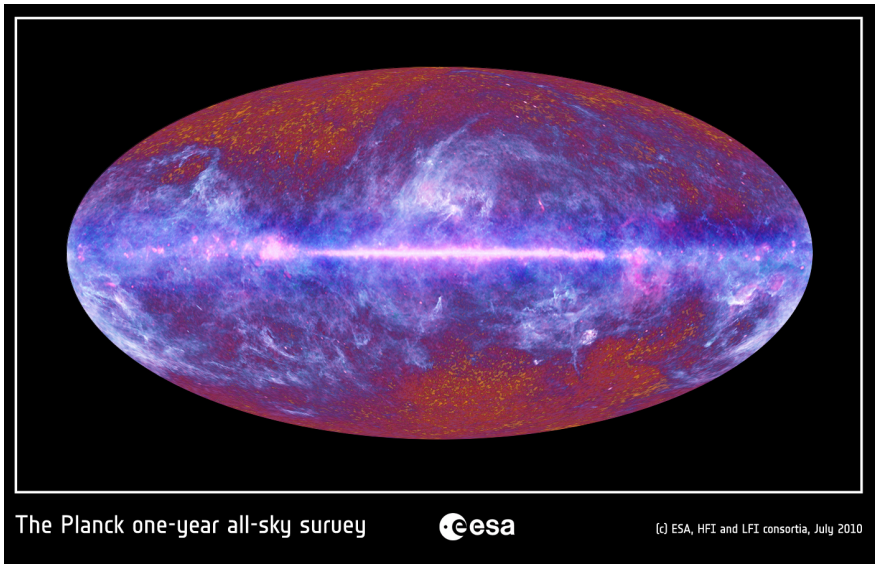

Figure 2.3: Planck view of the microwave sky, covering frequencies from 30 GHz to 857 GHz. (Image: ESA/LFI and HFI Consortia).

Thanks to this result, it has been possible to determine with more precision some fundamental cosmological parameters such as the age of the universe (now pointed at 13.81 billions of years) and the universe expansion rate (67.7 (Km/s)/Mpc).

Many molecules, e.g., water, oxygen, carbon monoxide, nitrogen, to name a few, can be probed in the terahertz regime. However, the water present in the Earth atmosphere generates strong absorptions, making any ground-based observation impossible (except from very few high-altitude observatory, aircrafts, or balloon platforms). For this reason, dedicated THz space telescopes have been realized, such as the Herschel ESA telescope. As opposed to the Planck telescope, designed to create a map of the observable universe, Herschel is designed to study specific sources, such as galaxies and stars formation with particular attention to the relative interaction with the interstellar dust. The satellite contains different instruments, that cover the wavelength range from 55 to 625 μm. It is correct to state that THz astronomy research pushed engineers and physicists towards the realization of source and detectors with outstanding performances. Part of these achievements will be shown in the next sections, with particular attention to the sources and detectors.

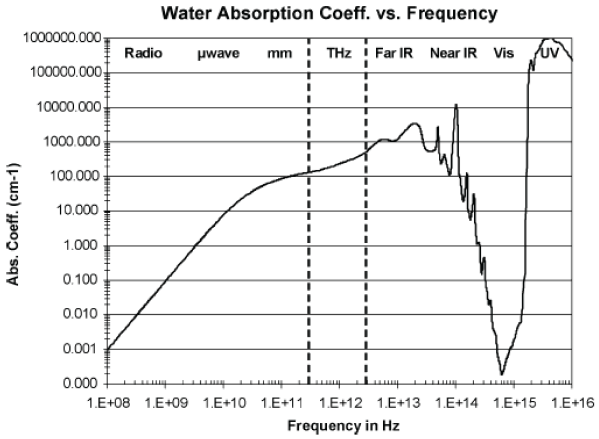

Figure 2.4: Absorption coefficient of triply deionized water at 292 K between 100 MHz and the ultraviolet (UV) [16].

2.1.2 Terahertz technology for life science

The very low energy levels of THz radiation are particularly suited for applications concerning life sciences. Indeed, with energy bounded between 1 and 12 meV, terahertz photons can not damage cells or tissues (no resonant absorption), while giving only generalized thermal effects. Consequently, applications to life science could be envisioned [16]. Some of the benefits offered by THz sensing are :

- THz radiation is non-ionizing.
- Less scatter than IR/optical due to longer wavelengths.
- Time-domain imaging uses amplitude and information in reflection or transmission, which can be used to generate 3D images.

However, as clearly shown by decades of research, the absorption of THz photons in water represents a serious issue towards the use of the radiation as sensing for *in vivo* or *in vitro* organisms. Indeed, as shown in Fig. 2.4, the broad absorption loss of THz energy in pure deionized liquid water is so strong that can compete with the best black body.

The absorption law follows the Debye relaxation model (spherical rotation in a viscous media) in polar liquids at least up to 1 THz [16]. By assuming a common Beer's law power penetration dependency in depth, $P_{Out}/P_{in} = e^{-\alpha x}$, the absorption is higher than 2000 dB/cm at 3 THz. Any

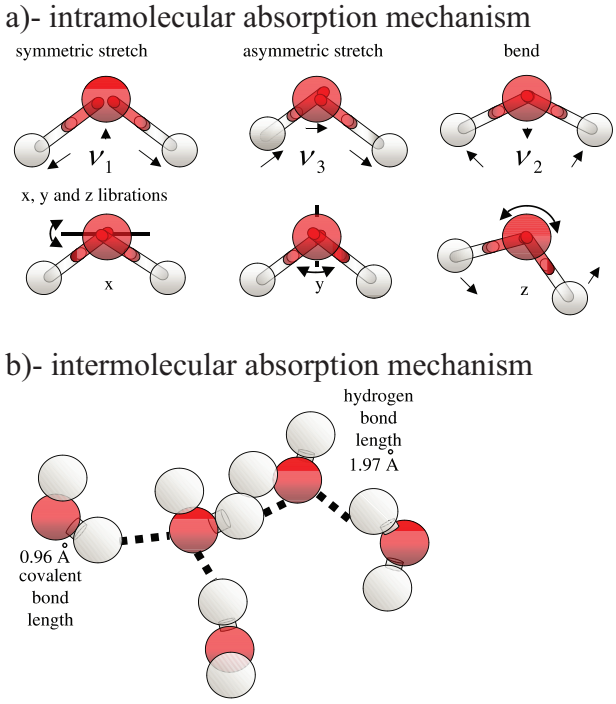

Figure 2.5: (a) The main vibration modes in water. (b) A schematic diagram to illustrate the differences between intra (a) and inter-molecular (b) bonding in water [18].

organic tissue with a relevant percentage of water would then be impenetrable to this radiation.

The vibration and libration modes of water molecules are illustrated in Fig. 2.5 [18]. Water molecules may vibrate in a number of ways. In the gas phase, the vibrations involve combinations of the symmetric stretch (ν_1), asymmetric stretch (ν_3) and bending (ν_2) of the covalent bonds. The ν_1 , ν_3 and ν_2 vibrations lie in the mid- to far-infrared.

In water, the infrared and Raman spectra are complicated due to vibrational overtones and combinations with librations. Hydrogen bondings also complicate the situation. Since these bonds are much weaker than the covalent (intra-molecular) bonds, their bondlengths are much longer (1.97 Å versus 0.96 Å), resulting in modes at THz frequencies. This is illustrated in Fig. 2.5(b).

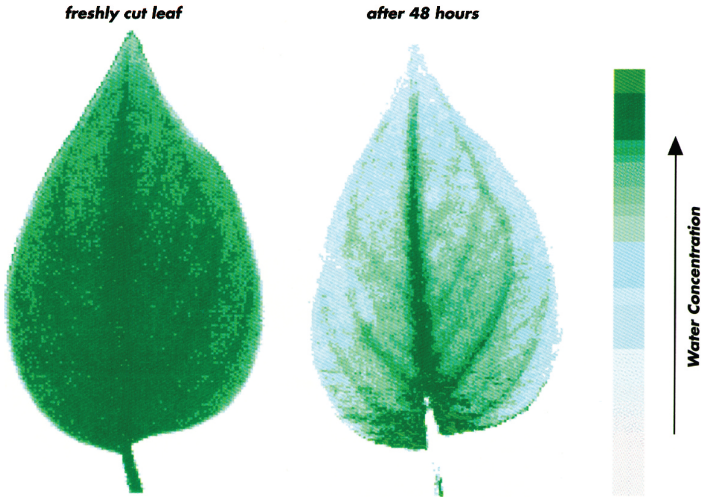

Figure 2.6: Left : Terahertz image of a fresh leaf. The attenuation of THz radiation through the leaf is mainly due to the water inside the leaf. Right : THz image of the same leaf after 48 hours. The water has evaporated from the leaf, except from the stem [19].

However, single-molecule vibration modes in the Terahertz absorption spectra of the water can not explain all the observed features. Particularly, as shown by [20], it is more likely that the observed Debye relaxation phenomena observed have to be attributed to collective motion of atoms. Rønne et al. [20] show that the mechanisms of absorption is related to different response time of *weakly* hydrogen bonded and *strongly* hydrogen bonded water molecules clusters. While weakly bonded clusters can reorient under the action of the electromagnetic field with a small activation energy (resulting in a fast relaxation time), the more strongly hydrogen bonded molecules have to wait until the hydrogen bonds become weak enough so they can orient (resulting in a slower relaxation time).

As mentioned above, due to the exceptionally high absorption losses at terahertz frequencies, the penetration through biological materials of any substantial thickness is impossible. However, the same high absorption coefficient that limits penetration in tissue also promotes extreme contrast between substances with lower or higher degree of water saturation.

This property has proven advantageous in the examination of water uptake and distribution in plants [21] (see Fig. 2.6), as well as in the severity of burns on necrotic skin samples [22] and in tumor morphology [23] (see

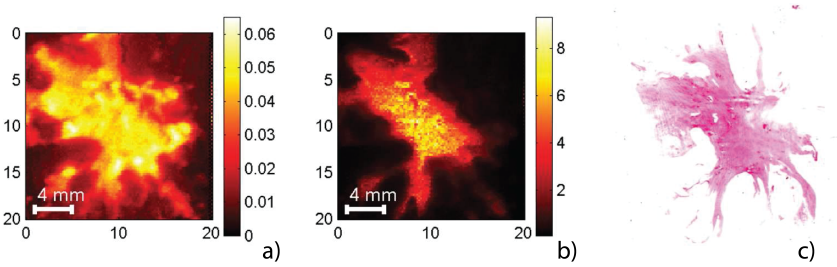

Figure 2.7: This figure shows two terahertz images generated using the maximum of the reflected pulse (E_{max} in a) and the ratio between maximum and minimum of the reflected pulse (E_{max}/E_{min} in b). In the E_{max} image all the tissue is shown, tumor with surrounding adipose tissue. In E_{max}/E_{min} only the tumor is visible and correlated well with the tumor shown in the histology image (c). [24].

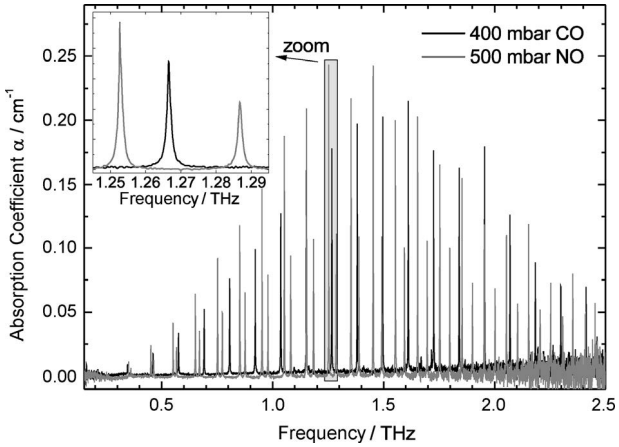

Figure 2.8: Measured absorption coefficient for carbon monoxide (CO) and nitric oxide (NO).

Fig. 2.7).

As many emission and absorption lines correspondent to rotational and vibrational excitations of gas molecules are in this frequency band, gas spectroscopy also represents an important THz sensing application.

Usually the absorption spectra of gases are detected in a Time Domain Spectroscopy system (see Section 2.2 and Section 2.3), by placing a cell with a certain analyte in the path of a THz beam.

An example is shown in Fig. 2.8, where the measured absorption coefficient for carbon monoxide (CO) and nitric oxide (NO) molecules show a wide set of rotational transitions. By evaluating the measured center frequency, a particular gas can be identified. The detection sensitivity of such systems is mainly determined by the SNR of the system, the absorption coefficient of the sample, and the absorption length within the measurement cell. Depending on these parameters, concentrations in the ppm range have been detected [17] .

2.2 Terahertz sources

The most difficult component to realize in the submillimeter-wave band is an efficient terahertz source. There are several fundamental explanations for this. Conventional electronic solid-state sources based on semiconductors, such as oscillators and amplifiers, are limited by reactive parasitics or transit times that cause high-frequency rolloff, or they have simple resistive losses that tend to dominate the device impedance [15, 25–27]. Tube sources suffer from simple physical scaling problems, metallic losses, and the need for extremely high fields (both magnetic and electric), as well as high current densities [28–32]. Optical sources, like solid-state lasers, must operate at very low energy levels (meV), comparable to that of the lattice phonons, although cryogenic cooling can partially solve this problem. More successful techniques for generating terahertz power have come from frequency conversion, either up from millimeter wavelengths, or down from the optical or IR [33–35]. Many approaches have been tried. The most successful milliwatt sources are laser (far-IR to submillimeter) pumping or reactive multiplication through $GaAs$ Schottky diode (see Fig. 2.9) [15].

Terahertz sources can be basically divided in :

- Upconverters : the power is generated starting from lower frequencies multiplied through a non-linear process.
- Downconverters : frequency downconverter, mainly from otpical frequencies.

2.2.1 Upconverters

The need for narrow-band compact solid-state THz sources is being driven, at least partially, by space applications such as FIRST/Herschel, which cannot fly bulky power-consuming lasers or short-lived very-heavy kilovolt-driven tube sources. In order to get power from the W band (75-110 GHz) to terahertz frequencies through solid-state upconversion, several octaves must be covered. The most efficient terahertz sources are, therefore, composed of

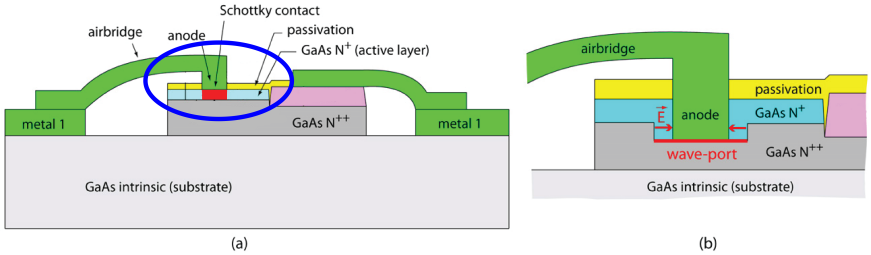

Figure 2.9: Schematic of a planar Schottky diode with zoom (blue ellipse) in of the metal-semiconductor junction [36].

in-chains lower order multipliers. Nowadays, sources based on multipliers mostly use planar $GaAs$ Schottky barrier diodes [15, 35, 37]. Multiplier chains driven by amplified sources at 100 GHz can reach 1200 GHz with 75 μW at room temperature and over 250 μW when operate in the presence of a controlled cooling system (with temperature around 120 K) [38, 39].

More recently, by using a room temperature device based on chain $GaAs$ amplifier, the group of Maestrini and Siegel [40] realized a tunable terahertz source working between 2.48 and 2.75 THz. This device can deliver 18 μW at 2.58 THz. When used in combination with microbolometers, these devices can be used for sub-mm heterodyne detection in space missions.

2.2.2 Downconverters

The most diffused technique for generating terahertz energy is nowadays the downconversion from the optical regime. Two principal methods are known to produce both narrow band and broad-band energy. The first technique, photomixing, makes use of offset-frequency-locked CW lasers focused on a small area of a photoconductor with very short lifetime (less than 1 ps). This pulse generates carriers between closely spaced (1 μm) electrodes printed on the semiconductor.

The laser induced photocarriers short the gap producing a photocurrent, that is coupled to an RF circuit or antenna that radiates the terahertz energy. The resulting power is narrow-band, phase lockable, and readily tuned over the full terahertz band by slightly shifting the optical frequency of one of the two lasers [15, 41, 42].

A second technique for producing terahertz energy from downconversion is based on using a short pulse (femtosecond) optical laser to illuminate a gap between closely spaced electrodes on a photoconductor generating carriers, which are then accelerated in an applied field ($\leq$ 100 V). The resulting current surge, which is coupled to an RF antenna, has frequency

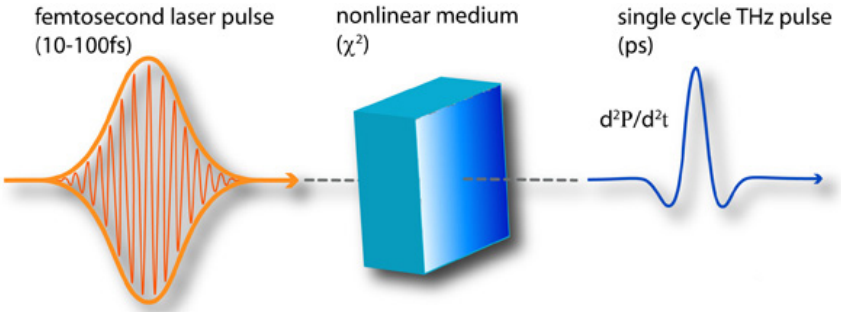

Figure 2.10: A nonlinear polarization P is generated by the incoming field E with frequency ω, mediated by the second order nonlinear susceptibility χ^2. When continuous laser beam hits the crystal, a small voltage is measured across it. Conversely, when very short laser pulses are applied, a very short polarization is produced that is of the duration of the pulse and has the form of the pulse envelope. By Maxwell's equations, the polarization P will act as a source term, radiating an electromagnetic pulse in the far field. For laser pulses that last less than a picosecond, the result will be a very short electromagnetic pulse with frequency in the terahertz range [43].

components in the terahertz.

The same output spectrum can be obtained by applying short laser pulses to a crystal with a large second-order susceptibility (χ^2) like zinc telluride (see Fig. 2.10). Since the higher order susceptibility terms are indicative of nonlinear response, the resulting mixing of the Fourier components produces a time-varying polarization with typical terahertz frequencies. The power is radiated by antennas printed on the crystal (or the photoconductor), with a band varying from 0.2 to 2 THz (depending on the type of pulse) and often very low power levels (10^{-9} to 10^{-6} Watts).

2.3 Terahertz detectors

While research on terahertz sources has to face and solve still many theoretical and technological limitations and issues, very sensitive terahertz detectors have been developed during the last decades. Near-quantum-limited detectors that can measure broad-band and extremely narrow-band signals up to or exceeding 1 THz have already been reported [44–46]. The main differences between detection at terahertz frequencies and detection at shorter wavelengths lie in the low photon energies and in the rather large Airy disk diameter (hundreds of micrometers). The first condition, for example, implies that ambient background thermal noise almost always

dominates naturally emitted narrow-band signals and either cryogenic cooling of the detector elements or long-integration-time radiometric techniques is required.

It is possible to differentiate between two large categories of THz detectors, i.e. *heterodyne* detectors and *direct* detectors.

2.3.1 Heterodyne detectors

Heterodyne detectors are based on the use of semiconductors [15] and are usually dedicated to the study of Earth and planetary science. In these systems, a local oscillator source at the THz frequency of interest is mixed with the received signal. The downconverted signal is then amplified and measured. Typically, the downconversion is achieved by using single Schottky diode mixer [46–49]. With this technology, a planar Schottky-diode mixer has been operated successfully at 2.5 THz for sensing applications in space [50]. In general, these devices are used when high spectral resolution is required.

By using cryogenic cooling is possible to achieve higher sensitivity in heterodyne superconductor detectors, as demonstrated by Weinreb and Kerr already in 1973 [51]. Among the different superconductive structures, the most widely used is the superconductor-insulator-superconductor (SIS) tunnel junction mixer (used for application from 100 to 1200 GHz). In this device, the current flow mechanism relies on the photon-assisted tunneling process (see Fig. 2.11) discovered by Dayem and Martin [52], [53].

2.3.2 Direct detectors

As opposed to *heterodyne* detectors, *direct* detectors are usually used when there is no need for very high spectral resolution. The main technologies that have been developed during the last years involve conventional bolometers based on direct thermal absorption and change of resistivity (see Fig. 2.12 a)), microbolometers that use an antenna to couple power to a small thermally absorbing region or Golay cells based on thermal absorption in a gas-filled chamber (see Fig. 2.12b) [55–58].

An outstanding example of THz detectors that combine SIS technology and bolometers is the Heterodyne Instrument for the Far-Infrared (HIFI) spectrometer on the ESA satellite Herschel. It is a very high resolution spectrometer and the first space instrument using superconductive heterodyne receivers, covering a frequency range from 480 GHz to 1500 GHz. The HIFI instrument provides also detectors for higher frequencies, from 1410 to 1910 GHz, realized with hot electron bolometer technology.

Starting from a W-band synthesizer module delivering 100 mW to 150 mW at room temperature, the frequency was multiplied to reach the de-

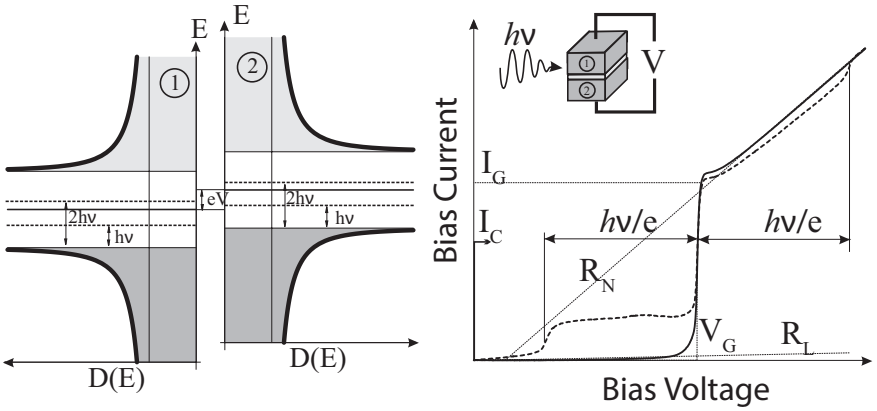

Figure 2.11: Energy diagram and current-voltage curve of a superconductor-insulator-superconductor junction (SIS). The typical geometry of a SIS junction is shown in the insert. Dashed line is current-voltage of SIS junction when submm radiation is applied [54].

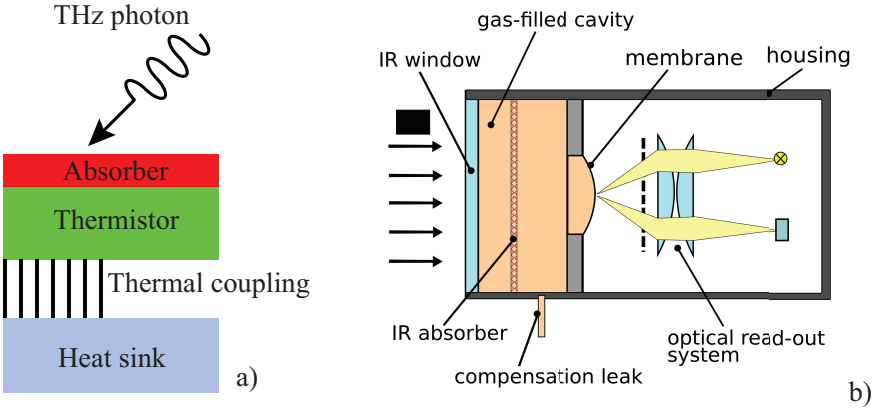

Figure 2.12: a) A typical bolometer architecture. An absorber element (in red) is connected to a thermistor, a resistor element that changes its resistivity with the temperature. A heat sink is connected to the sensitive area to dissipate the loaded heat. b) A Golay cell. The incident radiation is absorbed by the gas contained in an isolated chamber. One side of this chamber consists of a thin membrane, part of an optical read-out system. The radiation absorption induces gas heating and a consequent increase of the gas pressure. The membrane deforms consequently, resulting in a variation of the membrane shape measured by a photodiode.

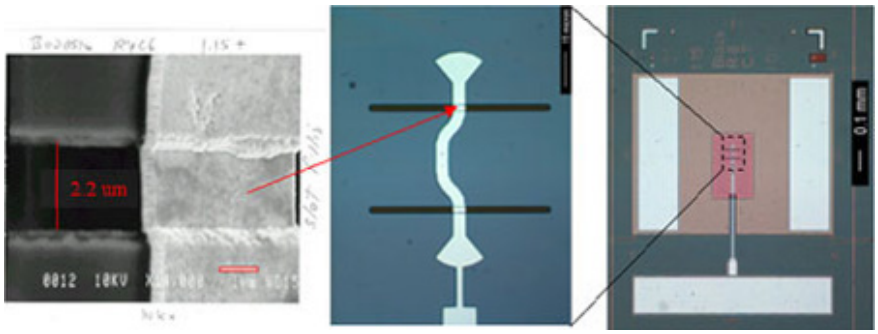

Figure 2.13: The Superconductor-Insulator-Superconductor device with an expanded view of the mixer circuit. This device were used in the 480 - 1250 GHz observations and were fabricated by a consortium between NASA and ESA (Image credit: ESA/Herschel).

sired frequencies. Unlike the W-band power modules, the frequency multipliers were passively cooled to 120 K to significantly increase the output power of the highest frequency local oscillator chains. Among the reason of this improvement, we can cite the enhanced $GaAs$ mobility due to the low temperature, thus improving the intrinsic performance of each diode; the reduced ohmic losses associated with the waveguides; the on-chip matching circuits due to the decrease in phonon scattering [36]. The final performance achieved by using these novel architectures of power-combined frequency multipliers at submillimeter-wavelengths leads to generated power between 40 and 100 μW in the different detection bands.

2.4 Present challenges

Due to the increase in the wireless data traffic of the last few years, there has been an increasing demand for much higher speed communication links. Following this trend, wireless Terabit-per-second (Tbps) links are expected to become a reality within a few years. In this context, the very large bandwidth provided by the THz band opens opportunities for applications which demand ultra-high data rates, both for conventional networking (5G Cellular Networks, Terabit Wireless Local Area Networks) and short distance communication.

However, such applications are still far from being realized, mainly due to fundamental limitations such as the intense absorption spectra of the Earth atmosphere in the THz frequencies. Indeed, as shown in previous sections, water represents the most striking limiting component, with thou-

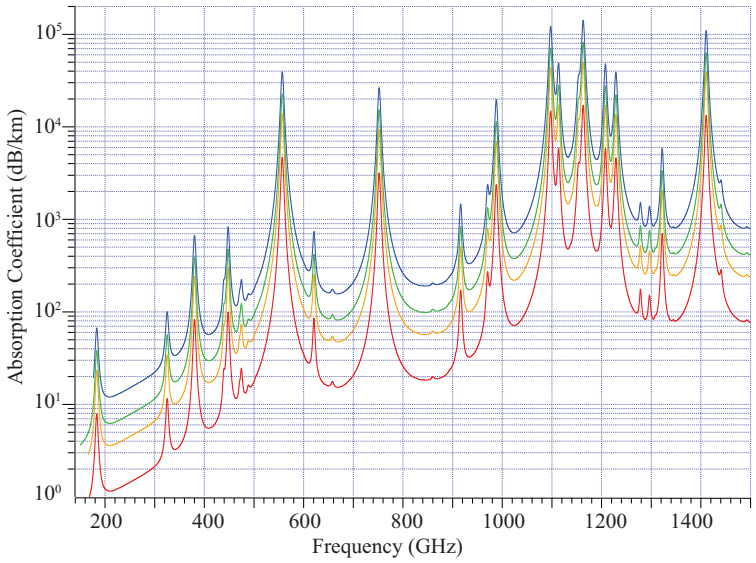

Figure 2.14: Calculated absorption coefficient values of water vapor at 296K for 10 (red), 30 (orange), 50 (green), and 90 (blue) percent relative humidity [59].

sands of absorption lines, due to its complex rotational and vibrational spectra (see Fig. 2.14). Moreover, as also shown in the previous sections, the lack of high power sources and easy-to-fabricate detectors partially confine the use of this radiation to its lower boundary (i.e. below 500 GHz).

Despite these limitations, the fabrication of transceivers working in the lower THz domain has been recently accomplished by exploiting silicon-germanium ($SiGe$) and silicon BiCMOS/CMOS technologies. A major advantage of $SiGe$ CMOS is the use of multi-level metallization with low-loss transmission lines to build integrated passive elements, such as antennas, for a real system-on-a-chip technology platform. By using this technology, cut-off frequencies above 300 GHz have been demonstrated [60], although the use of such devices remains confined to imaging application where a large bandwidth is not necessary.

However, in $SiGe$ and silicon technologies major challenges that still need to be addressed are the intrinsic device speed limitation for the cut-off frequency and the maximum operating frequency placed at $200 - 300$ GHz.

Particularly in the case of CMOS technology, the presence of unwanted parasitics and other (i.e. conductive) loss mechanisms, are serious limiting factors [61].

One of the main (passive) THz component that requires a careful design and fabrication to avoid any unwanted losses are the antennas. CMOS integrated planar antennas are becoming an important design aspect of low-cost millimeter-wave systems since they remove the loss and cost associated with transitions in and out of the silicon chip [62, 63]. Planar antennas, compared to the complex and bulky three dimensional antenna geometries, are not only light weight and simple to fabricate, but they can also be designed to achieve very high performance. This renders them attractive not only for commercial low-cost mobile devices, but also for the high-end applications such as radar, satellite communication and space.

Many on-chip antennas have been already proposed, but most of them present high loss and low gain due to the low metal conductivity or the proximity of a very close ground plane to the radiating structure [64]. Moreover, the physical properties of the substrate on which the antenna is printed (permittivity and thickness) can cause further performance reduction. When printed on electrically thin ($\lambda/10$, where λ is the central working frequency of the antenna) dielectric substrates, antennas are matched over narrow bandwidths and radiate half power in the upper space and half power in the lower space. A practical approach to increase the front-to-back-ratio and the matching bandwidth is to use a dense and electrically thick ($\lambda/4$) dielectric slab. However, by increasing the thickness and the permittivity of the substrate unwanted surface waves can be triggered, causing further loss in the radiated power and degrading the radiation patterns.

The above highlighted problems are the motivation for the design and realization of of innovative planar antenna solutions, which can be fabricated using commercial processes, e.g., printed circuit board (PCB) or monolithic microwave integrated circuit (MMIC) technology. The first part of this dissertation is centered around the design of planar electromagnetically engineered superstrates, which not only exhibit high surface-wave efficiency over a broad frequency band, but also results in a enhanced front-to-back ratio for an antenna radiating in their presence.

3

A 300 GHz CMOS-technology based antenna/ADL system

In this chapter the effectiveness of artificial dielectric layers (ADL) to enhance the front-to-back ratio of planar antennas at 300 GHz is demonstrated. The ADL working principle is described, highlighting the advantages offered when used in combination with planar antennas. A new antenna/ADL device working at 300 GHz is then presented. By means of numerical simulations, the relevant parameters of the antenna (gain, reflection coefficient, front-to-back radiation ratio) with and without the ADL are extracted. Finally, an antenna/ADL prototype is fabricated using a newly developed CMOS compatible process.

3.1 Artificial Dielectric Layers

Artificial dielectrics (ADs) were proposed in late 1940 to design low-loss and light-weight lens antennas [65]. An AD consists of non-resonant periodic metallic structures embedded in a host material in order to increase its equivalent relative permittivity. The working principle of AD is that the propagation of an incident wave in a uniform dielectric material is delayed when the material contains small periodic metallic inclusions arranged in a particular scheme (see Fig. 3.1). The field scattered by the metallic inclusions, when added to the incident field, creates an effective equivalent delay [65–67], resulting in a higher equivalent dielectric constant.

ADL-based integrated solutions have been recently proposed for THz frequency domain spectroscopy [68] and THz anti-reflection coating [69]. In [70], the authors have exploited the concept of ADL in commercial CMOS technology to reduce the size of on-chip passive components. This has finally led to a significant reduction of losses, since the losses are directly proportional to the device physical dimensions.

Planarity, integrability, and ability to reduce the physical size of integrated components, render ADL a promising candidate for the antenna design. It is known that in the case of planar and integrated antennas, a good front-to-back radiation ratio (10 dB) can be achieved using a dense dielectric slab of thickness in order of quarter wavelength $\lambda_d/4$. Here λ_d is the wavelength inside the dielectric (with dielectric constant ϵ) at the central frequency of matching bandwidth. However, the surface wave efficiency of these antennas is quite poor and the 3-dB radiation beam width of the far field radiation pattern can be severely affected [71, 72].

3.2 Advantages of using Artificial Dielectric Layer (ADL) in antenna design

A non-planar solution to the low radiation efficiency issue is to use a dielectric lens with matching layers. The matching layers are used to minimize the losses due to multiple reflections inside the lens [73–75]. A planar solution that can bypass a dielectric lens was presented in [63]. In this work, the antenna is printed on an additional low-loss quartz wafer, glued on the chip to increase the distance form the ground plane, and aperture-coupled to the feed structure. The antenna achieved a peak efficiency of 60%. The 40% loss in efficiency is due to the excitation of the substrate modes. Furthermore, a strict alignment accuracy is required between the antenna and the on-chip feed lines. A similar kind of solution has also been proposed for on-chip antenna arrays by the same authors in [62].

In [66], it was shown that ADLs can be exploited to increase the front-

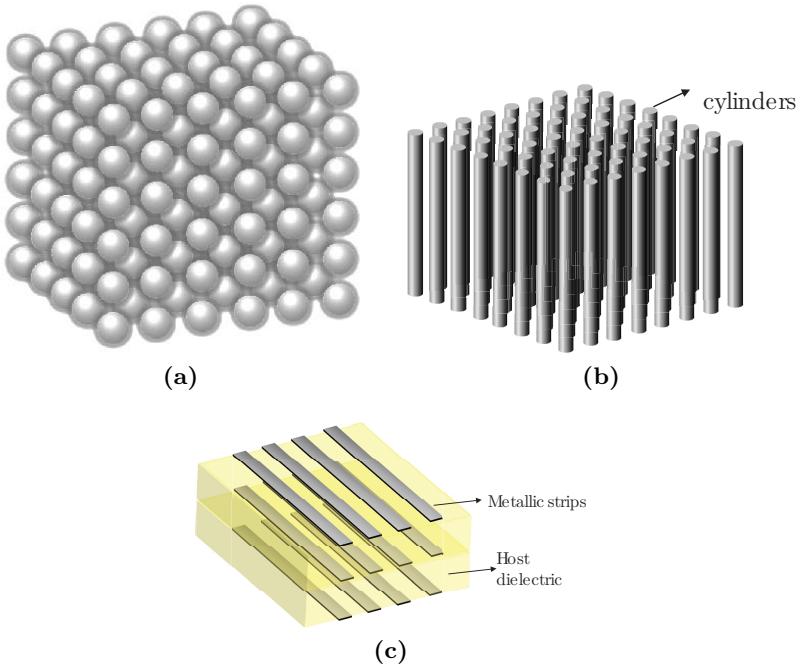

Figure 3.1: Artificial dielectric layer embedded in a host dielectric. (a) Three dimensional sphere and (b) cylinders and (c) planar two dimensional metallic strips.

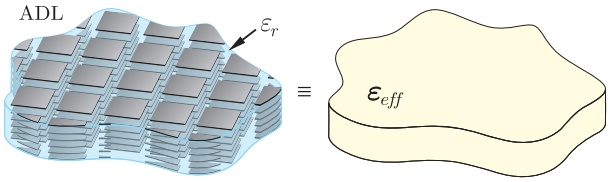

Figure 3.2: Artificial dielectric layers embedded in a host medium with relative permittivity ε_r to realize an equivalent effective homogenous medium. Each layer is composed by an array of electrically small patches.

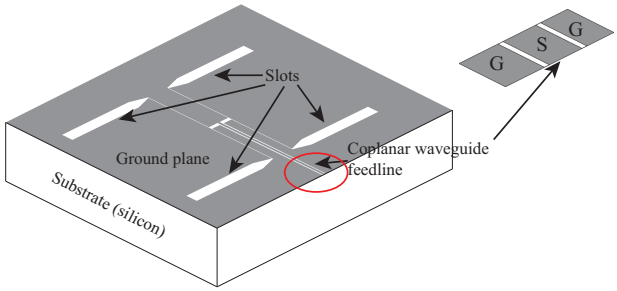

Figure 3.3: Double slot antenna schematic. In the inset (red ellipse), the feeding line given by the coplanar waveguide is shown. S and G indicate the signal and ground, respectively.

to-back radiation ratio of planar antennas printed on a electrically thin dielectric slabs, in X-band. Thanks to the enhanced anisotropic properties, virtually no power loss in surface waves was observed. To ensure that no surface waves are excited, the characterization of the dispersion properties of ADL slabs in [76, 77] can be used, which is based on an analytical study of the spectral Green's function of these slabs.

In this chapter a 0.3 THz version of the double-slot antenna enhanced by an ADL superstrate proposed in [66] is presented. In Fig. 3.3 and 3.4 a schematic view of the structure is shown. A coplanar waveguide is here used as feeding line (see 3.3 inset) of the radiating slots. On top of the antenna, the ADL is then realized by alternate depositions of metal (aluminum) and dielectric (silicon oxide). The non-resonant patches composing the ADL, as depicted in Fig. 3.2, are hosted by an electrically thin silicon dioxide slab with relative permittivity $\varepsilon_{\text{host}} = 4$. Such value is increased by the presence of the ADLs to an equivalent relative dielectric constant $\varepsilon_{\text{eff}} = 32$, for normally incident waves. The ADL superstrate does not suffer from surface-wave losses. This is due to the fact that, in virtue of the anisotropy, the waves incident at small angles do not feel the larger effective dielectric constant, which would otherwise induce surface-wave modes. The superstrate and the antenna have been fabricated using a specifically developed IC based process and the silicon on the back side of the antenna has been etched off. Measured results are reported and compared with simulations.

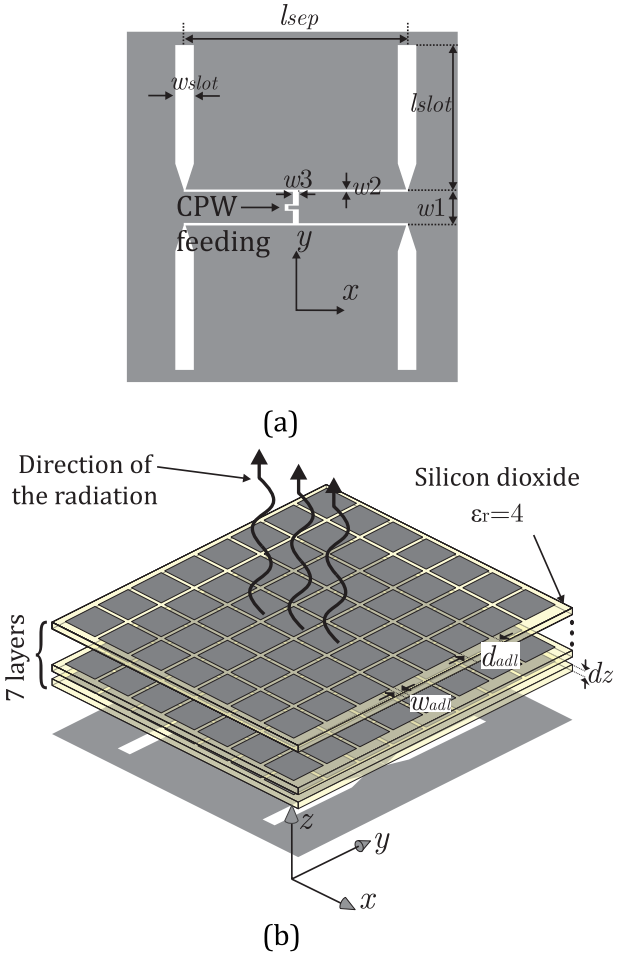

Figure 3.4: (a) Double slot antenna fed by CPW lines and (b) 3D view of the antenna/ADL device (only 3 layers of the ADL stack are shown here).

Table 3.1: Physical Dimensions of the Antenna and ADL in μm

l_{slot}	l_{sep}	w_{slot}	w_1	w_2	w_3	d_{adl}	d_z	w_{adl}
195	300	25	46.5	1	8	90	5	10

3.3 Enhancement of dielectric constant using Artificial Dielectric Layer

The double-slot antenna is shown in Fig. 3.4(a), with a co-planar waveguide (CPW) feed. The antenna is loaded by artificial dielectrics superstrate placed at a distance of 5 μm above the antenna (see Fig. 3.4(b)). The dimensions of the antenna and the ADL are summarized in Tab. 3.1. The geometrical parameter have been selected so that the antenna is matched around the frequency of 300 GHz and the ADL exhibit an effective dielectric constant of 32 for the waves which are incident along the broadside direction. The effective enhancement of the host material by the ADL, in an infinite homogeneous dielectric environment, is reported in Fig. 3.5. The equivalent dielectric constant is calculated using the formulation described in [76, 77]. This graph shows that for a transverse magnetic (TM) incident wave, the equivalent permittivity of the enhanced medium approaches the one of the host substrate, i.e. 4, when the angle of incidence tends to 90 degrees. However, in case of transverse electric (TE) incidence, the dielectric constant tends to a higher value. The effects of this property were investigated in [77], where the dispersion characteristic of these slabs were described in detail by means of an analytical method.

The total height of the host silicon dioxide substrate is 35μm, which is electrically equivalent to $\lambda_d/14$. Within this slab, an ADL consisting of a stack of 7 layers, each separated by 5μm along the z-axis (see Fig. 3.4(b)), is realized. This results in a slab with effective height of $0.2\lambda_{eff}$ at 0.3 THz. A starting point for the design has been obtained by following the guidelines outlined in [66] and by using the tools described in [76, 77]. While this allows for a fast selection of quasi-optimal geometrical parameter, the final structure with the details of the feed has been fine tuned using a commercial EM solver.

3.3.1 Simulated Results

Figure 3.6 shows the simulated reflection coefficient with and without metal losses. As expected, the finite conductivity case (aluminum with conductivity $\sigma = 2.6 \times 10^7$ S/m) shows a broader bandwidth of the reflection

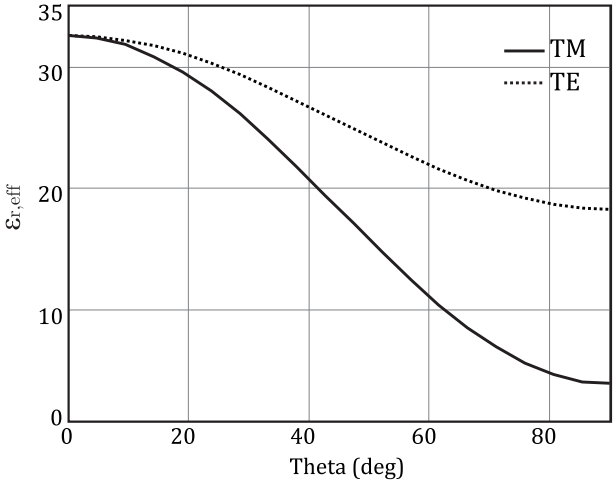

Figure 3.5: The value of the the equivalent dielectric constant for scanning angles 0 to 90 degrees.

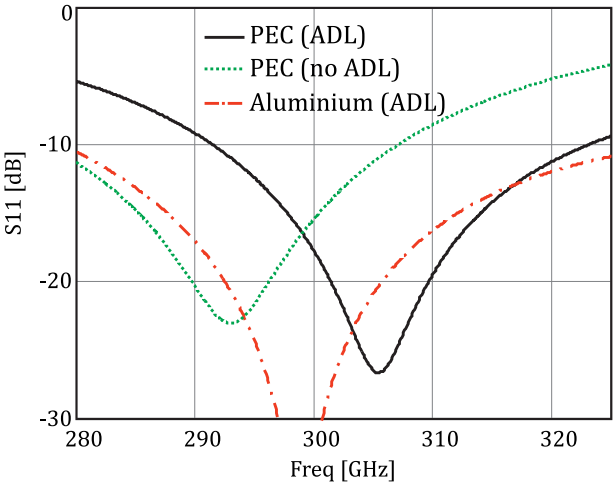

Figure 3.6: Simulated reflection coefficient for a perfect electric conductor (i.e. zero electrical resistance) with (black solid) and without the ADL (green dots). The same coefficient is then calculated for a real metal (i.e. finite conductivity)

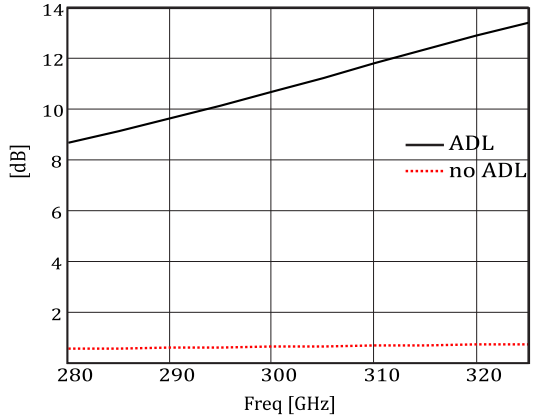

Figure 3.7: Simulated front to back radiation ratio.

coefficient, due to ohmic losses. In the fabricated device, the metal thickness of the antenna layer is 2μm, while it is 0.5μm for the ADL patches. In both cases, the thickness is well above the skin depth at 0.3 THz. The -10 dB impedance matching bandwidth of the antenna ranges from 295 till 320 GHz (8% relative bandwidth). This value is typical of a resonant double-slot antenna and not reduced by the presence of the ADL, which has broadband and non-resonant characteristics.

In order to quantify the advantage of using the ADL inclusions, a reference double-slot antenna loaded only with a 35μm slab of silicon dioxide has been designed and manufactured. This antenna without ADL is also matched at around 300 GHz, as shown in Fig. 3.6.

The simulated normalized radiation patterns of the antenna, with and without ADL, are reported in Fig. 3.10, at 305 GHz. It can be observed that the antenna with the ADL has a front-to-back ratio greater than 10 dB. On the contrary, the antenna in absence of the ADL, loaded only by an electrically thin slab, exhibits a front-to-back ratio lower than 1 dB, since almost equal power is radiated in the two half spaces above and below the slot ground plane. Figure 3.7 shows the variation of the front-to-back ratio as a function of the frequency for the two antennas. The values for the ADL loaded antenna are higher than 10 dB over the whole matching bandwidth, and linearly increasing with frequency, due to the increasing electrical thickness of the ADL slab. Instead, the reference antenna has an almost frequency independent front-to-back ratio of about 0.7 dB.

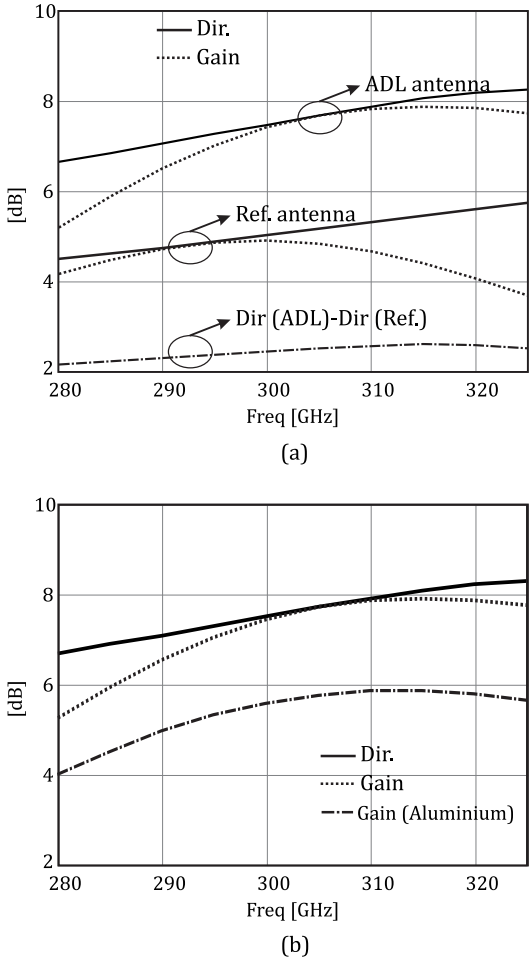

Figure 3.8: Simulated antenna efficiency: (a) comparison with a reference antenna (i.e., without ADL) for a PEC case; (b) evaluation of ohmic losses using aluminum as metal for the antenna layer and the feeding line.

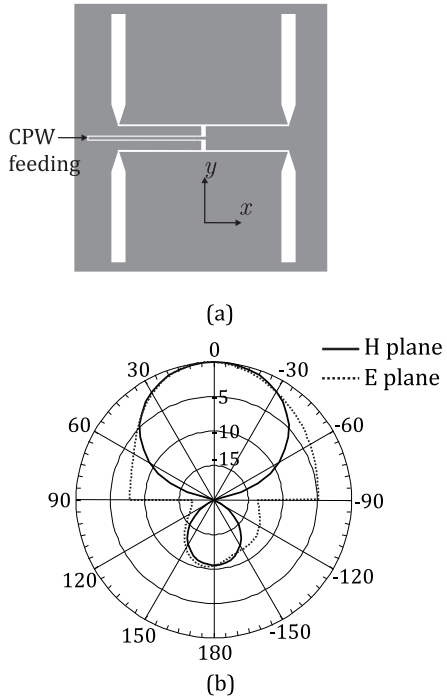

Figure 3.9: (a) Schematic drawing of the extended of CPW line to feed the antenna. (b) The simulated radiation pattern in E and H-plane after inclusion of extended CPW.

In Fig. 3.8(a), the gain and directivity for the antenna with and without ADL using a metal with zero resistivity, also called perfect electric conductor (PEC), is shown. This plot shows that the difference between the gain and directivity around the central frequency of the matching bandwidth for both antennas is negligible within the accuracy of the simulations. This means that surface waves, which in principle are allowed to propagate (TM_0 mode), are essentially not excited. The gain presented here also includes the mismatch losses. In the same graph, the comparison between the directivity of the two antenna reveals an enhancement of 2.2-2.6 dB for the ADL loaded antenna. This improvement occurs without compromising on pattern purity or surface wave efficiency. Note that, in simulations, surface wave losses are too low to be estimated accurately despite the use of absorbing boundary conditions along the lateral directions (x and y).

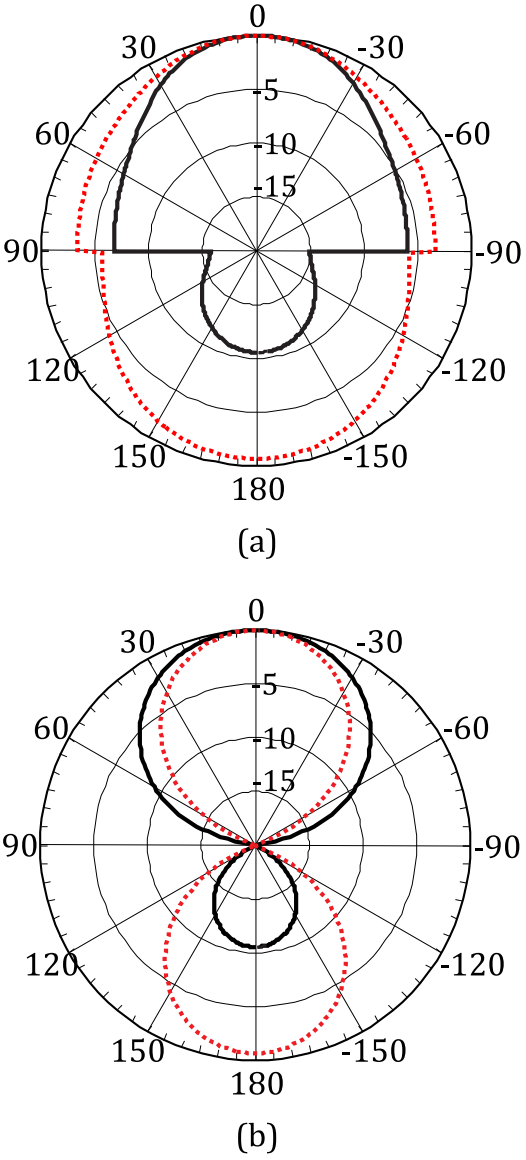

Figure 3.10: Simulated (normalized) (a) *E*-plane and (b) *H*-plane radiation pattern in dB at 305 GHz. The solid and the dashed line represent the antenna with and without the ADL, respectively.

The simulated gain obtained in the case of lossy metal (aluminum) for the ADL loaded antenna is shown in Fig.3.8(b). It is 2 dB lower than the PEC case. By means of numerical simulation, it has been estimated that the ohmic losses accounts for 1.3 dB within the slot antenna and 0.7 dB within the ADL.

To feed the double-slot antenna, a 50 Ohm CPW line is used to carry the input power to the center of the H-slot from one side of the antenna, as depicted in Fig. 3.9(a). Such a feed introduces an asymmetry in the E-plane pattern (see Fig. 3.9(b)), due to the coupling of the CPW lines with the parallel lines forming the H-slot and with the ADL. However, this asymmetry is kept to a minimum, by designing the CPW as small as possible (strip width of 5 μm and slot width of 2 μm) so that the field is confined in a small region and couples weakly with the antenna structure. On the other hand, such approach comes at the cost of increased ohmic losses due to strong currents in the inner conductor of the CPW. The total losses due to the 860μm long line are estimated to be about 2 dB.

3.4 Fabrication using CMOS-technology

The combined antenna/ADL structure has been built using as substrate a high resistivity (3.5k$\Omega\cdot$ cm) n-type silicon (Si) wafer with 100 mm diameter, (100) crystal orientation and thickness of $500 \pm 25\mu$m. The use of a high-resistivity substrate is mandatory since the charge carriers cause high losses and these losses are even higher in the THz frequency range [78, 79]. The main steps of the fabrication process are shown in Fig. 3.11.

The devices are realized using a 20×20 mm die design (see Fig. 3.12), giving a total of 12 dies on a single wafer. To avoid any cross talk between antennas, the distance of radiating structures has been chosen to be larger than 4 mm. The die is divided in three parts: the antenna/ADL structure on the top left side, the reference antenna on the top right part and the test structures (used for de-embedding the feed lines) on the bottom part (see Fig. 3.12). Further details about the test structures are given in the next section.

In Fig. 3.13, a schematic cross section of the device is shown. The structure can be divided in three main sections: the feeding/pads section (A), the feed transition (B) and the antenna/ADL one (C). A 2 mm long CPW with uniform width connects the contact-pads, where the wafer probe is landed, to a transition region. In this latter region, the CPW lines undergo a series of tapers and transitions to account for the different z-stratifications along the line. Finally, the feed line is connected to the double-slot antenna that radiates in the presence of the ADL. The antenna/ADL system is suspended by removing the silicon substrate, to avoid that the power is

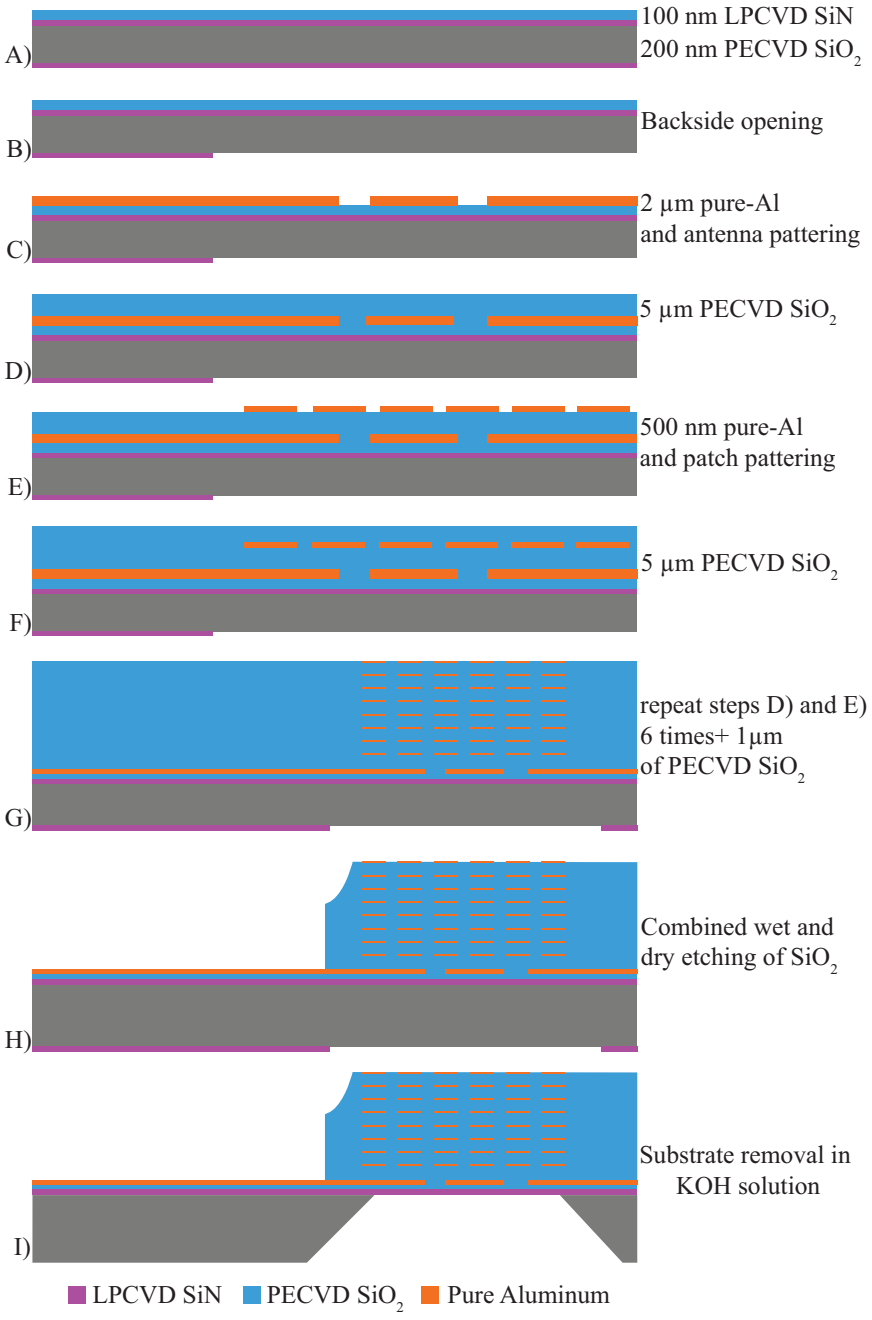

Figure 3.11: Main steps of the fabrication flow of Antenna/ADL device.

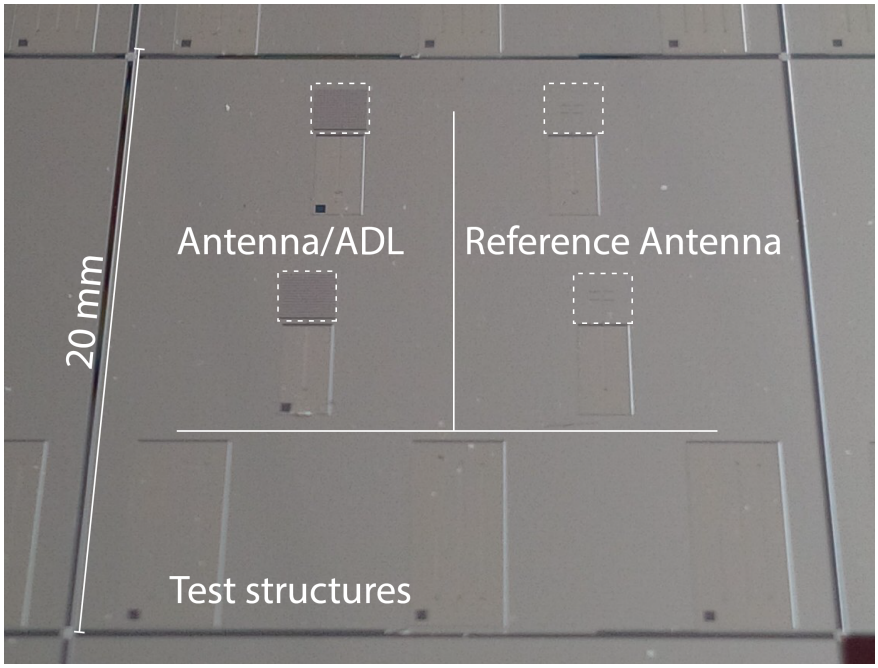

Figure 3.12: Top view of the die containing the antenna/ADL, the reference antenna and the calibration structures. The dashed area indicates where the silicon is removed from the back of the wafer.

radiated into silicon and then to enhance the effect of the dielectric contrast given by the ADL.

The fabrication processs starts with a thin (100 nm) low-pressure chemical vapor deposition (LPCVD) low-stress silicon nitride (SiN) layer on the silicon as hard mask for the back-side etching of the wafer, followed by 200 nm of plasma enhanced CVD (PECVD) silicon oxide to be used as electrical insulating layer and stopping layer for the further etching steps. The antenna layer was realized using a 2 μm thick pure aluminum layer deposited by radio-frequency (RF) sputtering, using an SPTS Sigma 204 DC magnetron system. The deposition temperature of the aluminum was 350°C, resulting in a layer conductivity of about $2.6 \cdot 10^7 \sigma$/m. The residual stress of this layer is 290 ± 23 MPa and has been measured using a TENCOR stress-meter.

The patterning of the metal layer is realized by first coating the wafer with a 2 μm layer of SPR 3017M positive photoresist and then using I-line

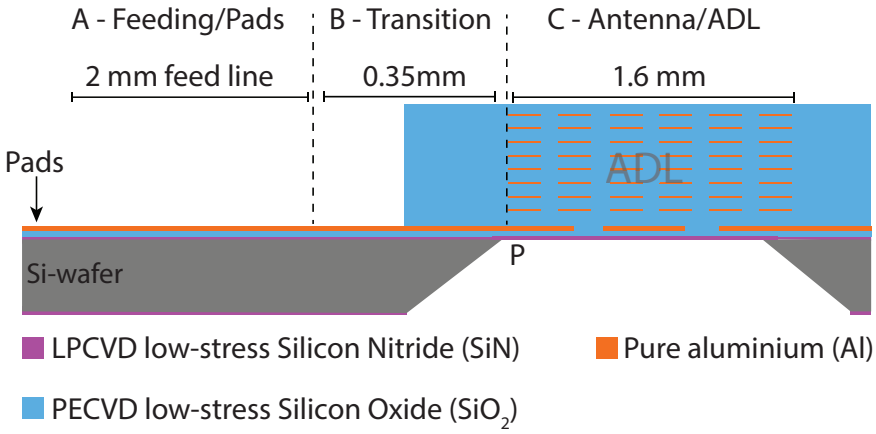

Figure 3.13: Schematic cross-section of the antenna/ADL structure. The device can be divided in three main parts: the feeding/pads area, the transition region and the antenna/ADL structure. The overall length of the structure is 4 mm, including the pads and the entire ADL length.

lithography (ASML PAS 5500/80 wafer-stepper) to define the features.

After the photoresist development, a dry etching process based on chlorine chemistry has been used to pattern the aluminum. The etching parameters, such as the gas ratio, etching time and depth uniformity, have been carefully optimized. This is because unwanted effects like over-etching or iso-etching could have resulted in larger features, compromising the impedance matching between the feed and the antenna. Moreover, any aluminum residuals in the thin slots could have shorted the antenna or the feeding lines in some points. For these reasons, accurate scanning electron microscope (SEM) inspections of the thin slots have been performed after the etching and the resist stripping (see Fig. 3.14 and 3.15). The PECVD silicon oxide deposited under the antenna layer prevents any damaging of the silicon nitride during the metal etching.

As explained in the previous sections, to ensure a correct matching between the slot antenna and the feeding lines, an accurate transition has been designed and the result is shown in Fig. 3.16. The structure in region B is designed to implement the transition between the large CPW lines (region A), with a inner conductor width of 22μm, and the CPW lines feeding the antenna slots (region C), with a inner conductor width of 11μm.

After the antenna fabrication, a separation layer of 5μm of silicon oxide is deposited in a PECVD Novellus Concept-One reactor. The ADL consists

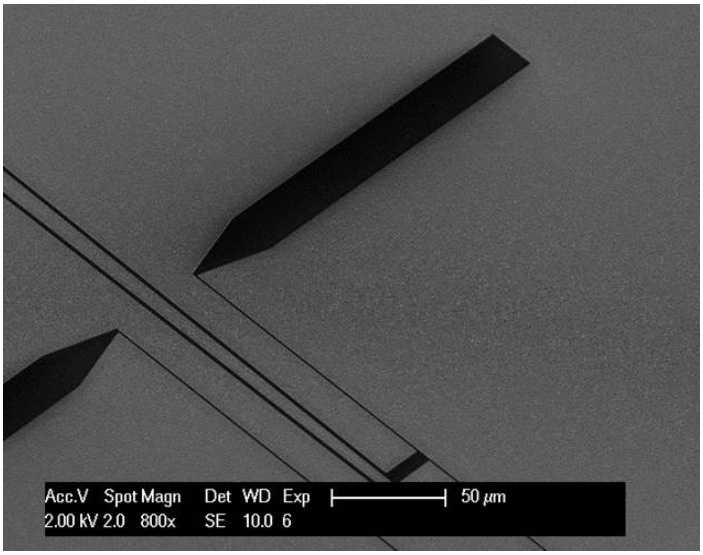

Figure 3.14: SEM picture showing the double slots antenna. The grey area is the pure aluminum layer while the dark area is the landing layer of PECVD silicon oxide.

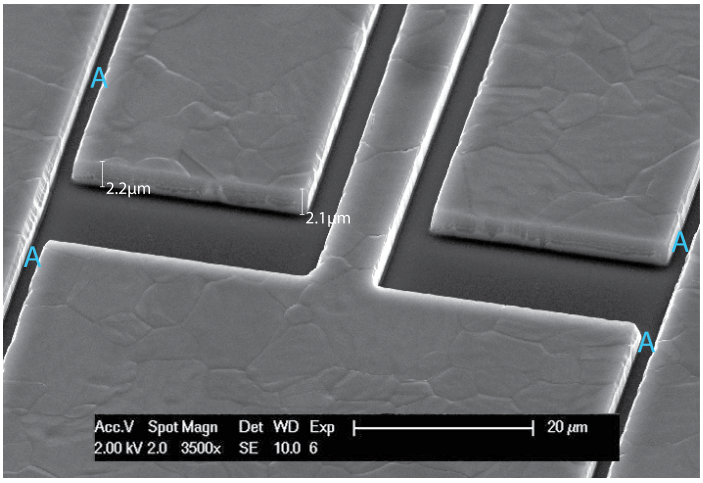

Figure 3.15: SEM picture showing a detail of the double slots antenna. The thick aluminum layer is clearly visible and the measurements confirm the thickness of 2μm. No visible aluminum residuals are present in the the structure. The thin opening marked by A are only 1μm wide.

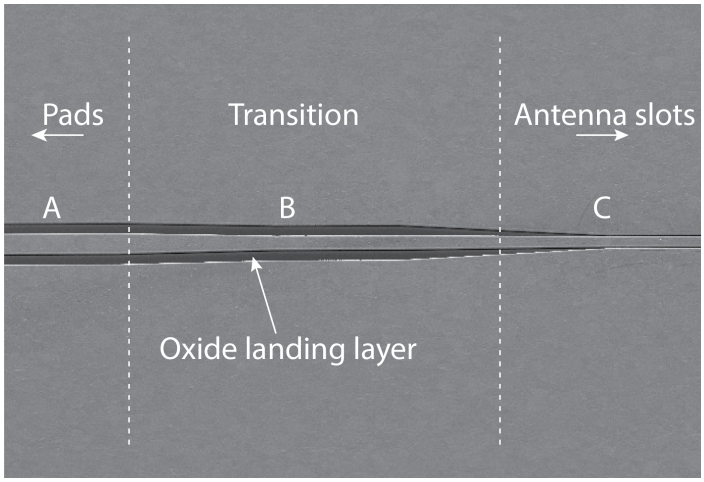

Figure 3.16: SEM picture of the transition region on the antenna feeding line.

of a stack of 7 metal layers embedded into a thick layer of PECVD silicon oxide. As first step, a pure aluminum layer (500 nm) is deposited using the same tool and deposition condition of the antenna layer. A layer of 2μm of SPR 3017M positive photoresist is used to define the ADL area. Each ADL layer consists of an array of 16×16 square patches that effectively cover the entire antenna radiation area. The patches are 85μm wide with a separation of 10μm in the xy plane. All the layers are patterned by means of I-line lithography and dry etching process. The details of the fabrication are shown in Fig. 3.17. After the patches definition, a layer of 5μm of low-stress (−30MPa) PECVD silicon oxide is deposited. Since the ratio between the height of the oxide layer and the metal patches is more than 10, step coverage is not an issue. After the oxide deposition, a new metal layer is deposited and etched. These process is repeated 7 times. A protective layer of 1μm of PECVD oxide is deposited to prevent possible damages of the ADL during the remaining process steps.

To achieve an effective enhancement of the dielectric constant, an accurate control of the oxide thickness and alignment of the metal patches is fundamental. By means of optical reflectometry (Leitz MPV-SP) measurements, the thickness of the layers was determined and carefully monitored during all process steps. The close-up of the ADL cross section (Fig. 3.18) clearly shows the metal patches embedded in the oxide layer. A maximum thickness deviation of about ∼80 nm on the entire wafer area is measured.

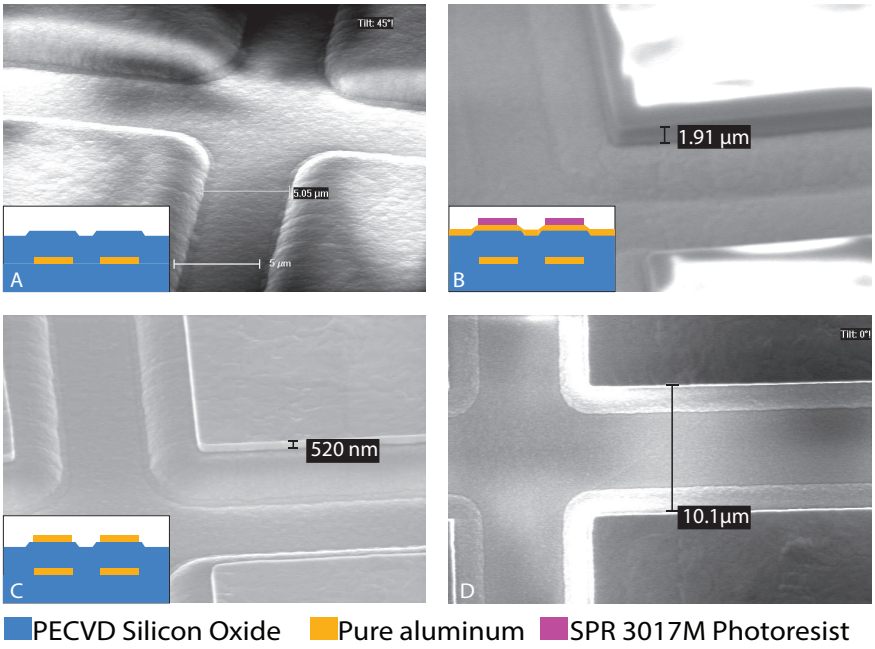

Figure 3.17: Series of SEM picture showing the ADL during the fabrication process. A) The 5μm silicon oxide layer is deposited on top of a metal patch layer (see in the inset the layer stack). The brighter area in the figure are given by electron charging phenomena in the SEM. After the silicon oxide coating, the aluminum layer is deposited and the patches defined by I-line lithography. In B) the photoresist layer is clearly visible and the measured thickness is $\approx 2\mu$m. Using a dry etching process, the patch layer is defined (C) and the relative distance between the patched measured (D).

Numerical simulations have confirmed that such variations have negligible effects on the ADL properties.

Using a similar process, a reference test-antenna has been realized on the same substrate, to allow a comparison between the antenna gain with and without the ADL. This structure is similar to the one presented in Fig. 3.13 and visible on the right side of Fig. 3.12. These antennas are covered only by the thick oxide layer used to realize the ADL, but no metal patches have been inserted in the fabrication flow.

After the ADL deposition, a final etching is required to remove the thick layer of silicon oxide that covers the antenna contact pads. Due to the large amount of oxide to etch, a single dry etch step would require a very thick

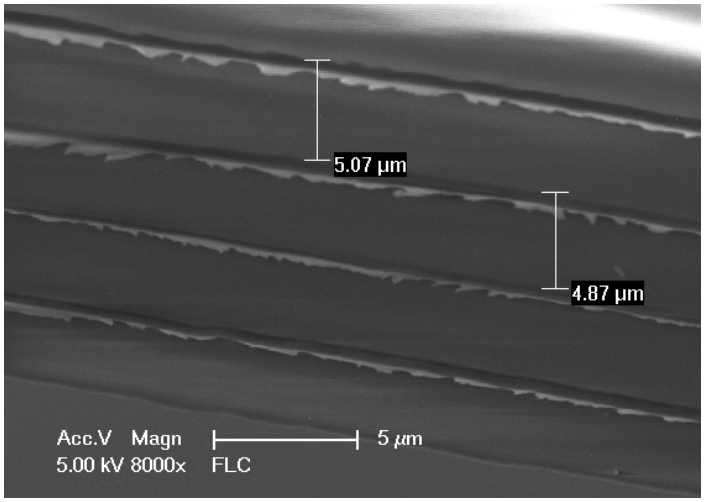

Figure 3.18: SEM cross-section showing a detail of the fabricated ADL stack. The overall ADL is $\approx 39\mu$m thick.

photoresist layer to protect the structures and a very long (more than 1 hour) plasma etching. Such long process could cause unwanted phenomena such as photoresist burning or large non-uniformity in the etched layer. For these reasons, a wet/dry combined etching has been performed. To protect the structures, a 12 μ m layer of SPR 3017M photoresist has been used. After the resist patterning, the oxide is etched in a buffered hydrofluoric acid (BHF) 1:7 solution (etch rate 290 nm/min), for 75 minutes. This step removes approximately 2/3 of the oxide layer, with a very high uniformity on the wafer area. A final dry etching step is then performed in a Drytek Triode 384T oxide dry etcher. SEM inspection has been performed on the wafer (see Fig. 3.19) and clearly show the thick oxide being etched and the aluminum layer exposed.

To release the antenna/ADL membrane and the test-antenna membrane, a silicon wet etching in a 33 wt % KOH at 85 °C has been performed on the wafer backside. The windows were previously patterned etching the LPCVD silicon nitride layer with a dry etching process. Then, using a special holder, the wafer front-side has been protected from the solution. After the etching (5 hours and 30 minutes), a final rinsing (HNO_3 and water) is performed to clean the wafer. The inspection of the etched cavity has shown that a small mismatch ($65 \pm 10\mu$m) in the KOH opening position (point P in Fig. 3.13) is present. This is probably due to a variation of the wafer

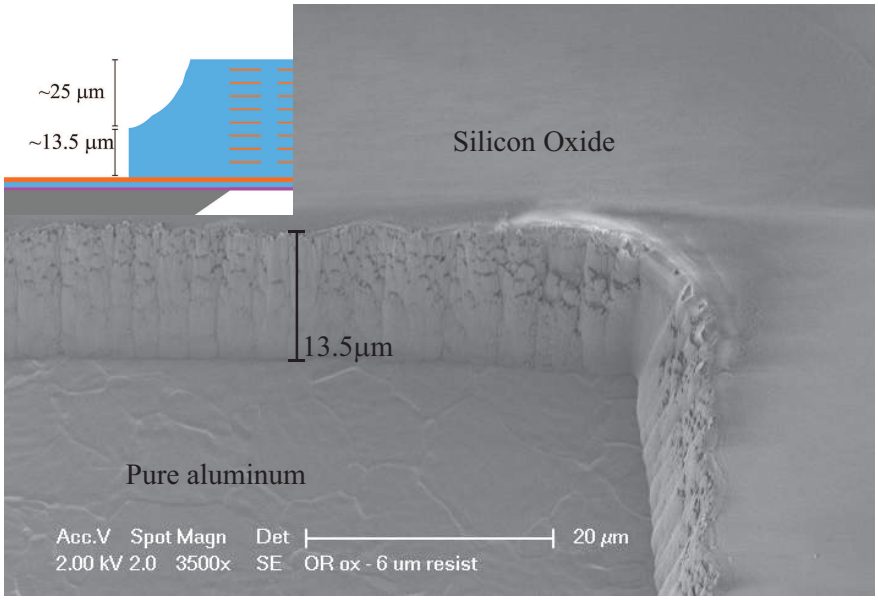

Figure 3.19: SEM cross-section showing a detail of the silicon oxide after the etching. The sample is here tilted 45ô to show the inner part of the cavity. The wet etching gives a round corner on the top of the silicon oxide layer (see the schematic in the inset). Approximately 25 μm of silicon oxide are removed with this process. The remaining 13.5μ m are removed by a final dry etching.

thickness and a front-to-back misalignment of the silicon nitride mask used to pattern the wafer backside.

3.4.1 Mechanical simulation

Due to the large dimension of the membranes, possible bucklings needs to be evaluated to ensure that only small deflections (if compared to the wavelength) are present. Unwanted deformation of the membrane could indeed induce lens-effect in the field propagation, causing a wrong estimation of the optical properties of the material. As the presented materials have a very high refractive index, even relatively thin dielectric slabs could induce a wave-front distortion. Some preliminary evaluations can be carried out by comparing the aspect ratio of the fabricated ADL membranes with earlier work on suspended structures. As shown by Ziebart et al. [80], high aspect ratio pre-stressed (−60.7 MPa) membranes of PECVD silicon nitride present a first order buckling mode when the a/t ratio is below 600. When

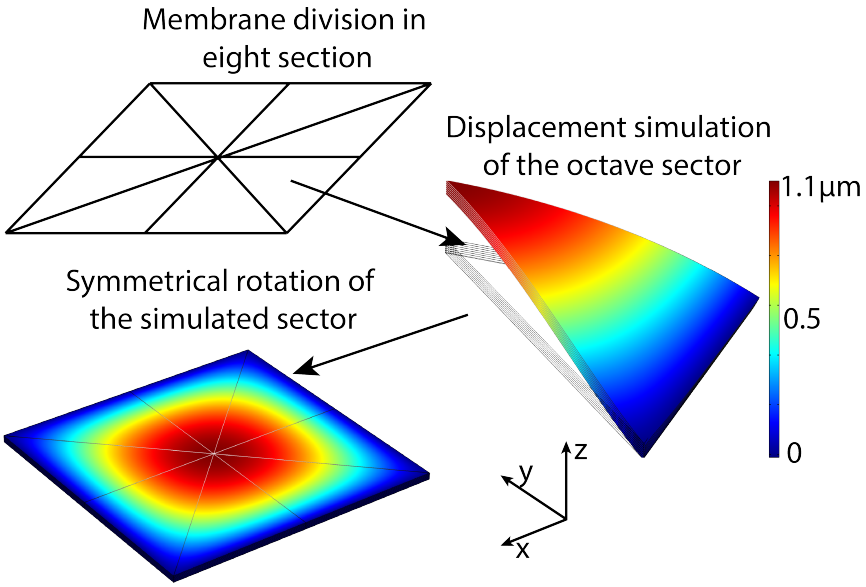

Figure 3.20: Mechanical simulation of one octave of the membrane. Symmetrical boundary conditions are applied on the side of the membrane portion.

the a/t ratio is larger than 800, higher buckling modes become relevant, breaking the geometrical symmetries of the membranes. It is important to remark that the membranes presented in this work are realized using different materials (silicon oxide and aluminum) and a layered structure. These design differences make a comparison with the structures presented by Ziebart not straightforward. However, the most relevant parameters, such as the residual stress, Young modulus and aspect ratio, are comparable with the values presented in the work of Ziebart. The ADL membranes here fabricated have an a/t ratio of ≈ 40.

These values are well below the limits set up by Ziebart, so only a first order buckling mode should occur. However, due to the different materials used and the layered structure of the ADL, an analysis is required to ensure the flatness or quasi-flatness of the membrane. For this reason, an accurate analysis of the membrane profiles has been carried out using a white light interferometer and the results compared to finite element module simulations

of the membrane deformation.

The mechanical properties of the ADL were simulated by using the Comsol Solid mechanics module, using linear elastic approximation. Due to the large dimensions, the geometrical symmetry of the membrane was used to reduce the number of elements to compute. As shown in Fig. 3.20, the ADL membrane was divided in 8 sections. Using symmetric boundary condition on the membrane section side and *rolling* condition on its vertex, it is possible to simulate a complete membrane by simulating only one octave of it.

Due to the large high aspect ratio of the membranes, a simulation of the entire membrane requires long time and a powerful calculator. Moreover, the thin multilayer structure of the ADL, that alternates metal patches (0.5 μm thick) with silicon oxide (5 μm thick), results in a complex mesh with a very large number of elements. To solve this problem, an effective interlayer that takes into account the mixed mechanical properties of the aluminium (patches) and the silicon oxide (the host matrix) has been here proposed. As shown in Fig. 3.21 a-b) the base element of the interlayer consists of a single metal patch surrounded by the host silicon oxide. The thickness of the interlayer is the same as the metal patch thickness. Using Comsol simulation tool, the mechanical properties such as residual stress, Young modulus and Poisson ratio of the single element have been evaluated. The properties of the interlayer are calculated by creating an array of the single patches and averaging over the volume the relevant mechanical parameters.

A large number of simulation (see Fig. 3.21(c)) have been performed, up to arrays of 100 single patch elements. The results show that the layer properties such as stress become almost constant already 25 elements. Small variations of the average stress are present in the range $25 - 100$ elements, giving an average residual layer stress of 288 MPa. These variations can be attributed to the relatively coarse mesh used. With the same process, the poisson ratio and the Young modulus of the layer have also been evaluated.

3.4.2 Deformation of the Antenna/ADL layer

To validate the presented method, the membrane deformation has been evaluated for the Antenna/ADL device and compared with profile measurements. In this case, the ADL is deposited directly on top of a 2 μm pure Aluminum, used to fabricate the antenna used to generate the 300 GHz e.m. field. This variation respect the original ADL design is taken into account by inserting this layer in the mechanical simulation performed in Comsol. However, the patterning of the metal layer is not considered in the simulations since involves only a very small percentage of the aluminium area ($\leq$ 2 %) and then any eventual change in the layer stress is considered negligi-

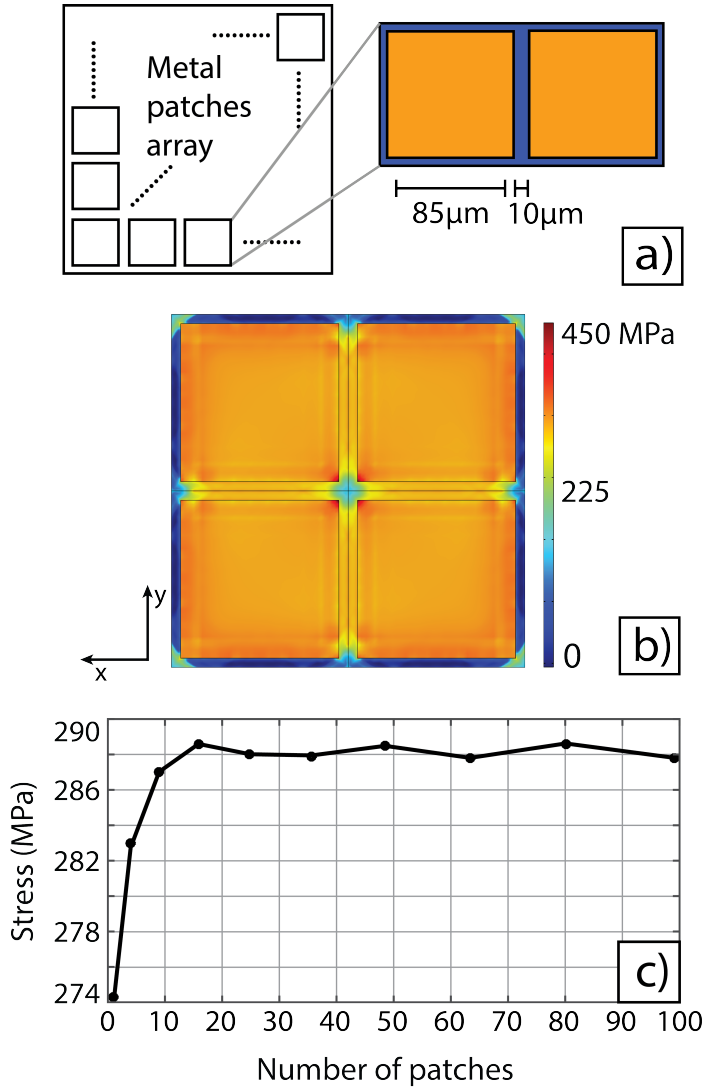

Figure 3.21: Mechanical simulation of the metal patch/oxide layer. The thickness of the structure is 0.5 μm. As expected the stress concentrates at the membrane corners, but do not overcome 450 MPa. In c) it is shown how the layer stress varies as a function of the patches. Saturation is reached already by inserting 25 metal patches. Minor changes are due to the relatively coarse mesh used.

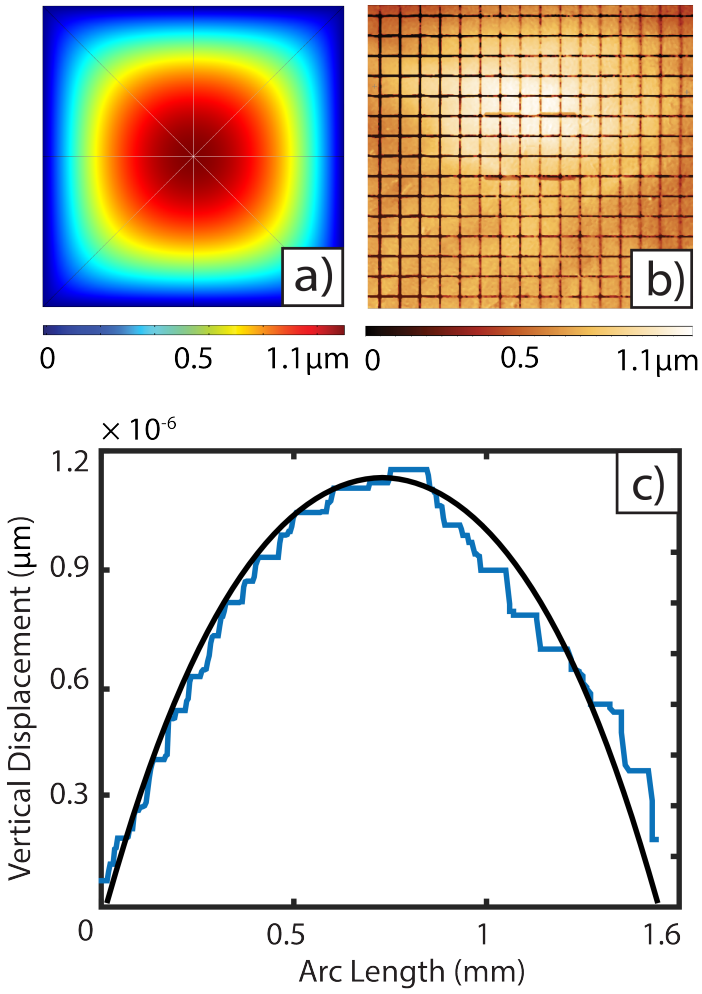

Figure 3.22: The deformation of the fabricated Antenna/ADL membrane under compressive stress. The simulated displacement (a) is compared to the measured 3D profile (b). The displacement along the z axis is plotted in correspondence of the membrane center (c), showing the very good agreement between the simulated and the measured results.

ble. To evaluate the membrane deformation after releasing, a profile of the membrane is carried out using a white light interferometer. By plotting the deformation of the layer along a line crossing the membrane in the center, it is possible to evaluate the vertical displacement of the structure. As shown in the Fig. 3.22, the maximum vertical displacement is approximately 1.1 μm and occurs in the center of the membrane, as expected.

The relative small aspect ratio of the membrane (1 : 40) results in a simple buckling of the membrane, without any high order deformation of the layer. These results indicate that after the releasing, the membrane presents a deformation in the order of $6 \cdot 10^{-3}$ λ_{eff} inside the metamaterial. No relevant deformation of the layer is then affecting the wave-front.

3.5 Conclusions

An innnovative antenna/ADL device is presented and the radiation efficiency of the system analyzed by means of numerical simulations. When placed on top of the radiating double-slot antenna, the front-to-back radiation ratio of the antenna/ADL shows a strong enhancement (higher than 10 dB over the matching bandwidth), while preserving a clean radiation pattern. Moreover, due to anisotropic permittivity of the ADL, no surface-waves are excited, thus further maintaining the radiation pattern purity and increasing the overall system efficiency.

An dedicated, low temperature ($\leq 400^o$C), CMOS compatible process is used to realize the proposed antenna/ADL design. By using low stress silicon oxide and aluminum layers, the ADL is fabricated on top of a double slot antenna, directly patterned on a thick aluminum layer. By removing the backside silicon with wet etching, a high aspect-ratio composite membrane is finally obtained. The deformations due to the residual stress are analyzed and compared to numerical simulations, showing that only minor deflections of the membrane are present, thus avoiding unwanted *lens* effects.

In the next chapter, the optical properties of the presented structure will be evaluated by using two different approaches and compared to the theoretically predicted ADL properties.

4

ADL characterization

The optical properties of the fabricated artificial dielectric layer are measured. Two different measurements methods are used, one that relies on the generation of the THz radiation with the integrated antenna and the second one that use an external source to probe the artificial dielectric membrane. Both measurements confirm the expected properties of the Artificial Dielectric Layer.

4.1 The antenna measurements

To evaluate the relevant parameters of the antenna in the presence of the ADL, a dedicated measurement setup has been used. This system allows the mapping of the antenna (near-field) radiative region, that is later converted in the (far-field) radiation pattern by Fourier transform. The radiation pattern and the gain of the antenna show a very good agreement with the theoretical predictions, thus confirming the overall efficiency enhancement given by the ADL.

4.1.1 The antenna measurement setup

The near-field measurement setup depicted in Fig. 4.1 [81]. It consists of an Agilent vector network analyzer (PNA-X N5242A) working from 10 MHz to 26.5 GHz. Frequency extension modules, to operate the VNA in the WR03 band (i.e. 220-325 GHz) from OML Inc. are used. The feeding to the antenna is realized by using GGB Cascade Infinity ground-signal-ground (GSG) waveguide probes with pitch equal to 100μm. The measured insertion loss of this probe (1 dB) was taken into account by a preliminary calibration step. To avoid the reflections from the metal chuck, commercial absorbers (ECCOSORB MMI-U) are placed below the antenna. A linearly polarized, WR-03 open ended waveguide (OEW) is used to sample the near field of the antenna under test (AUT) on a rectangular grid, while the AUT

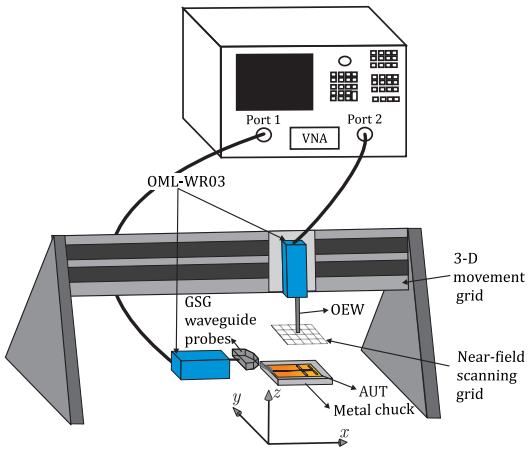

Figure 4.1: Schematics of the near-field measurement setup (not to the scale).

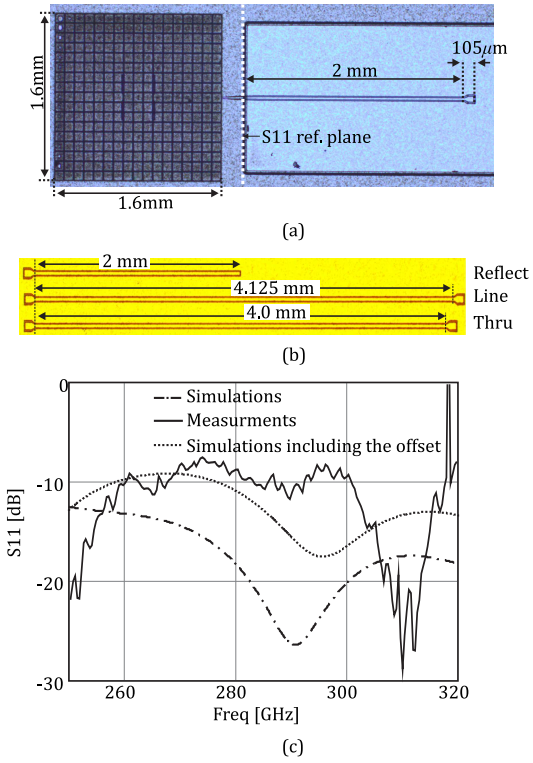

Figure 4.2: The fabricated (a) chip micrograph, (b) TRL structure, and (c) simulated and measured reflection coefficient.

is kept stationary. The distance between each spatial sample point was set to be $\lambda_0/8$ at 300 GHz, to obtain a high resolution data. The vertical distance (along the z-axis) of the OEW tip from the AUT is about 3.5 mm, i.e. radiative near-field region.

4.1.2 The measurement procedure

The fabricated chip (shown in Fig. 4.2(a)) was placed on a metal chuck. A 105μm long feeding pad to land coaxial probes and a feeding line was added on the back of the antenna, as labeled in the chip micrograph in Fig. 4.2(a). The length of this line was selected to be 2 mm, to trade off loss levels with scan area: on one hand, a too short line would cause the bulky wafer probe to be too close to the antenna, limiting the near-field scanning

area needed for the radiation pattern measurements; on the other hand a line that is too long would introduce too high losses reducing the accuracy of the measurement.

4.1.3 Results and discussion

The long line (i.e., 2mm) is de-embedded from the measured data employing a thru-reflect-line (TRL) technique [82]. Figure 4.2(b), shows on-chip test structure that are fabricated on the same die as that of the antenna (see Fig. 3.12) and are measured to apply TRL procedure. The measured de-embedded one port reflection coefficient is presented in Fig. 4.2(c), compared with the simulation results. There is a frequency shift of 6% between the measured and the simulated values. As pointed out earlier in section 3.4, a mismatch during the KOH etching process has resulted in an offset of point P (see Figure 3.13) by a distance of $65 \pm 10\mu$m. The S11, recomputed after including the above-mentioned mismatch in the simulation, is shown in Fig. 4.2(c). The error difference between simulation and measurement is now reduced to 3%. Also, the measured and simulated reflection coefficients starts to show a similar trend at the low end of the frequency band (250-280 GHz).

The measured normalized amplitude and phase of the electric field radiated by the AUT in the presence of probe is shown in Fig.4.3 (a) and (b), respectively. Since the AUT and OEW are linearly polarized, only the x-component of the near field was measured. The scan area is rectangular and the maximum of the electric field is around $x = 0$ and $y = 0$, which denotes the center of the AUT. The acquisition of near field data along the $-x$-direction is limited by the presence of the GSG waveguide probe, which is an usual limitation in these type of measurements [63, 83, 84].

The effect of the OEW is de-embedded from the far-field pattern of the AUT by using a standard probe correction technique [85]. The far-field radiation patterns in the upper hemisphere, obtained by Fourier transform of the near-field data, are shown in Fig. 4.4, in the frequency range from 300-315 GHz. The patterns in the H-plane show an excellent agreement with the simulations. The E-plane patterns are asymmetric and oscillatory. The reason is the scattering from the probe, which interferes with the antenna. Also, the patterns are shown till $\pm 45°$, because the near-field scan area is restricted to ± 1.5 mm (see Fig. 4.3) by the presence of the wafer probe. Since the near-field area is limited along the x-direction the accuracy of the radiation pattern measurements decreases for angles greater than $\pm 23°$.

The relative difference between the broadside gain of the two antennas (with and without ADL) is presented in Fig. 4.5. Both simulations and measurements show an improvement of about 2 dB for the ADL loaded an-

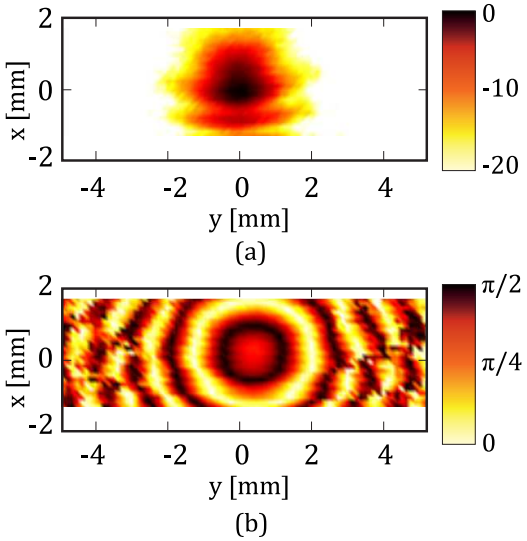

Figure 4.3: The measured near field at 300 GHz a). Normalized amplitude in dB b). Phase in radians.

tenna with respect to the reference one. The measured results are presented in a frequency range of 20 GHz centered at 300 GHz, where the simulated reflection coefficient is well matched for both antennas (see Figure 3.6).

At a later moment, a scan over a bigger aperture in the direction where there is no feed probe was carried out. The measured near field data is shown in Fig. 4.6(a) at 300 GHz. A symmetric near field data is obtained artificially by mirroring the near field data (see Fig. 4.6(b)) with respect to the x-axis ($x = 0$). Exact symmetry conditions are also imposed on the simulated near field data from CST. The far field patterns after post-processing are shown in Fig.4.6(c) for both the cases. A better agreement can now be observed between the simulations and the measurements. This approach for artificially symmetrizing the pattern gives an indication of how the antenna would operate in a realistic application scenario, in which there would be no feeding probe.

Also the reference antenna without the ADL was measured. A comparison between the simulated and the measured far field radiation patterns is shown in Fig. 4.7, at 300 GHz. Although not shown for the sake of brevity, the radiation patterns at other frequencies show a similar agreement.

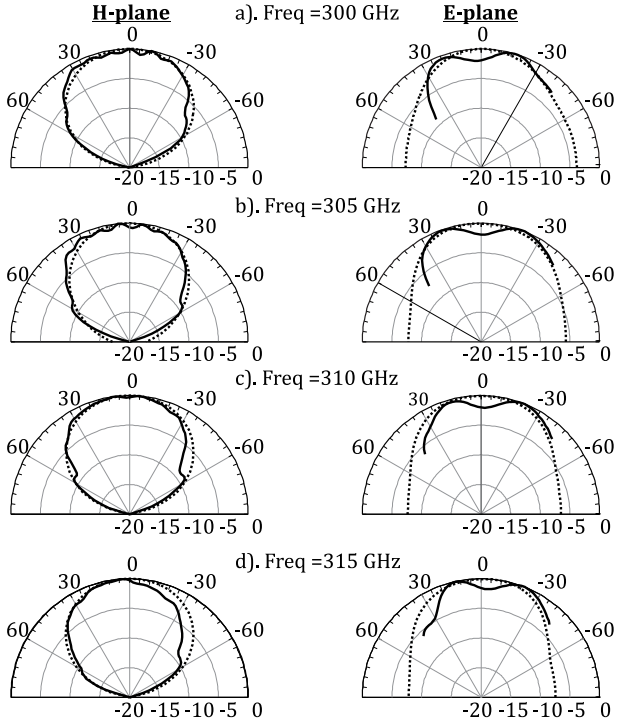

Figure 4.4: Measured(-) and the simulated (- -) radiation pattern (dB) with ADL.

4.2 Time domain spectroscopy measurements

To further confirm the optical properties of the ADL, the optical properties of the material have also been measured using a Time Domain Spectroscopy (TDS) measurement setup. For these measurements, a new set of devices has been prepared. Although the multilayer structure remains the same, the ADL membrane is much wider. In fact, as the THz beam spot measures few squared millimeter, the area available using the Antenna/ADL design would have not been large enough to guarantee a uniform illumination. Part of the THz beam could have indeed hit the wall of the silicon KOH cavity, resulting in unwanted reflections. For this reason, 5 × 5 mm square membranes have been fabricated.

The process used is similar to the one presented in the previous sections, with the obvious absence of the antenna layer. As the membrane are much

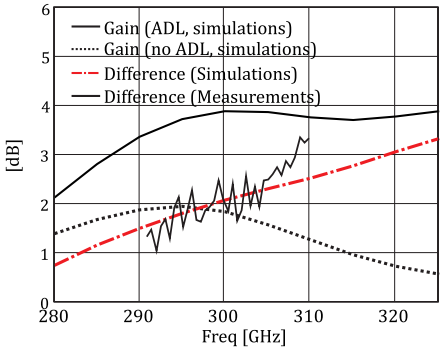

Figure 4.5: Simulated gain of the two antennas, with and without the ADL loading; the relative gain difference is also reported and compared with the measured one.

larger, new mechanical simulations have been performed, to ensure that no major deformation are present. As in the case of the Antenna/ADL layer, a white light interferometer has been used to map z displacement of the membrane.

As shown in Fig. 4.8, the membrane presents only a first order buckling, resulting in a very small deformation in the center (less than 5.5 μm). This result confirms that such membranes can be indeed realized on a larger scale and that the resulting deformation are in the order of 10^{-3} times the side dimensions.

4.2.1 The Time Domain Spectroscopy system

Fig. 4.9 shows the system used to perform measurements on the ADL layers. A femtosecond laser (center wavelength 775 nm) that generates 450 mW of average power, and produces 15 fs pulses with a 72 MHz repetition rate hits the surface of a SI-GaAs crystal. On the surface of the semiconductor, two silverpaint electrodes are painted with a separation of 0.4 mm. The sample is glued, using silverpaint, on two 2 mm thick and 1 cm wide copper strips, separated by 2 mm. Each copper strip forms a contact to one silverpaint electrode only. The copper strips have two functions: they serve as electrical contacts to the voltage source and they provide a good sink for any heat generated in the GaAs crystal. Indeed, when the GaAs is illuminated, an average electrical power of about 5 W is dissipated in the crystal.

A 50 kHz, 400 V square wave ac bias voltage is applied to the emitter. As reported in [86], by changing the voltages from 400 to -400 V the THz

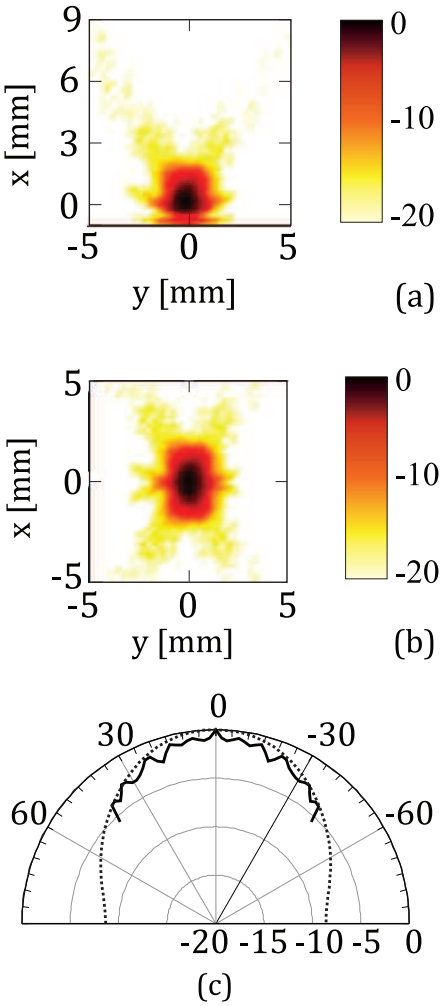

Figure 4.6: The near-field expressed in dB (a) measured, and (b) obtained after applying symmetry to the measured data. (c) Measured (-) and the simulated (- -) far-field radiation pattern (dB) in *E*-plane. The process of symmetry has also been applied for simulated antenna.

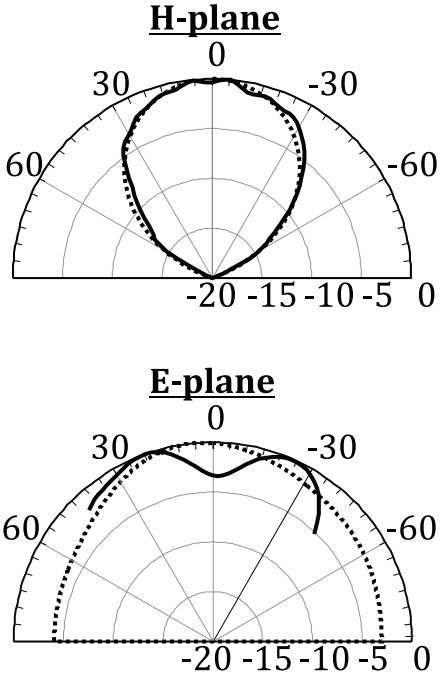

Figure 4.7: Measured (-) and the simulated (- -) radiation pattern of the antenna without ADL loading at 300 GHz.

signal changes sign as well, resulting in a signal detected by the lock-in amplifier that is twice the signal one would get when the applied voltage switches between 0 and 400 V only.

A silicon hyperhemispherical lens is glued on the back of the crystal to focus the emitted radiation in a more forward direction. The material to test is inserted in the optical path of the THz beam. By comparing the shape of the original subpicosecond THz pulse with the one transmitted inside the material, it is possible to calculate the frequency dependent refractive index.

A slightly different version of the final stage of the setup (green ellipse in Fig. 4.10) was used. After passing through the desired optical path (i.e. through the ADL membranes in this specific case), the THz beam passes through a 2-mm-thick piece of polystyrene foam. The polystyrene foam has a refractive index of 1.017 with a very low absorption coefficient (less than 1 cm^{-1}), that blocks any small infrared signal around the emitter.

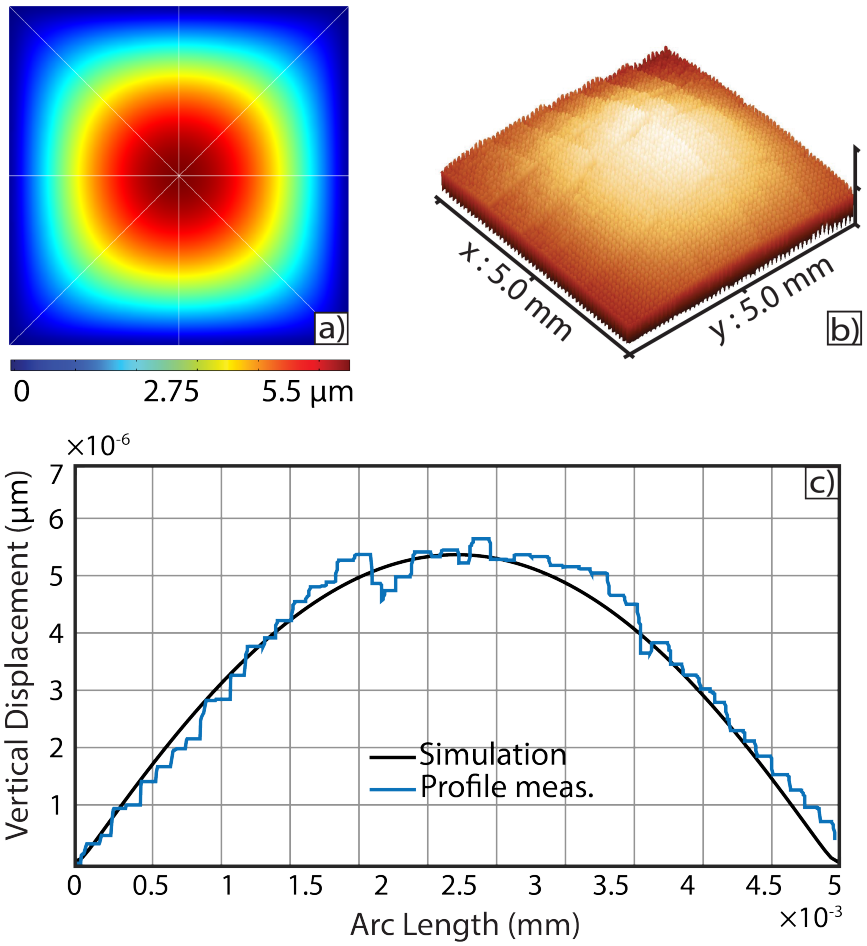

Figure 4.8: The deformation of the fabricated 5 mm ADL membrane under compressive stress. The simulated displacement (a) is compared to the measured 3D profile (b). The displacement along the z axis is plotted in correspondence of the membrane center (c), showing the very good agreement between the simulated and measured values.

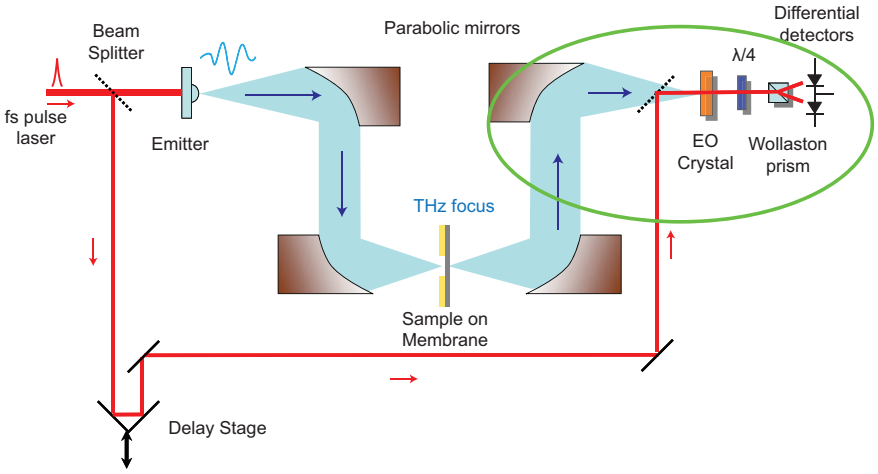

Figure 4.9: Terahertz time domain spectroscopy setup. The green ellipse indicates the final stage of the setup and is described in Fig. 4.10.

A small prism is glued onto the foam. The prism is used to combine the THz pulse with a synchronized, time-delayed, horizontally polarized probe pulse. Both the THz beam and the probe beam are focused onto the detection crystal. The probe beam then passes through a quarter-wave plate and a Wollaston prism that separates the two orthogonal polarization components of the beam. These components are finally focused into a differential detector that measure the electric field of the THz pulse.

4.2.2 Results and discussion

In Fig. 4.11 the pulse shape of the TDS setup with (dashed blue line) and without (solid black line) the ADL membrane is plotted. It is clear that the presence of the device cause a delay of the THz beam. From this values it has been possible to extract the refractive index of the ADL, as shown in Fig. 4.12.

Two different measurements are reported (dashed lines). A comparison between the plots indicated that the measurements do not precisely match the predicted refractive index value. However, by averaging the two curves, a fair comparison with the theoretical prediction is obtained. The mismatch between the simulations and measurements can be possibly caused by the following effects.

- Finiteness effect of the ADL thickness :

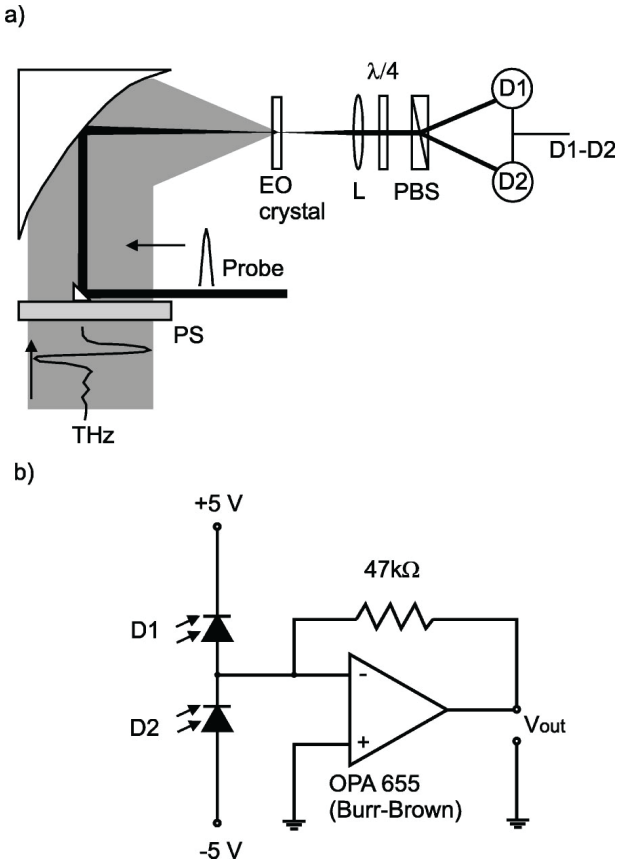

Figure 4.10: a) The THz detection setup, with PS a 2-mm-thick polystyrene foam sheet, L a lens, PBS a polarizing beamsplitter, and $\lambda/4$, a quarter waveplate. The small triangle on the polystyrene plate is the gold coated prism. b) The differential detector. D1 and D2 are photodiodes of type $BPW34$ from Siemens.

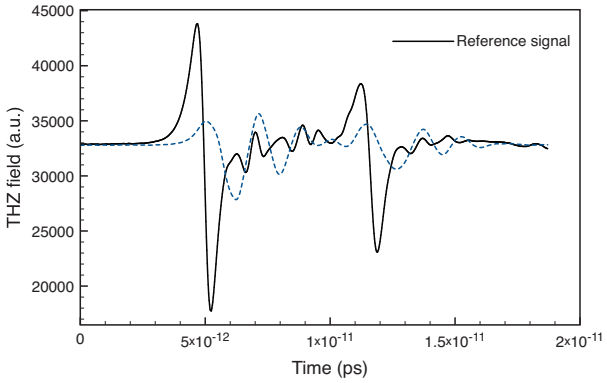

Figure 4.11: The THz field in the time domain. The reference pulse (no sample) is reported in black. The pulse shape with the sample inserted in the optical path is reported in blue.

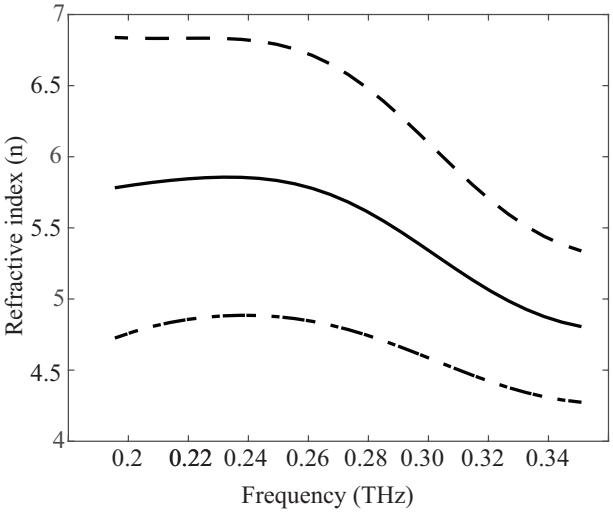

Figure 4.12: Refractive index (real part) of the ADL membrane. The dashed lines represents two different measurements. The solid line is obtained by averaging these data. The averaged value is ≈ 5.7 around 300 GHz, as predicted by the simulations.

This effect usually arises when a *finite* thickness ADL slab is used instead of an *infinite* ADL slab to obtain the constitutive parameter of the effective homogeneous medium [77].

- The tilting of the sample with respect to the polarization of the incident beam :
  The positioning system in our measurement setup allowed to orientate the membrane with respect to the incident beam with a relative uncertainty of $\approx 5^\circ - 10^\circ$.

4.3 Conclusions

On-chip integrated antennas typically radiate in the presence of either a lossy silicon substrate or an electrically thin grounded slab. This leads to either high dielectric losses or very narrow bandwidths of operation. We demonstrate that artificial dielectric superstrates previously proposed at lower frequencies and using printed circuit board technology, increase the radiation efficiency of such antennas at 300GHz. A conventional double slot antenna is loaded by an ADL superstrate that substantially increases the front-to-back ratio.

For the fabrication of the antenna and the ADL superstrate, we developed a low-temperature CMOS back-end compatible process. By using pure aluminum as metal and silicon oxide as dielectric host matrix, the ADL was deposited directly on top of the antenna structure.

The anisotropic properties of the proposed artificial slab allows to achieve high surface-wave efficiency. This is because the ADL is dense and electrically thick for waves radiated by the slot in directions close to the normal, whereas it has lower permittivity and is electrically thin for the waves radiated in directions almost parallel to the slab.

The antenna has a front to back ratio larger than 10 dB, with essentially no power launched into surface waves. Also an antenna without ADL loading has been fabricated and used as a reference solution to quantify the enhancement due to the ADL. The simulated results indicate an improvement of about 2 dB, confirmed by the measurements.

The key feature of the proposed ADL superstrate solution is that they can be designed and manufactured independently from the antenna and the ICs. They can be used as add-on components since no alignment is required between the antenna and the superstrate layers. Also, ADL are broadband because of their non-resonant periodic nature. This concept can be beneficial for any on-chip radiating structure, including antenna arrays.

Although the oxide/aluminum base ADL represents a reliable choice to increase the efficiency of planar antennas, the deposition of the thick (5 μm

) oxide inter-layers requires a relatively long deposition and a long etching process to remove it from the measurement pads.

In the next chapter PECVD Silicon Carbide, is proposed as possible alternative host medium to the silicon oxide. This material with a larger refractive index, can allow the deposition of thinner separation layers, thus reducing processing time and complexity.

5

Silicon Carbide based ADL for higher frequencies

In this chapter the use of PECVD Silicon Carbide as possible alternative to silicon oxide layer in ADL fabrication process is discussed. The surface and mechanical properties of the layer are presented. The optical properties in the THz are measured, showing a very high refractive index in a large bandwidth. The design of a SiC-based ADL is then presented, indicating that a substantial decrease in the ADL thickness can be achieved.

5.1 PECVD Silicon Carbide as structural material for ADL fabrication

During the last decades, silicon carbide (SiC) layers have been used in the fabrication of many microsystems such as waveguides [87,88], hotplates [89] and MEMS [90, 91]. Due to the high mechanical strength, good thermal conductivity and remarkable chemical inertness, SiC layers are also suitable as structural material and protective coating for MEMS working in harsh environments [89,92,93]. When exposed to very high temperatures ($1050 - 1200\ ^oC$), this material naturally forms a silicon oxide layer [94, 95], thus making it also suitable for the fabrication of Metal-Oxide-Semiconductor (MOS) devices.

To the author knowledge, very limited literature exists on the use of SiC for THz applications. Due to the the intrinsic wide-bandgap, SiC has been used in the fabrication of impact avalanche transit time (IMPATT) diodes [96]. In fact, if compared to traditional Si and GaAs based devices, SiC based diodes can operate with higher output power levels and higher breakdown voltages .

As demonstrated in the previous sections, ADLs can be effectively used to enhances the properties of THz planar antennas. However, if low refractive index materials, i.e. silicon oxide, are used in the ADL fabrication, the resulting device is quite thick ($\approx 40\mu$m). To effectively reduce the thickness of the ADL, high refractive index dielectric materials are then required [66].

Here we present amorphous PECVD SiC layers as alternative dielectric layer in ADLs fabrication. The mechanical, optical and morphological properties are discussed, to evaluate the suitability and compatibility of this material with the fabrication of large ADL membranes. By using a TDS spectroscopy setup, the refractive index of this material is measured, showing very high values in the $0.2 - 2$ THz range. Finally the design of a SiC-based ADL is presented, resulting in a thickness reduction of a factor 2.44 with respect a similar silicon oxide based device.

5.2 Deposition and structural properties of SiC layers

Silicon carbide layers were deposited in a Novellus-Concept PECVD reactor, using SiH_4 and CH_4 as precursors. Measurements of the residual thermal stress have been performed using a TENCOR-Flexus stress meter. By tuning the precursors ratio, the stress of the layer was reduced up to 25 MPa (tensile). In Table 5.1 and 5.2 the deposition parameters and the main layer properties are reported. The thickness and the optical properties of

the layer are determined by spectroscopic ellipsometry, using a Tauc-Lorentz dispersion relation (see Fig. 5.1).

A complete surface characterization has been performed with AFM technique to ensure that only small grains are present, as shown in Fig.5.2 and 5.3(a-b). The average grain size on the surface is $\approx$ 17 nm, with an estimated roughness of 0.1 nm.

5.3 SiC refractive index in THz frequency

The THz refractive index of SiC has been investigated by using the Time Domain Spectroscopy (TDS) setup presented in described in section 4.2. With this system, the real part of the refractive index has been evaluated over a large bandwidth (0.2 - 2 THz). As in the case of the silicon oxide-based ADL, large and undeformed membranes have been fabricated to effectively measure the layer properties.

The membranes were realized starting from p-type $< 100 >$, 100 mm, silicon wafers. A thin (100 nm) layer of low stress LPCVD SiN is first deposited as hard mask for the back-side etching of the wafer. The SiC layer ($\approx$ 20 μm) is then deposited, using the abovementioned low stress recipe (see Table 5.1 and Table 5.2). To release the membrane, the backside SiN is first patterned and the silicon removed by wet etching in a 33 wt % KOH at 85^o.

The result of this process are large (5 mm $\times$ 5 mm) and flat membranes (See Fig. 5.4). No buckling of the membrane is observed, due to the low residual tensile stress.

Temp.	SiH_4	CH_4	$RFpower$
$^\circ C$	(sccm)	(sccm)	(W)
400	250	3000	750

Table 5.1: Deposition conditions of the PECVD a-SiC layer.

Dep. rate	Stress	Refr. index (n)	Refr. index (k)
$^{nm}/_{min}$	(MPa)	at 633 nm	at 633 nm
60	25	2.69	0.05

Table 5.2: Main properties of the PECVD a-SiC layer.

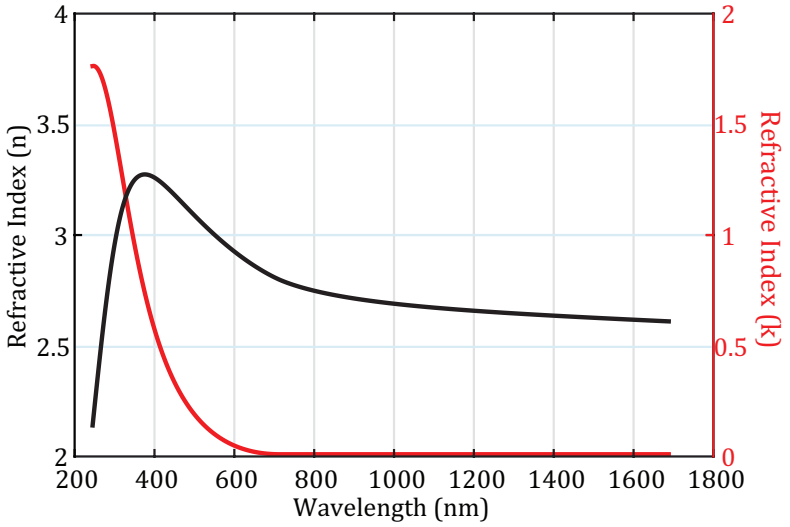

Figure 5.1: Refractive index of the PECVD a-SiC in the $250 - 1600$ nm frequency range extracted from ellipsometric analysis. A marked absorption in the ultraviolet part of the spectrum is present, while at lower energy (near-infrared) the k goes rapidly to zero.

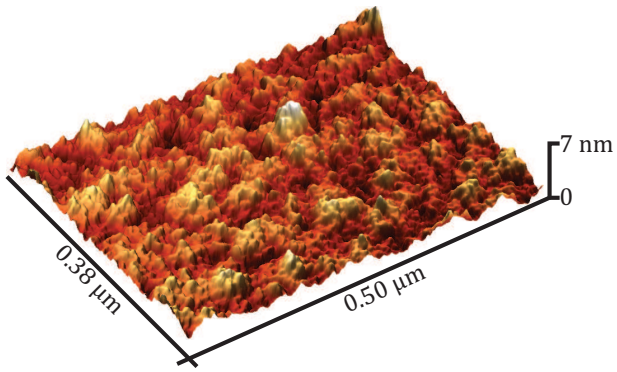

Figure 5.2: SiC surface as obtained by AFM analysis.

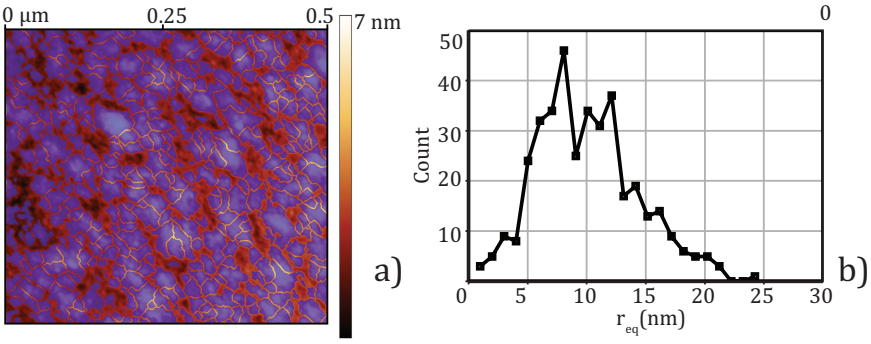

Figure 5.3: Grain analysis of the SiC surface on a 0.25 μm^2 area. The average grain dimension is roughly 7 nm.

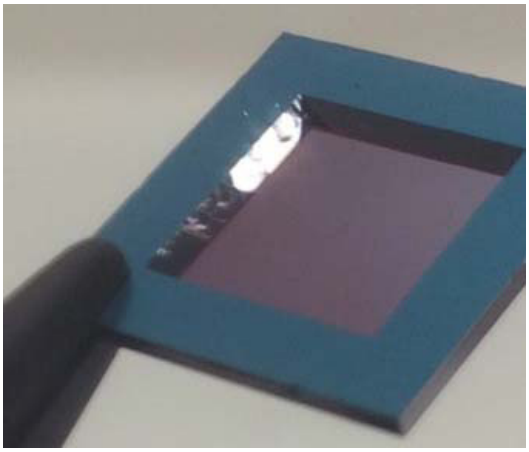

Figure 5.4: Microphotograph of the PECVD-SiC membrane (view from the backside).

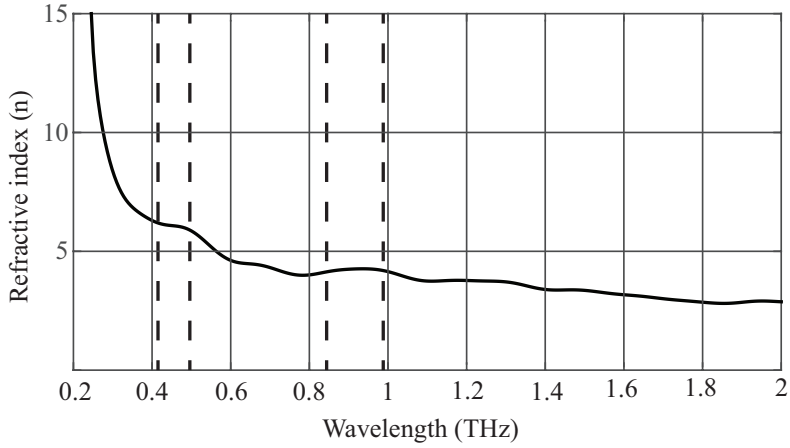

Figure 5.5: Silicon carbide refractive index between 0.2 and 2 THz. The curve shows a parabolic behaviour, presenting at least two different band ($0.42 - 0.5$ THz and $0.85 - 0.97$ THz) where the n value shows only small variations.

In Fig. 5.5 the refractive index between 0.2 and 2 THz is presented. The observed trend follows a Cauchy dispersion relation. It is possible to observe that there are at least two different bands where the refractive index is practically constant (see dashed lines). The first one ($n = 6$) is centered around 450 GHz and spans almost 100 GHz, while the second one ($n = 4$) is centered around 900 GHz and covers a larger bandwidth ($850 - 970$ GHz).

5.4 Silicon carbide based ADL

By using the design rules presented in the previous chapter, it is possible to realize ADLs working in these frequency range. Due to the SiC properties, the final thickness of these ADLs will be consistently reduced if compared to silicon oxide based devices. In Table 5.3, the relevant design parameters for an ADL working around 450 GHz are reported. The resultant thickness (t_{ADL}) for a SiC based ADL is ≈ 9 μm. If realized by using silicon oxide, the same ADL would have been 22 μm thick.

The calculation of these parameters has been carried out by using the same criteria reported in [66] and applied in the fabrication of the antenna/ADL device presented in the previous section.

Table 5.3: Physical Dimensions of SiC-based ADL. The data are calculated by choosing a central frequency of 450 GHz.

d_{adl}	d_z	w_{adl}	n_{layers}	t_{ADL} (μm)
19	1.2	2	7	9

5.5 Conclusions

The use of silicon carbide as alternative material in ADLs fabrication is discussed. The material shows almost zero residual stress and an extremely low surface roughness. By using the same fabrication process presented in the previous chapter, large SiC membranes are fabricated and the refractive index measured by using a TDS setup. The results indicate that SiC has a very high refractive index in the $0.2 - 2$ THz range. In two different bands (each of them 0.1 THz wide), the SiC refractive index presents a constant values (6 and 4, respectively) and, consequently, can be used in the fabrication of ADL devices. By using the same design criteria presented in the previous chapters, the relevant parameters for a SiC-based ADL are then established. The results show that the final thickness of SiC-ADL membranes can be reduced by a factor 2.44 compared to similar silicon oxide-based devices.

6

MHz passive components : Supercapacitors

In this chapter existing supercapacitors technologies are introduced. Conventional supercapacitors architectures are reported and their performance discussed in detail. To overcome their limitations, an innovative solid state supercapacitor is presented. This device is based on the use of metallic carbon nanotubes (CNTs) as electrodes. By using Atomic Layer Deposition (ALD), the large surface area of the CNTs is exploited by conformal dielectric and conductive layers, resulting in a high specific capacitance and a large operating frequency range.

6.1 Introduction

There is a great demand for the manufacturing of high performance, light and small size electronic devices, such as mobile phones and wireless sensor networks. Their ability to perform a large variety of operations is intrinsically coupled with energy requirements, driving the necessity of a new generation of compact and efficient energy storage devices. In this regard, there is a great interest in high performance supercapacitors. These devices represents a reliable choice to store energy, ensuring high power density and high specific capacitance. The extremely fast discharge rate, typical of such devices, make them suitable for applications where temporary energy storage is requested, such as regenerative car breaking. Using a supercapacitor, the energy dispersed by the vehicle during the braking can be stored and then used when large power boosts are needed.

However, supercapacitors are also attractive as *on-chip* components (see Fig. 6.1). In fact, the ability to fabricate large capacitance devices is a key step in modern heterogeneous integration (i.e. System in Package technologies) [97, 98], where large decoupling/filters supercapacitors are often necessary. Usually these devices are realized by deep trenches in silicon that are subsequently coated by a conformal dielectric layer. Highly doped polysilicon is then used as capacitive counter-electrode.

In this chapter a fully solid state supercapacitor is presented as possible alternative to such class of devices. The supercapacitor is based on dense CNTs bundles coated with aluminum oxide and titanium nitride deposited by Atomic Layer Deposition and results in a capacitance density of

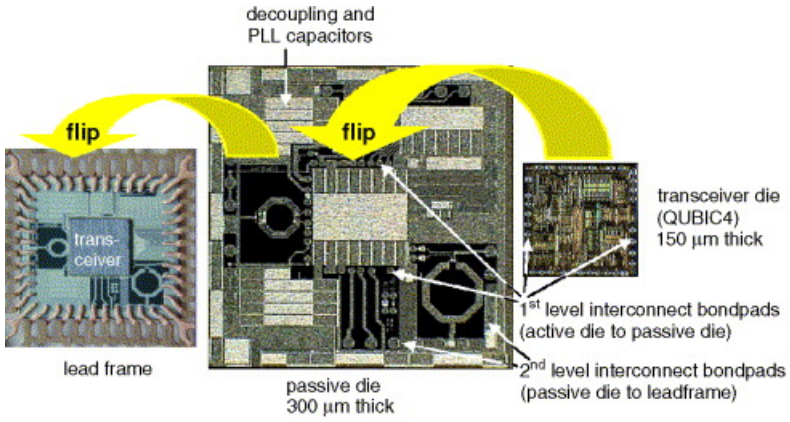

Figure 6.1: Passive die in a Bluetooth radio module [97].

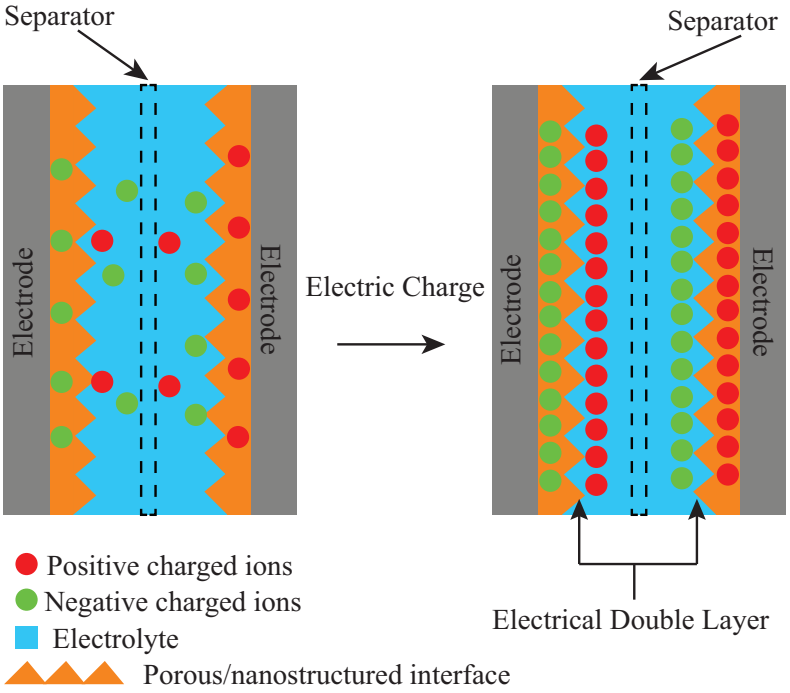

Figure 6.2: The typical architecture of a double layer capacitor (EDLC). The charge is stored electrostatically in the Helmholtz double layer that generates at the interface electrode/electrolyte. By realizing porous or/and nanostructured electrodes, the surface area increases, thus increasing the accumulated charge.

25 nF/mm^2 and operates up to a frequency of 1 MHz.

6.2 Supercapacitors

With the term *supercapacitors* we usually refer to high capacitance devices that store from 10 to 100 times more energy per unit volume (or mass) than conventional capacitors. Supercapacitors can be divided into two main categories, electrochemical supercapacitors (EDLCs) and dielectric solid state supercapacitors, according to the different mechanism that allows the charge storage.

6.2.1 Electrochemical supercapacitors

The term electrochemical supercapacitors usually refers to devices that store electrical charges using liquid or solid electrolytes. These devices can be devided in Electric Double Layer Capacitors (EDLCs) and pseudocapacitors.

The EDLCs store the electrical charge at the electrode-electrolyte interface (see Fig. 6.2), providing high power density with excellent charge-discharge cycling stability [99–101].

Conversely, in pseudocapacitors, the storing mechanism is based on the charge transfer between the electrode and the electrolyte (faradaic mechanism). These devices present a higher specific capacitance with respect to classical EDLC devices [102]. The electrolytes that allow the charge transfer/storage used in these two types of devices are mainly liquid ones, but solid-state electrolytes have also been reported [7, 8, 10–13].

The performance of electrochemical supercapacitors can greatly benefit from the use of nanostructured electrodes, such as carbon nanotubes, graphene or nanotemplates [7–13, 103]. In 2011 Shen et al. [104] have shown that by using electrochemical capacitors with composite nanostructured carbon as electrodes, it is possible to achieve a very high capacitance density (up to 90 mF/cm^2 in the 0.1-25 Hz frequency range).

Despite the relevant high capacitance values, the use of electrochemical supercapacitors in the IC industry still represents a challenge. In fact, the use of a liquid electrolyte, often highly toxic and corrosive, in proximity of electrical circuits, requires a solid encapsulation of the electrolyte to avoid any possible leakage. The packaging problems associated with this, makes the integration in a conventional IC process quite complex. Furthermore, the use of electrolyte capacitors is still problematic in particular applications, such as space and automotive, as the different environmental conditions (e.g. high temperature, pressure) in which the capacitors are subjected to, limit the choice of suitable electrolytes [14, 105].

Given the abovementioned issues related to the use of a liquid electrolyte, many solid-state electrolyte supercapacitors have been presented as a possible solution to overcome these limitations.

In general, in these devices, a solid or gel polymers is used as electrolyte, but the poor ionic conductivity at room temperature typical of these chemical compounds seriously limits their performance [103].

As in the case of EDLCs capacitors, the use of electrodes engineered with nanomaterials can partially solve this issue. In fact, Yang et al. [10], have demonstrated that the ionic mobility of the electrolyte can be substantially improved by using a graphene-flakes doping.

6.2.2 Solid-State supercapacitors

Solid-state supercapacitors employing conventional dielectric layers, as opposed to electrolytes, to store the charges, could be an interesting alternative to realize devices working at high frequency that can be integrated in a conventional IC process [14]. The most common architecture of a dielectric solid-state supercapacitor involves the coating of high aspect-ratio electrodes (deep silicon trenches, porous structures or carbon nanotubes) with an insulating material and a conductive layer that works as counter electrode [2, 14, 106–111]. Such electric components are very attractive as power sources because the physical, rather than chemical mechanism of energy storage avoids among others, hysteresis, short cycle-life and low rates of charge and discharge. In fact, compared to a conventional electrochemical supercapacitor that stores charges using electric double layers or faradaic mechanism, a dielectric solid-state supercapacitor uses only surface charge to accumulate the power. The main limitation to the use of solid-state supercapacitors is then the low energy density due to the limited electrodes surface area generally available.

6.3 High aspect ratio 3D electrodes for supercapacitors

As pointed out in the previous sections, dielectric solid state supercapacitors are quite interesting as storage device to be integrated *directly* on chip. However, their energy density is still quite low if compared to electrochemical supercapacitors.

A typical architecture of integrated dielectric supercapacitor is the Metal Insulator Metal (MIM) one [108–110]. The small size, the relatively simple fabrication process and their high reliability make them appealing for large scale application such as decoupling of CMOS microprocessor units [107–109]. These high speed ICs often require large amount of current in bursts, generating switching noise. To protect the electronics, large decoupling capacitors are used which require large -and costly- physical space on the chip. A single high capacitance device could then be placed directly on the die, freeing space for other components. Although they can be fabricated with IC technology [2, 107–110], , still present drawbacks such as low specific capacitance [109], or limited operating range of frequency (less than 200 Hz) [2].

6.3.1 CNTs as electrodes

As demonstrated by [2, 14, 106–111] high aspect-ratio nanostructures can be effectively used as large surface area electrodes. Among the materials used

for this application, carbon nanotubes are the ideal candidates to realize a scaffolding that effectively enhances the surface area of the supercapacitor.

For example, by using ALD coatings on singlewalled CNTs, a high volumetric capacitance of $20\text{mF}/cm^3$ has been obtained by Pint et al. [14], but at high frequency ($\geq$ 10 KHz) the impedance of these devices significantly deteriorates.

6.3.2 Atomic layer deposition in high aspect ratio supercapacitors

Due to its intrinsic high conformality and the high quality of the deposited layers, the atomic layer deposition technique is the most suitable technology to coat high aspect ratio nanostructures, such as porous electrodes or carbon nanotubes bundles [2, 14, 98].

Atomic layer deposition (ALD) has emerged as an important technique for depositing thin films for a variety of applications. The International Technology Roadmap for Semiconductors (ITRS) has included ALD for high dielectric constant gate oxides in the MOSFET structure and for copper diffusion barriers in backend interconnects [113, 114]. In addition, ALD has met challenging requirements in other areas including the deposition of high quality dielectrics to fabricate trench capacitors for DRAM [115].

ALD is able to meet the needs for atomic layer control and conformal

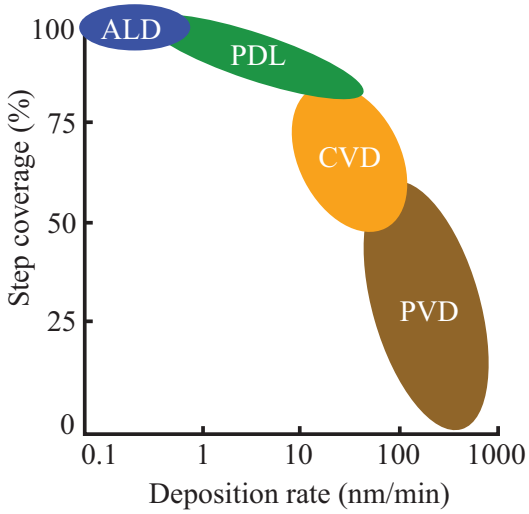

Figure 6.3: Step coverage and deposition rate Vs. deposition technique [112].

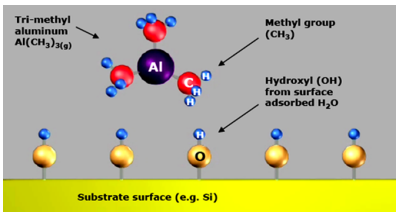

(a) *Trimethylaluminum injection in the chamber.*

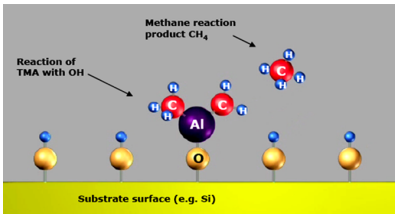

(b) *Reaction with the OH-groups and methane formation.*

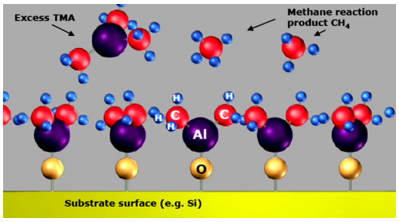

(c) *Saturation of all the surface sites.*

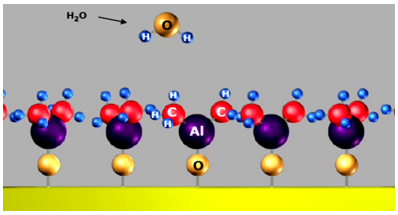

(d) *Water injection in the chamber.*

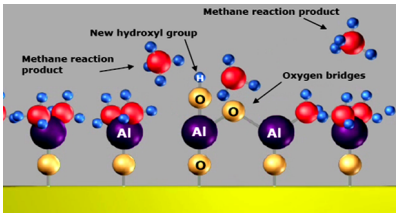

(e) *Formation of new hydroxyl groups.*

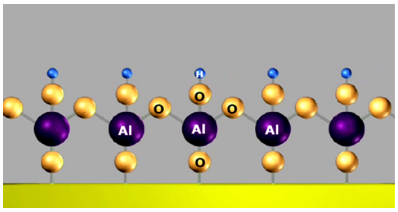

(f) *Saturation of all the surfaces sites.*

Figure 6.4: Different steps of the atomic layer deposition of Aluminum oxide [116].

deposition using sequential, self-limiting surface reactions (see Fig. 6.3). This process is based on binary reaction sequences where two surface reactions occur and deposit a binary compound film. Because there are only a finite number of surface sites, the reactions can only deposit a finite number of surface species. If each of the two surface reactions is self-limiting, then the two reactions may proceed in a sequential fashion to deposit a thin film with atomic level control. The self-limiting aspect of ALD also leads to excellent step coverage and conformal deposition on high aspect ratio structures. Some surface areas will react before other surface areas because of different precursor gas fluxes. However, the precursors will adsorb and subsequently desorb from the surface areas where the reaction has reached completion. The precursors will then proceed to react with other unreacted surface areas and produce a very conformal deposition.

A schematic showing the sequential, self−limiting surface reactions for Aluminum Oxide ALD deposition is displayed in Figure 6.4. The deposition process starts with the injection of the first precursor (Tetramethylaluminum, TMA) and with its reaction with the oxydryl groups that naturally terminate the silicon surface (see 6.4 a-c)). Once the precursors pulse is finished, a purging flow of nitrogen is injected in the chamber to evacuate all the residual TMA vapor.

After this step, the second precursor, in this case water, is injected into the chamber and starts reacting with the H-C-H groups left by the first precursor (see Fig. 6.4 d-e)). The by-product of the reaction (in this particular case methane) is continuously evacuated to prevent any stagnation phenomena. Once the reaction is terminated, a first monolayer of aluminum oxide is formed. The deposition continues with a new purging flow of nitrogen in the chamber and then with injection of the first precursor.

The self-limiting nature of the surface reactions also produces a nonstatistical deposition because the randomness of the precursor flux is removed as an important factor. As a result, ALD films remain extremely smooth and conformal to the original substrate because the reactions are driven to completion during every reaction cycle. Because no surface sites are left behind during film growth, the films tend to be very continuous and pinhole-free. This factor is extremely important for the deposition of excellent dielectric films.

6.3.3 A supercapacitor based on ALD coated CNTs

By using ALD to deposit Aluminium Oxide (Al_2O_3) as dielectric layer and Titanium Nitride (TiN) as high aspect-ratio conformal counter-electrode on 2 μm long MWCNT bundles, a three-dimensional nanostructured capacitor array based on double conformal coating of Multiwalled Carbon Nanotubes

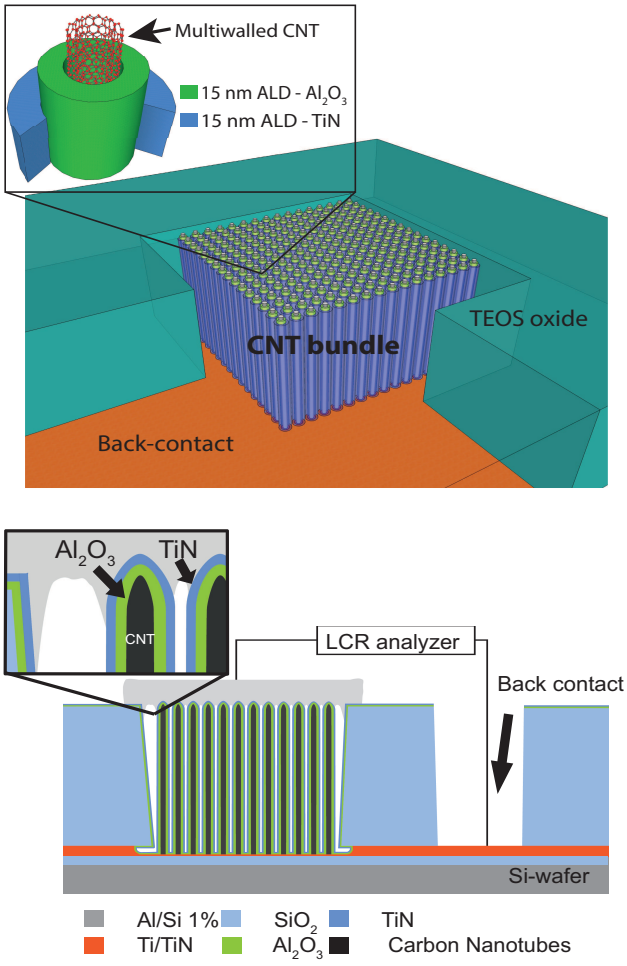

Figure 6.5: Left) A 3D view of the nanostructured capacitor array. The coated CNTs bundle is buried in a TEOS oxide layer. The inset shows a detail of the double ALD coating of the CNTs. Right) Cross-section view of the device.

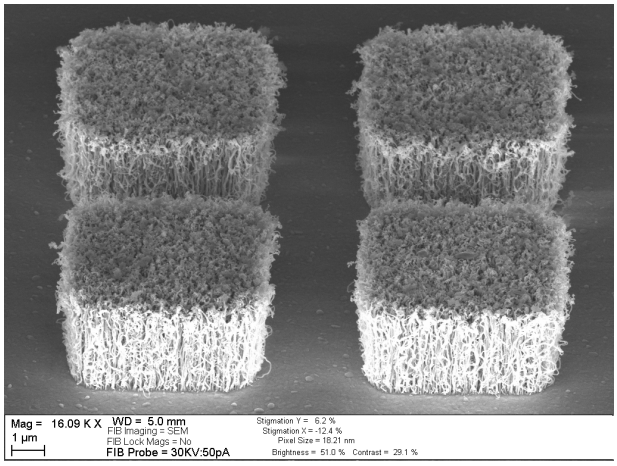

Figure 6.6: High resolution SEM images of ALD coated carbon nanotubes bundles.

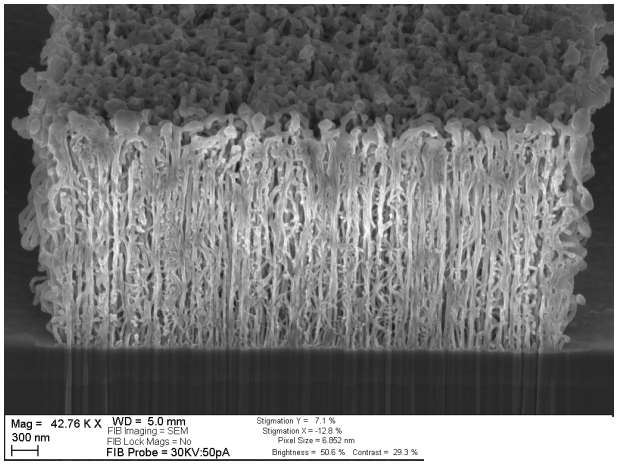

Figure 6.7: FIB cross-section of one bundle.

(MWCNT) bundles has been realized. The devices have a small footprint (from 100 μm^2 to 2500 μm^2) and are realized using an IC wafer-scale manufacturing process with high reproducibility ($\leq 0.3E-12$F deviation).

As shown in Fig. 6.5 the carbon nanotubes bundles form the first electrode, while the Al_2O_3 and TiN, both deposited by Atomic Layer Deposition (ALD), are used as dielectric and high aspect-ratio conformal counterelectrode, respectively. No functionalization is used to achieve a conformal coating of the CNTs, probably due to the presence of defects that act as nucleation sites for the ALD growth [111]. An example of ALD coated CNTs bundles is given in Figs. 6.6 and 6.7.

6.4 Conclusions

In this chapter the existing types of supercapacitors have been briefly introduced. The advantages and drawbacks related to their use for different applications have been discussed. To overcome some of the abovementioned limitations, a new design of a fully solid state supercapacitor has been presented. This device exploits the large surface area given by dense CNTs bundles to realize a high aspect ratio counterelectrode.

The electrical performance of these devices will be presented in the next chapter, together with a complete characterization of the materials employed for their fabrication.

7

A fully solid state nanostructured supercapacitor : Design and fabrication

In this chapter the fabrication, modeling and characterization of a fully solid state (dielectric) supercapacitor is presented. A significant increase of the capacitance due to the enhancement of the electrodes surface area is observed. The effect of the ALD gas precursors diffusion into the CNTs bundles is studied. Optical, chemical characterization of the material is carried out. Finally, a study on the dielectric breakdown of the device has been performed, relating the observed dielectric coating defects to the measuredobserved electrical data.

7.1 Device layout

Three device sets with an area of 100 μm^2, 625 μm^2 and 2500 μm^2 were fabricated based on the design depicted in Fig. 6.5.

In order to estimate the maximum theoretical capacitance of the capacitor a simple electrostatic model has been implemented. As depicted in Fig. 6.5, the ALD coating on the CNTs generates a high aspect-ratio counter-electrode with enhanced surface. However, every single multiwalled nanotube consist of a series of coaxial carbon nanotubes that generates a more complex structure. Previous theoretical work [117] estimates that the charge distribution on a multiwalled CNT is mostly concentrated on the CNT's outer shell. The contribution given by the single nanotube can be therefore calculated by considering it a cylindrical capacitor :

$$C_{CNT} = \frac{2\pi\epsilon L}{ln(\frac{r_{out}}{r_{in}})} \tag{7.1}$$

Where L is the length of the nanotubes, r_{in} is the average CNT radius $(7.5 - 10$ nm) and r_{out} is the external cylinder radius obtained by summing r_{in} and the Al_2O_3 thickness. The overall counter electrode area is then calculated considering a density of $10^{10} - 10^{11}$ $\frac{CNT}{cm^2}$. The ratio between the

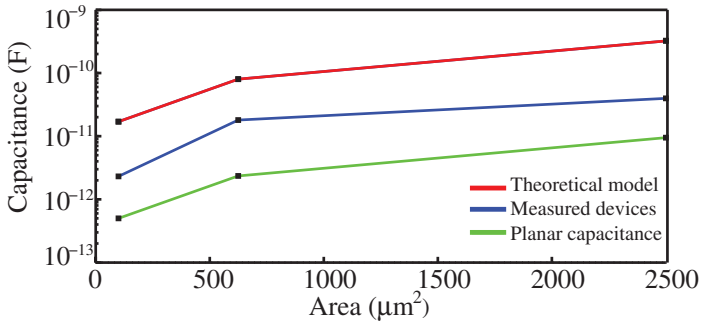

Figure 7.1: Measured and theoretical capacitance VS device area. The green line is the capacitance of a conventional planar capacitor with the same footprint of the realized device. The blue line is the measured capacitance of the ALD-CNT enhanced capacitor and the red line represent the theoretical capacitance of the ALD-CNT capacitor that fully utilize the large surface area offered by the CNTs. The capacitance trend of the measured device (blue curve) is consistent with the predictive model (red curve), while it is clear that the ALD coating process does not completely exploit the CNT surface area, resulting in a lower device capacitance.

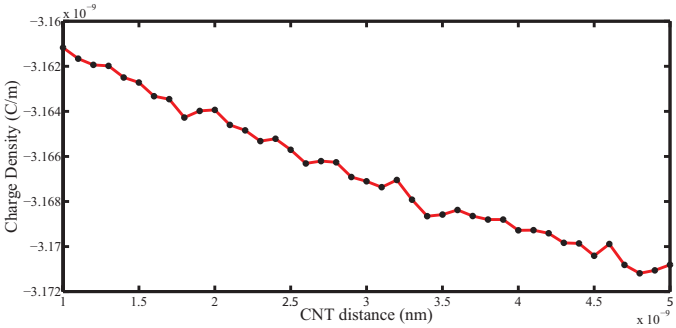

Figure 7.2: The charge density profile on the TiN counter-electrode. The short range interaction between two adjacent CNT gives a reduction of less then 0.35 % of the charge density.

bundle and the planar capacitance of an equivalent planar capacitor of the same footprint is then calculated. Using an average CNT diameter of 15 nm, a thickness of the dielectric layer of 15 nm, a bundle length of 2μm and a dielectric constant of 8.5, the average C_{bund}/C_{plan} ratio is 34. From the capacitance measurements the best C_{bund}/C_{plan} ratio obtained is 5 (625 μm^2 sample). The comparison between theoretical and measured capacitance, together with the values for the corresponding footprint equivalent planar capacitors, are reported in Fig. 7.1. Although the measured devices show a constant capacitance enhancement when compared to the planar capacitance, the theoretical enhancement that could be achieved for a complete coating of the CNTs (red curve) indicate much higher capacitances. A possible explanation can be related to a limited contribution of the CNT surface area, due to incomplete coating of both dielectric and top electrode layers.

Due to the nanometric distance between the coated CNTs, the electric field generated between the coated CNTs can represent a not negligible contribution to the total capacitance calculation. This effect has been evaluated using *Comsol Multiphysic* 4.3 simulation tool. On a single unit cell composed by two CNT covered by alumina and TiN, a voltage drop of 1 V has been applied and the relative charge density has been plotted as a function of the distance between the tubes. The carbon nanotube has been simulated as a simple metal layer with a fixed conductivity. The simulation shows that the charge density is constant in the range $5 - 30$ nm, indicating no significant interaction between the electric fields generated cross the tubes. Changing the average distance between the tubes from 1 to 5 nm

(see Fig. 7.2) the charge density is decreased by 0.35 %. From this simulation results that the small-range interaction between the tubes gives a very limited contribution on the computed capacitance value.

7.2 Device fabrication

The capacitors were realized starting from MWCNT bundles that work as first electrode. A 100 mm p−type Si wafer substrate was coated with a 500 nm tetraethyl orthosilicate (TEOS) oxide to electrically insulate the silicon from the top layers. A stack of 500 nm of Ti and 50 nm of TiN was then sputtered using a Trikon (SPTS) Sigma sputter coater. A 2 μm layer of tetraethylorthosilicate (TEOS) oxide was then deposited using a Novellus Concept One PECVD reactor. The wafer was then coated with 1.5 μm AZ nLOF2020 negative resist, exposed and developed to define the cavities in which the CNTs are later grown. The exposed oxide was etched using a Drytek etcher with fluorine chemistry.

7.2.1 CNT

As catalyst for the CNTs growth, Fe deposited in a Solution CHA e-beam evaporator and patterned by lift-off process, was used. The CNTs were then grown at 500 °C in a BlackMagic Pro 4″ inch CVD reactor. More details on the CNTs growth process can be found in Ref. [118]. The direct use of a dense (10^{11} CNT·cm^{-2}) MWCNT bundle as electrode is one of the key step to achieve a very high capacitance density device. From HRTEM analysis the average CNT diameter is 15 nm (Fig. 7.3). The raw CNT Raman spectra show that the average ratio between D and G band intensities is 1.10±0.01 using multiple measurements and averaging. As previously shown by Tuinstra and Koenig [119] this ratio can be related to the electron mean free path L_a by :

$$\frac{I(D)}{I(G)} = \frac{C(\lambda)}{L_a} \tag{7.2}$$

Where $C(\lambda)$ is 4.4 nm for $\lambda = 514$nm, the laser wavelength used in our Raman spectroscopy setup. This ratio results an average mean free path of ≈ 4 nm.

7.2.2 ALD alumina and titanium nitride

The capacitor dielectric is a 15 nm thick layer of Al_2O_3 deposited by means of ALD technique, using an ASM F-120 reactor. With the same technique, a conformal counter electrode, a 15 nm thick layer of TiN, was then deposited. The precursor used were Trimethylaluminium (TMA) and deionized water (H_2O) for the Al_2O_3 (15 nm) while for the TiN we used $TiCl_4$ and NH_3.

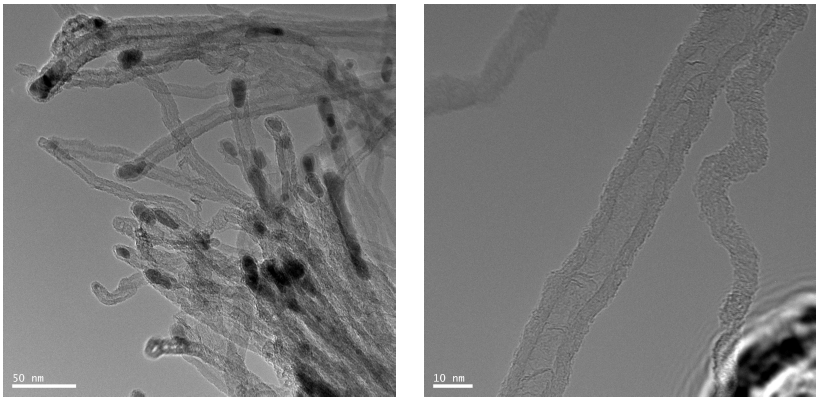

(a) **(b)**

Figure 7.3: : a) HR-TEM of the CNT. The black spot inside the CNT are the iron catalyst particle. b) The average CNT diameter is 15 nm.

The counter-electrode was then covered by a 2 μm layer of Al/Si to provide a robust electrical contact between the nanostructure and the measurement probes, while the back electrode was contacted through an opening in the oxide, as indicated in Fig. 6.5.

The deposition of Aluminum Oxide and Titanium Nitride was carried out increasing the exposure time of the MWCNTs to each of the precursors. To allow a complete depletion of the reaction products inside the dense bundles, the time of the purging step was consequently increased. No special functionalization steps were necessary to ensure the coating of the nanotubes.

The optical properties of the ALD layers were analyzed by means of spectroscopic ellipsometry. The refractive index of the Al_2O_3 films has been extracted using a Cauchy dispersion relationship with Urbach absorption :

$$n(\lambda) = a_n + \frac{b_n}{\lambda^2} + \frac{c_n}{\lambda^4} \tag{7.3}$$

$$k(\lambda) = a_k exp[b_k(\frac{1}{\lambda} - \frac{1}{c_k})] \tag{7.4}$$

and found to be in the 1.5-1.7 range from 1600 nm to 300 nm (see Fig. 7.4), as previously reported [120]. The growth rate at 300 °C was 0.11 $^{nm}/_{cycle}$. Similar analysis has been performed on the TiN layer. To

extract the thickness and the optical properties of the layer (see Fig. 7.5), a Drude-Lorentz dispersion relationship was used :

$$(n+ik)^2 = \epsilon(\omega) = \epsilon_\infty - \frac{\omega_{pu}^2}{\omega^2 - i\Gamma_D\omega} + \sum_{j=1}^{2} \frac{f_j\omega_{oj}^2}{\omega_{oj}^2 - \omega^2 + i\lambda_j\omega} \tag{7.5}$$

where in the Drude contribution $\hbar\omega_{pu}$ is the unscreened plasma energy and Γ_D a damping factor. The factor ω_{pu} depends on the concentration of the conduction electrons :

$$\omega_{pu} = \sqrt{\frac{Ne^2}{\epsilon_0 m^*}} \tag{7.6}$$

where N is the density of conduction electrons, e is the electorn charge, ϵ_0 is the permittivity of the free space and m^* is the effective mass. The Lorentz oscillators are described by their energy positions $\hbar\omega_{oj}$, oscillator strength f_j , and damping (broadening) factor γ_j. Finally, ϵ_∞ is a background constant, larger than unity due to the contribution of the higher-energy transitions that are not taken into account by the two Lorentz terms [121].

The extracted growth rate of TiN is between 0.02 and 0.04 $^{nm}/_{cycle}$, which is consistent with values reported in literature [122].

The resistivity of this layer was measured using four-probe technique and found to be 300 $\mu\Omega$·cm, slightly higher than what reported in previous work [123]. The relevant material properties are summarized in Table 7.1 and 7.2.

To further investigate how the different deposition parameters affect the stoichiometry of the layers, a complete chemical analysis by means of XPS has been performed. In Fig. 7.6 a) the XPS depth profile of the alumina layer is shown. The chemical constituents (aluminum and oxygen) are indeed in the 2:3 ratio, as expected by the nominal alumina stoichiometry. The XPS depth profile (see 7.6 b)) of the TiN shows that in the overall length of the sample there is presence of oxygen.

A more detailed analysis of the binding energies of the Titanium is reported in Figure 7.7. The $Ti2p$ peak typical of TiN [[124]] is clearly present at 455 eV (Fig. 7.7), and a shoulder centered around 458 eV is present as well. This feature is a common signature of the $Ti2p$ related to $TiOx$ [125]. From the depth profile analysis it appears that the first $1-2$ nm of TiN is mostly $TiOx$. In Fig. 7.7 a clear shift of the $Ti2p$ peak from 458 eV towards 455 eV is observed, indicating that TiN layer starts prevailing on the $TiOx$. The presence of the initial titanium oxide layer is

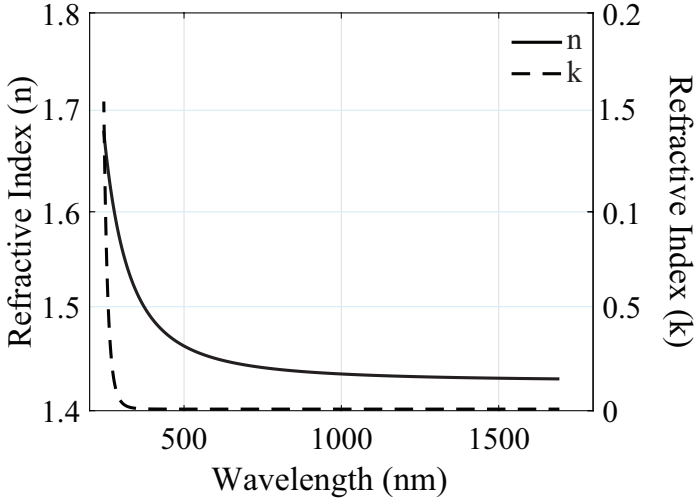

Figure 7.4: Refractive index of the ALD Al_2O_3 layer. The optical properties have been modeled with a Cauchy dispersion law.

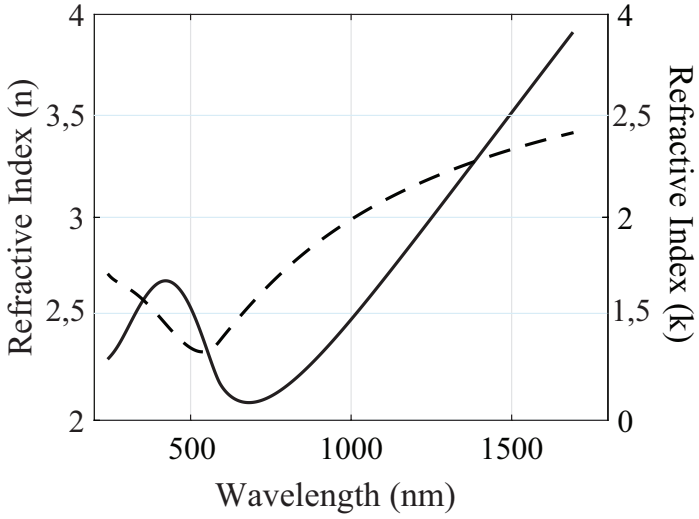

Figure 7.5: Refractive index of the ALD TiN layer. The optical properties have been modeled with a Drude oscillator and two Lorentz oscillators.

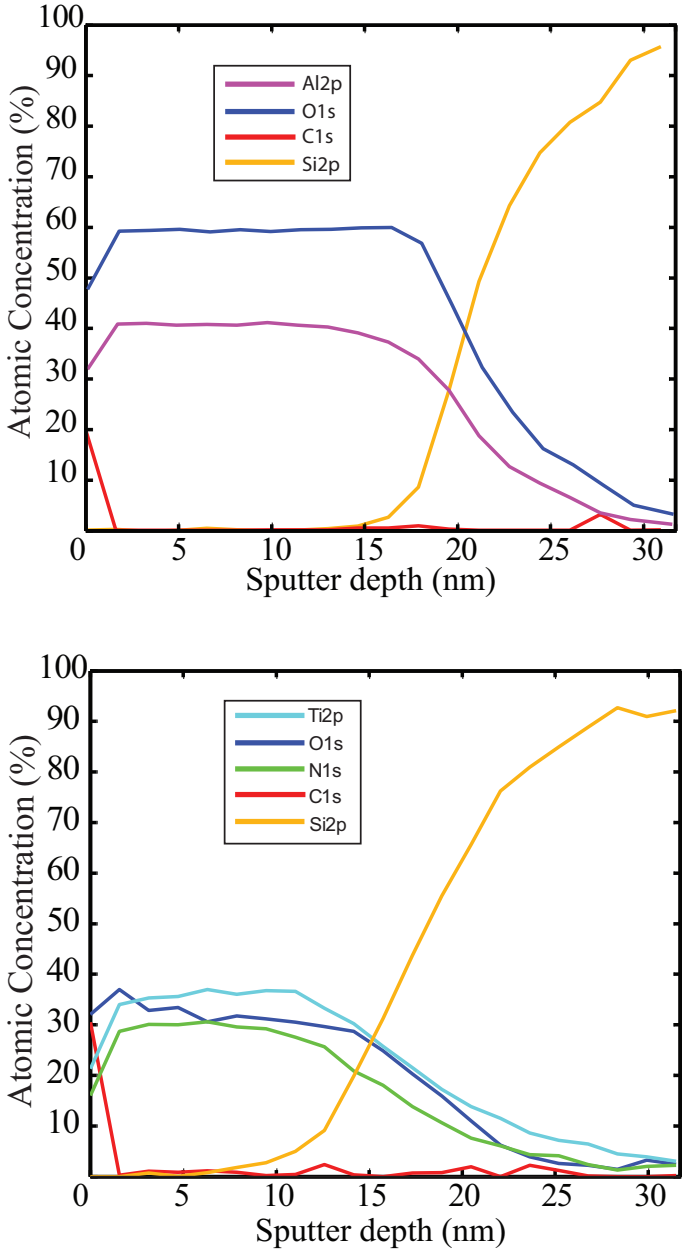

Figure 7.6: : XPS depth profile of 15nm thick Al_2O_3 (Top) and TiN (Bottom)layers. The Al_2O_3 and TiN layer constituents are in the expected ratio 2:3 and 1:1, respectively. In the TiN layer, presence of oxygen, which is responsible for an increase in resistivity for the very thin layers, is observed.

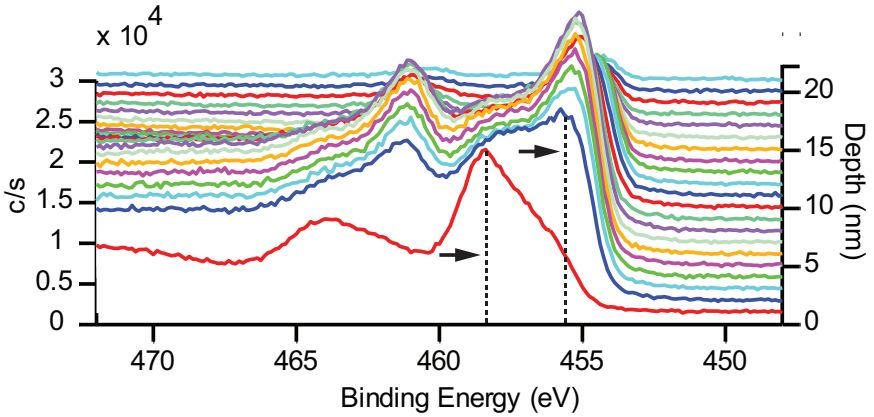

Figure 7.7: XPS depth profile of Titanium Ti2p line of the TiN sample. The dashed lines show the shift of the binding energy of the $Ti2p$ line.

	Precursor A	*Purge A*	*Precursor B*	*Purge B*
Al_2O_3	TMA		H_2O	
$Time(s)$	2	6	2	8
TiN	$TiCl_4$		NH_3	
$Time(s)$	4	12	4.8	8

Table 7.1: Deposition conditions of the ALD Al_2O_3 and the TiN layers

responsible for the increase in resistivity observed in this very thin layers, as compared to values reported for thicker layers [123].

To further confirm the CNTs are effectively coated by alumina, EDX analysis was performed on ALD Al_2O_3 coated CNT. In Fig.7.8 (Top), a high resolution image of a coated CNT is shown. The total thickness of the coated CNT is $\approx$ 47nm. The elemental counts image (Fig. 7.8 Bottom) show that a $\approx$ 15 nm thick layer of Al_2O_3 is indeed present around the CNT structure. Previous studies have shown that the ALD coating of the CNTs requires a chemical pretreatment to promote the anchoring of the ALD precursors to the CNTs surface. However, defects of the CNTs morphology can work as nucleation sites for the ALD precursors, leading to a more uniform coating [14], [111]. The low temperature process ($500°C$) we used to grow CNTs could be responsible for the large presence of defects of the nanotubes [111]. In the center area of the graph the carbon count is

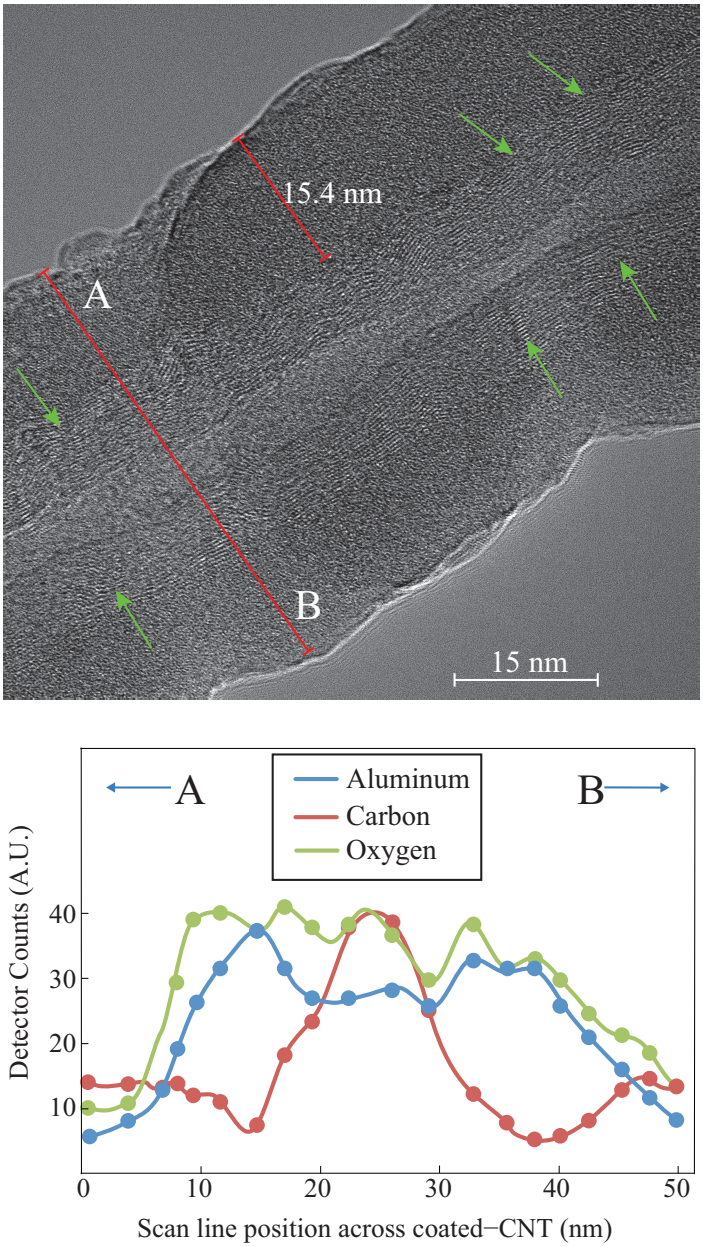

Figure 7.8: Top) HRTEM image of Al_2O_3 coated CNT. The multiwall structure of the tube is clearly visible (green arrows). The ALD coating is cleary visible around the CNT. The red line (AB) shows the EDX scan region. (Bottom) Elemental count vs position graph (Line AB).

Material	Al_2O_3	TiN
Temperature	300°	400°
Pressure	1 $Torr$	1 $Torr$
$Growth - rate$	0.9 $^{nm}/_{cycle}$	0.019 $^{nm}/_{cycle}$
Refractive index	1.61 *at* 633 nm	1.92 *at* 633 nm
Density	2.3 $^{g}/_{cm^3}$	4.8 $^{g}/_{cm^3}$
Stress	300 ± 60 MPa $(tensile)$	400 ± 60 MPa $(tensile)$
Resistivity	—	300 $\mu\Omega \cdot cm$
Dielectric constant	8.5	—

Table 7.2: The optical, mechanical and electrical properties of the Al_2O_3 and TiN layers

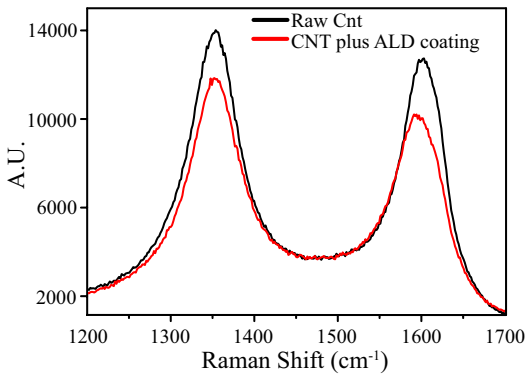

Figure 7.9: Raman spectra performed on the CNT after the alumina coating. As can be seen from the characteristic D band (1350 cm-1) and G band (1580 cm-1), only minor changes on the spectra are visible after the ALD deposition.

significantly large, due to the presence of the CNT. The multi-walled structure of the tube is now clearly visible. The TEM analysis indicate that the spacing between the CNT shells is 0.34 nm. To confirm that the nucleation of the Al_2O_3 preserve the morphology and the physical properties of the CNT, Raman spectroscopy on the coated nanotubes has been performed and reported in Fig. 7.9.

No relevant changes of the spectra of the CNTs occur during the ALD alumina deposition, suggesting that the CNTs are not damaged by the ALD process.

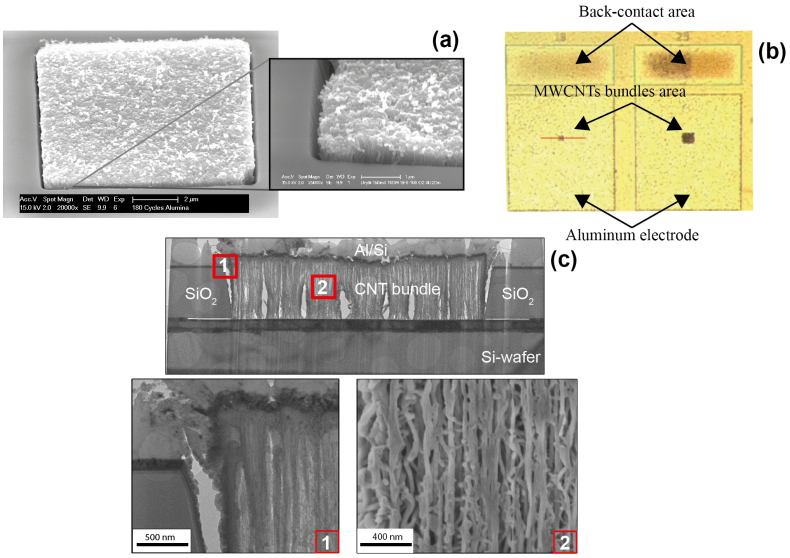

Figure 7.10: a) Top view of the CNTs bundle after the double ALD coating; b) Optical micrograph of the capacitors. Two different bundles sizes ($10x10$, and $25x25$ μm^2) are shown. The red line indicates the cross section for the TEM . c) TEM cross-section of the device . The close ups corresponding to the positions 1 and 2 clearly show the ALD coating on the CNTs.

In Fig. 7.10 (a) the capacitor array after the double coating process with a close-up on the corner of the structure, showing the high density of the CNT bundle in the inset. The device top view is shown in Fig. 7 b). Clearly visible in the figure are the CNT bundle area and the back contact openings. Using a thin lamella prepared by FIB ion milling (see the red cut line in Fig 7b)), a final TEM cross section was then performed to show the internal structure of the capacitor (Fig.7.10 c)). The top part of Fig. 7.10 shows the overall device (here the 100 μm^2 sample) structure while the two insets show the detail of the coating and the porous structure of the CNT bundle.

7.3 ALD precursors diffusion in CNTs bundles

Calculations based on the presented model show that the nanotube coating is effective in the first $300 - 350$ nm of the bundles, while the deepest part of the bundle is partially inaccessible to the ALD precursor gas.

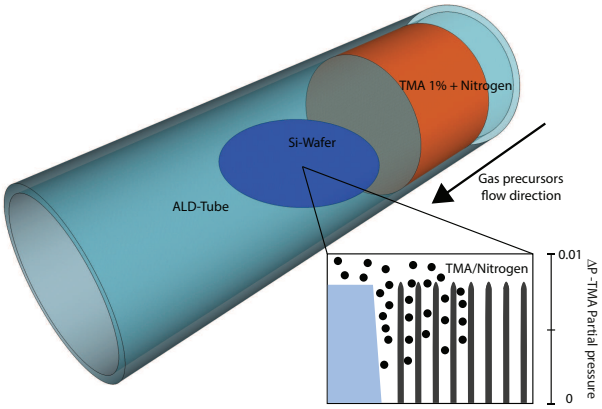

Figure 7.11: Gas diffusion inside the CNT bundle. The 3D model depicts schematically the diffusion process. During the TMA (or other precursors) pulse, the gas molecules are carried together with the nitrogen carrier gas. The diffusion is mainly driven by the partial pressure of the precursor inside the gas mixture (typically from 1% to 3%).

To explain this phenomenon an ALD precursor gas diffusion model into the CNT bundle was developed (see Fig. 7.11). The gas diffusion through a CNT membrane has already been described in [126], mainly to analyze the filtration properties of this material. Due to dense porous structure of the bundles, gas transport is a combination of surface diffusion, Knudsen diffusion, and viscous flow. However, when the mean free path of the diffusion species is larger than the pore diameter of the membrane, Knudsen diffusion becomes prominent, and there are more collisions with the pore walls than those among gas molecules. The gas (here in particular is represented the diffusion of the TMA precursor) mean free path in our ALD reactor can be estimated in $\lambda = \frac{RT}{\sqrt{2}\pi N_A d^2 P} = 1.35^{-5}$m, that is 4 order of magnitude larger than pore dimension. This implies a Knudsen diffusion mechanism since the ratio $\lambda/d_{pore} >> 1$ [126]. In this diffusion regime, the molar flux can be obtained from Fick's law as:

$$N_a = \frac{\epsilon D_K \Delta P}{RTLp^{-\frac{1}{2}}} \tag{7.7}$$

where ϵ is the porosity, D_K the Knudsen diffusion coefficient, ΔP is the pressure drop, R the universal gas constant, T the absolute temperature and p the porosity (estimated by the CNT density). The resultant molar flux is

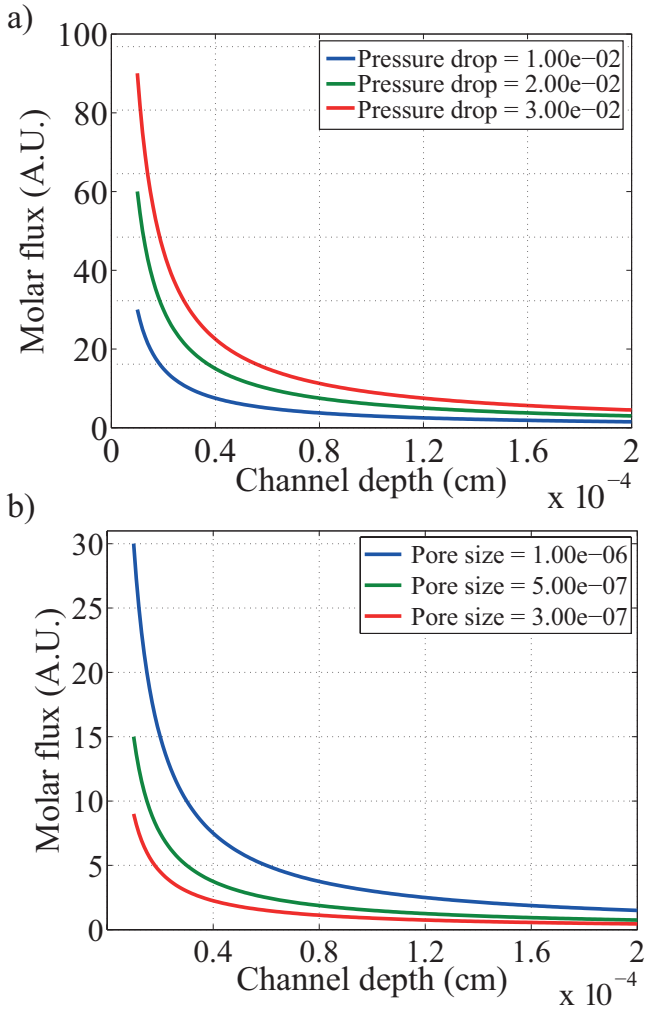

Figure 7.12: : Top) The molar flux is depicted for an average pore dimension of 10 nm. The molar flux drastically reduces of a factor 5 at 400 nm. Bottom) Molar flux calculated for different pore dimension, corresponding to different thickness of the deposited dielectric.

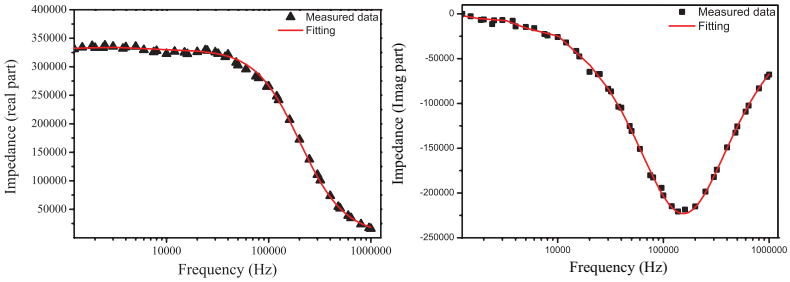

Figure 7.13: Impedance of the capacitor array. Both real (left) and imaginary part (right) are shown. The device presents the typical behaviour of a capacitor in the entire frequency range under study.

represented in Fig. 7.12 (a). As can be noticed, the molar flux drastically decreases of a factor 5 at 400 nm, suggesting a lower penetration of the gases inside the bundle. The comparison between electrical measurements and the gas diffusion model, confirms that the ALD deposition has been effective in sufficiently covering the first $350 - 450$ nm of the CNTs inside the bundle.

It is important to underline that the diffusion profile in Figure 7.12 a) depicts the molar flux during a single ALD cycle. In fact, due to the layer-by-layer deposition, characteristic of ALD, the pore dimension decreases, giving a different diffusion profile of the molar flux. To show how this phenomena can affect the diffusion profile, three different pore dimensions have been chosen (10, 5 and 3 nm) and the relative molar flux estimated (see Fig. 7.12 b)). The linear dependence of the molar flux from the pore size determines a consequent reduction of the gas precursors quantity flowing inside the CNT bundle. Eventually, the reduction of the pores dimensions and the consequent low amount of precursors diffusing in the cavity can generate very thin layers of alumina at the bottom of the CNT bundles that, as observed, can cause a dielectric breakdown of the device even at the relative low voltages used ($1.1 - 1.3$ V).

7.4 Measurements and results

7.4.1 Impedance

Impedance measurements using a conventional LCR meter were carried out. Three device sets with different area (100 μm^2 to 625 μm^2 and 2500 μm^2) are here presented to study the effect of device scaling on its performance. Prior to any measurement, an open calibration step was performed to cancel

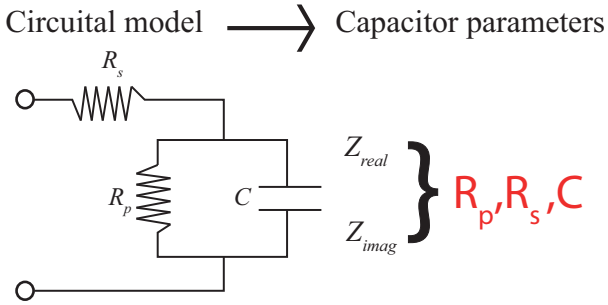

Figure 7.14: The parameters C (capacitance), R_s (series resistance) and R_p (parallel resistance) are extracted fitting the impedance data with a model that accounts for leakages due to the not ideal behaviour of the dielectric layer.

the contribution of any parasitic component of the measurement system. In Fig. 7.13, a typical measured impedance curve of the realized capacitor is presented. The device is purely capacitive over the entire frequency range under study (10^3-10^6 Hz). This behavior represents a significant improvement respect to previously presented work (see for example Ref. [14]), where at high frequency no simple circuital model was able to explain the observed curves. The real and the imaginary part of our device impedance can be instead effectively modeled using a simple circuit scheme as depicted in Fig. 7.14. According to this, the impedance can be written as:

$$Z_{real} = R_s + \frac{R_p}{1 + \omega^2 C^2 R_p^2} \tag{7.8}$$

$$Z_{imag} = -\frac{\omega^2 R_p^2}{1 + \omega^2 C^2 R_p^2} \tag{7.9}$$

where C represents the capacitance component of the device, ω is 2π times the frequency, R_p is a resistor that takes into account the leakage component eventually present, while R_s is the series resistance of the capacitor. In table 7.3 the best-fit parameters of the capacitors impedance are reported. The relevant capacitors parameters were extracted from the presented model to take into account the non-ideal behavior of the capacitors. Discontinuous or locally thinner Al_2O_3 layers can indeed generate an unwanted resistive behavior due to the electrical shorts between the capacitors electrodes, thus explaining the observed impedance curves. The non-uniform coating of the overall length of the CNTs was probably related to the relatively high base pressure (1 Torr) inside our ALD reactor which

Table 7.3: Capacitor array best fitting parameters. The very high parallel resistance of the 100 μm^2 indicates a very small number of defects in the aluminum oxide layer.

$Area$ (μm^2)	C (F)	R_s (Ω)	R_p ($k\Omega$)	$C - C_{avg}$ (F)
100	$2.5E-12$	3500	719	$\pm 0.03E-12$
625	$1.17E-11$	110	11	$\pm 0.05E-11$
2500	$1.06E-10$	800	0.8	$\pm 0.12E-10$

limits the precursors diffusions through the CNT bundles, and the limited percentage of gas precursors injected in the chamber during each ALD cycle. From the data reported in Table 7.3 it is clear that the devices with the smaller area (100 μm^2) present a very high parallel resistance (in the order 700 $k\Omega$), meaning that the ALD coating of the CNTs has been quite effective. The series resistance of these devices is in the order of 3.5 $k\Omega$. The second device set has a surface area of 625 μm^2, more than 6 times higher than the first device set. These capacitors present a low parallel resistance of 11 $k\Omega$, while the capacitance is almost 5 times higher. The third device set has an area of 2500 μm^2 and a very low parallel resistance of 0.3 $k\Omega$. More than 16 devices for each size were measured on the wafer area and only a small deviation of the capacitance and density values observed, indicating the good reproducibility of the fabrication process. To verify the effective enhancement of the presented design, we compared the obtained values of capacitance with a planar capacitor of the same footprint and evaluated the capacitance density.

The results are summarized in Table 7.3. Compared to the capacitance of a planar device with the same footprint (Fig. 7.1), the ALD coating on the CNTs increases the effective capacitance of a factor $4.2 - 5$.

7.4.2 Dielectric breakdown voltage

The electrical robustness of the capacitors here presented has been evaluated studying the dielectric breakdown voltage (B-V) of the Al_2O_3 layer. Previously reported breakdown field of the aluminum oxide deposited by ALD occurs around 5 $^{MV}/_{cm}$ [127]. However, these measurements have been performed on conventional parallel plate capacitors. In all the measured capacitors the B-V is found to be in the $1.1 - 1.3$ V range at low frequency (1 KHz).

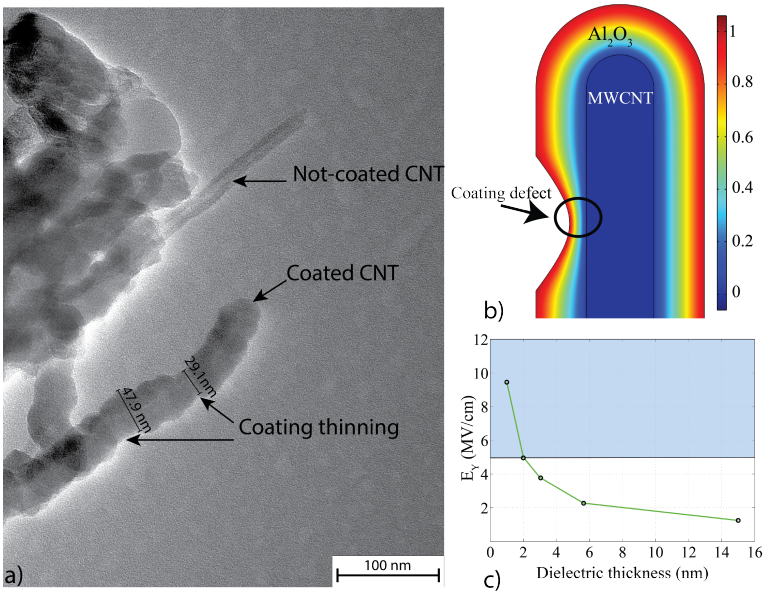

Figure 7.15: a) HRTEM image of the alumina coated tube. It is possible to see that some region of the tube are indeed coated with a thinner alumina layer. b)Dielectric breakdown simulation using *Comsol* 4.3. a)Electric potential of the CNT structure, thinning the Al_2O_3 to simulate a defect in the ALD coating. c)The resultant maximum electric field is then plotted as a function of the thickness. For a 2 nm thick Al_2O_3 layer, the field overcome the value of 5 MV/cm, causing a dielectric breakdown in the layer.

Given the nominal alumina thickness, the resulting electric field inside the alumina layer, should not exceeds 2 MV/cm. However, the ALD coating on CNTs can present imperfections, regions in which the thickness of the layer is reduced that can generate higher electric field between the electrodes. The TEM image in Fig. 7.15 (a) shows a progressive thinning of the Alumina layer on a portion of the coated CNTs. To estimate the critical thickness at which the breakdown occurs, a simulation of the electric field on the CNT- Al_2O_3 interface has been realized using Comsol Multiphysic 4.3 software. As shown in Fig. 7.15 (b) the CNT has been depicted as a simple metal cylinder with a rounded top-side. The cylinder is then covered by a dielectric layer that simulate the Al_2O_3 layer. On the top boundary of the alumina layer the voltage at which the breakdown experimentally occurs is then applied. Using the nominal dielectric thickness of 15 nm and a voltage of 1.1 V, an electric field of 1.8 $^{MV}/_{cm}$ is present at the dielec-

tric/CNT interface that is well below the expected breakdown field. To simulate a defect in the coating, we decreased the thickness of the layer in a small region and consequently we mapped the resulting electric field. Simulations have been performed using 5 different value of alumina thickness, as shown in Fig. 7.15 (c) and we observe a breakdown voltage of 5 MV when the dielectric layer is 2 nm thick. This simulation indicates a possible mechanism to explain the premature breakdown of the fabricated device.

7.5 Conclusions

A 3D solid-state nanostructured capacitor array has been realized by means of atomic layer deposition coating of highly dense CNTs bundles. A 15 nm thick layer of aluminum oxide has been employed as dielectric layer, while a 10 nm thick layer of titanium nitride is deposited as conformal counter electrode on top of the oxide. The ALD coating has been achieved without any chemical pretreatment of the CNTs. Impedance measurements on these devices show that the high aspect ratio design of the capacitor electrodes effectively enhances the capacitor performances up to a factor 5 compared to a planar capacitor with the same footprint. The area enhancement factor has been explained modeling the ALD gas precursors diffusion inside the CNT bundle. The results show that the gas flow undergoes a reduction from $300-350$ nm deep inside the CNT cavity. A second set of simulations show that reduction in the pore size during the ALD deposition implies a reduced flow at the bottom of the cavity, eventually generating very thin dielectric layers. This is supported by the analysis on the dielectric breakdown of the capacitor. Using a finite element model simulation, we show that the observed breakdown voltage ranging from $1.1-1.3$ V can be effectively explained considering a very thin (2 nm or less) alumina layer on the CNT.

Despite these limitations, the device here presented is the first known example of large-scale manufacturable nanostructured capacitors. The very high performance, the relatively simple and easy-to-integrate fabrication process, and the thermal budget required ($500°C$ reached during the CNT growth) make these devices a very interesting alternative to the conventional EDCL capacitors. Further improvements (e.g. a reduction in the CNT density) are required to optimize the capacitance performance preserving at the same time the observed low leakage currents.

In addition, the results of this investigation provide useful insights for the coating of very high aspect ratio nanostructure [128]. This could be of interest in other field of application where high quality coating are required, like study of tribology on MEMS device [129] or the enhancement of optical, mechanical and rheological properties of nanoparticles [130].

8

Conclusions and future work

8.1 Conclusions

The continue route of scaling for electronic devices has clearly shown that new architectures have to be explored to overcome materials physical limitations. The design and fabrication of high aspect-ratio electronic components represent a promising choice to solve these critical issues. In this dissertation we have applied this concept to fabricate a new generation of high aspect-ratio MEMS components. These devices have been designed to enhance the performance of conventional passive elements, particularly high frequency (THz) planar integrated antenna and dielectric solid state supercapacitors.

8.2 Artificial Dielectric Layers for efficient THz integrated planar antennas

The integration of efficient high frequency planar antennas in a conventional CMOS fabrication process is a fundamental task for the realization of high-speed communication links and innovative sensing instruments. However, due to intrinsic material and device physical limitations, high frequency (sub-THz and THz) integrated planar antennas suffer from high losses and very low front-to-back radiation ratio. These issues become a serious limiting factor, especially for THz frequencies, where the generated power by chain amplifiers is already quite low. In this thesis we have introduced a new generation of metamaterials called Artificial Dielectric Layers (ADLs) fabricated by using CMOS compatible technology.

These artificial dielectric layers consist of periodic arrays of metal patches embedded in a dielectric host medium. By selecting PECVD Silicon oxide and pure aluminum as dielectric and metallic material, respectively, we have demonstrated that the performance of integrated planar antennas is highly enhanced (gain improvement of 2 dB for an antenna/ADL system when compared to a conventional antenna).

The mechanical and electrical properties of these materials have been studied and properly tuned to enable the fabrication of the proposed antenna/ADL structure. The residual thermal stress of the silicon oxide has been lowered to -30 MPa, allowing the realization of high-aspect ratio composite membranes. The fabricated membranes present a very low residual buckling, thus ensuring no deformation of the radiation wavefront.

A numerical model has been proposed to characterize and predict the buckling of the antenna/ADL membrane. Measurements of the vertical displacement validate the correctness of the model.

The optical properties of the ADL have been measured using two different methodologies, both confirming the simulated layer properties. The

first one relies on the measurements of the relevant antenna parameters, such as radiation patterns and gain. A direct measurement of the ALD refractive index has been carried out with a Time Domain Spectroscopy (TDS) setup. The results show a very good agreement between simulations and measurements.

The fabrication of ADLs at 0.3 THz requires thick layers of oxide to separate the metal patches. The thickness of the dielectric layers can be reduced by choosing a material with higher refractive index. We demonstrated that PECVD amorphous silicon carbide (SiC) represent a viable alternative to silicon oxide. This material presents very high refractive index in the 0.2-2THz range, with two large bands that can be used for the ADL design. We calculated that a SiC-based ADL, working at a central frequency of 0.45THz, would be 2.44 times thinner than a similar silicon oxide based device.

8.3 Dielectric solid state supercapacitors as efficient on-chip energy storage devices

The realization of high capacitance devices *directly* on chip represents a fundamental step for more performing and battery-lasting electronic devices. This result can be achieved with so called supercapacitors. Conventional supercapacitors, such as electrochemical supercapacitor, can not be directly integrated in an IC process, due to the particular materials and architectures used. Fully dielectric solid supercapacitor represents a viable solution to overcome this limitation.

In this thesis we have demonstrated the fabrication of a fully dielectric solid-state supercapacitor based on the ALD coating of carbon nanotubes. This device has remarkable capacitance values and a large operating frequency range (from 20 to 1 MHz).

We demonstrated that ALD coating can be performed on defective CNTs withouth any chemical pretreatment, usually needed to activate the nucleation surface sites.

An electrical model of the presented capacitor has been introduced.

The measured device capacitance has been correlated to the ALD precursor diffusion inside the CNTs bundle.

By using TEM analysis and numerical simulations, we demonstrated that a possible mechanism behind the observed low dielectric breakdown is the local reduction of the aluminum oxide thickness, due to the ALD coating imperfections.

8.4 Future work

The results and technological advances presented in this thesis open the possibility to realize more efficient passive devices (high frequency antennas and supercapacitors). However, further research is needed in order to obtain fully mature components and commercially viable devices. Suggestions for future research and potential applications that could be considered are given in this Section.

Artificial Dielectric Layers

The measurements of the antenna radiation patterns and gain at THz and sub-THz frequencies remain a challenging topic. The power generated by the amplifier chain remains so low that any loss (conductive, radiative) mechanism becomes relevant and severely degrades the signal transmission. To avoid any frequency and impedance mismatch, the design and fabrication of integrated planar antennas for THz applications requires an extremely accurate control of the etching profile of metal patterns. In fact, unwanted isotropic etch phenomena during the aluminum removal can change the relevant antenna parameters design, such as the slots width. This would results in a shift of the antenna central working frequency and also asymmetry in the radiation patterns.

Although we successfully demonstrated the fabrication of a CMOS compatible metamaterial that enhances the performance of planar integrated antennas, the fabrication process of the ADL remains long and the final membrane very thick. As suggested in Chapter 5, new materials have to be explored. Silicon carbide can represent a viable alternative, but further research is necessary to optimize the fabrication steps of a SiC based ADL.

The fabrication of ADL working at lower frequencies cannot be simply achieved by conventional silicon oxide and metal layers. In fact, the separation between the metal patches would results in an extremely long deposition process, with risks associated to uniformity and wafers mechanical stability. However, by exploring new dielectric layers such as polymers (SU8, PDMS or similar), these issues can be solved. It is then important to study in detail the mechanical and optical properties of these layers.

Nano supercapacitors

In this thesis, the use of ALD layers has been proposed to coat CNTs for the realization of high-aspect ratio nanoelectrodes. Although the device that we presented shows the feasibility of this technique, further research is required to solve the issues related to the uniformity of the ALD coating process for the dense forest of CNTs and the low dielectric breakdown voltage measured.

The diffusion process of the ALD precursors inside the CNTs bundles

needs further investigations to optimize the device capacitance. By realizing a setup similar to the one proposed in [126], it would be possible to directly measure the amount of gas flowing through a dense CNT membrane.

The effectiveness of the ALD coating can be also validated by realizing capacitors with different CNTs bundles height but same footprints. If the measured capacitances values would be the same also for taller CNTs bundles, the maximum precursors penetration depth would have been reached and no further capacitance enhancements could be achieved .

The use of high-aspect ratio scaffolding as CNTs is advantageous for the large surface area offered, but similar nanostructures, such as carbon nanofibers, can be an interesting alternative. In fact, the ALD coating could be more effective in bundles where the density is not that high as in CNTs bundles. This will also bring benefits to the coating uniformity and, consequently, to a larger capacitance enhancement and a higher dielectric breakdown.

Bibliography

[1] I. L. Markov, "Limits on fundamental limits to computation," *Nature*, vol. 512, no. 7513, pp. 147–154, 2014.

[2] P. Banerjee, I. Perez, L. Henn-Lecordier, S. B. Lee, and G. W. Rubloff, "Nanotubular metal–insulator–metal capacitor arrays for energy storage," *Nature Nanotechnology*, vol. 4, no. 5, pp. 292–296, 2009.

[3] J. Klootwijk, K. Jinesh, W. Dekkers, J. Verhoeven, F. Van Den Heuvel, H.-D. Kim, D. Blin, M. Verheijen, R. Weemaes, M. Kaiser *et al.*, "Ultra-high capacitance density for multiple ald-grown mim capacitor stacks in 3-d silicon," *Electron Device Letters, IEEE*, vol. 29, no. 7, pp. 740–742, 2008.

[4] Y. P. Zhang and D. Liu, "Antenna-on-chip and antenna-in-package solutions to highly integrated millimeter-wave devices for wireless communications," *Antennas and Propagation, IEEE Transactions on*, vol. 57, no. 10, pp. 2830–2841, 2009.

[5] H. Li, H.-M. Rein, T. Suttorp, and J. Bock, "Fully integrated sige vcos with powerful output buffer for 77-ghz automotive radar systems and applications around 100 ghz," *Solid-State Circuits, IEEE Journal of*, vol. 39, no. 10, pp. 1650–1658, 2004.

[6] A. Arbabian, S. Callender, S. Kang, M. Rangwala, and A. M. Niknejad, "A 94 ghz mm-wave-to-baseband pulsed-radar transceiver with applications in imaging and gesture recognition," *Solid-State Circuits, IEEE Journal of*, vol. 48, no. 4, pp. 1055–1071, 2013.

[7] P. Yang, Y. Ding, Z. Lin, Z. Chen, Y. Li, P. Qiang, M. Ebrahimi, W. Mai, C. P. Wong, and Z. L. Wang, "Low-cost high-performance solid-state asym-

metric supercapacitors based on mno2 nanowires and fe2o3 nanotubes," *Nano letters*, vol. 14, no. 2, pp. 731–736, 2014.

[8] Z.-S. Wu, A. Winter, L. Chen, Y. Sun, A. Turchanin, X. Feng, and K. Müllen, "Three-dimensional nitrogen and boron co-doped graphene for high-performance all-solid-state supercapacitors," *Advanced Materials*, vol. 24, no. 37, pp. 5130–5135, 2012.

[9] C. Shen, X. Wang, W. Zhang, and F. Kang, "Direct prototyping of patterned nanoporous carbon: a route from materials to on-chip devices," *Scientific reports*, vol. 3, 2013.

[10] X. Yang, F. Zhang, L. Zhang, T. Zhang, Y. Huang, and Y. Chen, "A high-performance graphene oxide-doped ion gel as gel polymer electrolyte for all-solid-state supercapacitor applications," *Advanced Functional Materials*, vol. 23, no. 26, pp. 3353–3360, 2013.

[11] C.-C. Yang, S.-T. Hsu, and W.-C. Chien, "All solid-state electric double-layer capacitors based on alkaline polyvinyl alcohol polymer electrolytes," *Journal of power sources*, vol. 152, pp. 303–310, 2005.

[12] T. Osaka, X. Liu, M. Nojima, and T. Momma, "An electrochemical double layer capacitor using an activated carbon electrode with gel electrolyte binder," *Journal of the Electrochemical Society*, vol. 146, no. 5, pp. 1724–1729, 1999.

[13] C. Meng, C. Liu, L. Chen, C. Hu, and S. Fan, "Highly flexible and all-solid-state paperlike polymer supercapacitors," *Nano letters*, vol. 10, no. 10, pp. 4025–4031, 2010.

[14] C. L. Pint, N. W. Nicholas, S. Xu, Z. Sun, J. M. Tour, H. K. Schmidt, R. G. Gordon, and R. H. Hauge, "Three dimensional solid-state supercapacitors from aligned single-walled carbon nanotube array templates," *Carbon*, vol. 49, no. 14, pp. 4890–4897, 2011.

[15] P. H. Siegel *et al.*, "Terahertz technology," *IEEE Transactions on microwave theory and techniques*, vol. 50, no. 3, pp. 910–928, 2002.

[16] P. H. Siegel, "Terahertz technology in biology and medicine," in *Microwave Symposium Digest, 2004 IEEE MTT-S International*, vol. 3. IEEE, 2004, pp. 1575–1578.

[17] M. Theuer, S. S. Harsha, D. Molter, G. Torosyan, and R. Beigang, "Terahertz time-domain spectroscopy of gases, liquids, and solids," *ChemPhysChem*, vol. 12, no. 15, pp. 2695–2705, 2011.

[18] E. Pickwell and V. Wallace, "Biomedical applications of terahertz technology," *Journal of Physics D: Applied Physics*, vol. 39, no. 17, p. R301, 2006.

[19] B. Hu and M. Nuss, "Imaging with terahertz waves," *Optics letters*, vol. 20, no. 16, pp. 1716–1718, 1995.

[20] C. Rønne and S. R. Keiding, "Low frequency spectroscopy of liquid water using thz-time domain spectroscopy," *Journal of Molecular Liquids*, vol. 101, no. 1-3, pp. 199–218, 2002.

[21] S. Hadjiloucas, L. S. Karatzas, and J. W. Bowen, "Measurements of leaf water content using terahertz radiation," *Microwave Theory and Techniques, IEEE Transactions on*, vol. 47, no. 2, pp. 142–149, 1999.

[22] D. Mittleman, M. Gupta, R. Neelamani, R. Baraniuk, J. Rudd, and M. Koch, "Recent advances in terahertz imaging," *Applied Physics B*, vol. 68, no. 6, pp. 1085–1094, 1999.

[23] R. Woodward, V. Wallace, D. Arnone, E. Linfield, and M. Pepper, "Terahertz pulsed imaging of skin cancer in the time and frequency domain," *Journal of Biological Physics*, vol. 29, no. 2-3, pp. 257–259, 2003.

[24] A. J. Fitzgerald, V. P. Wallace, M. Jimenez-Linan, L. Bobrow, R. J. Pye, A. D. Purushotham, and D. D. Arnone, "Terahertz pulsed imaging of human breast tumors 1," *Radiology*, vol. 239, no. 2, pp. 533–540, 2006.

[25] C. Sirtori, "Applied physics: Bridge for the terahertz gap," *Nature*, vol. 417, no. 6885, pp. 132–133, 2002.

[26] M. Tonouchi, "Cutting-edge terahertz technology," *Nature photonics*, vol. 1, no. 2, pp. 97–105, 2007.

[27] H.-J. Song and T. Nagatsuma, "Present and future of terahertz communications," *Terahertz Science and Technology, IEEE Transactions on*, vol. 1, no. 1, pp. 256–263, 2011.

[28] A. Dobroiu, M. Yamashita, Y. N. Ohshima, Y. Morita, C. Otani, and K. Kawase, "Terahertz imaging system based on a backward-wave oscillator," *Applied optics*, vol. 43, no. 30, pp. 5637–5646, 2004.

[29] M. Mineo and C. Paoloni, "Corrugated rectangular waveguide tunable backward wave oscillator for terahertz applications," *Electron Devices, IEEE Transactions on*, vol. 57, no. 6, pp. 1481–1484, 2010.

[30] W. He, C. Donaldson, L. Zhang, K. Ronald, P. McElhinney, and A. Cross, "High power wideband gyrotron backward wave oscillator operating towards the terahertz region," *Physical review letters*, vol. 110, no. 16, p. 165101, 2013.

[31] A. Roitman, D. Berry, and B. Steer, "State-of-the-art w-band extended interaction klystron for the cloudsat program," *IEEE transactions on electron devices*, vol. 52, no. 5, pp. 895–898, 2005.

[32] T. Saito, N. Yamada, S. Ikeuti, S. Ogasawara, Y. Tatematsu, R. Ikeda, I. Ogawa, T. Idehara, V. N. Manuilov, T. Shimozuma *et al.*, "Generation of high power sub-terahertz radiation from a gyrotron with second harmonic oscillation," *Physics of Plasmas (1994-present)*, vol. 19, no. 6, p. 063106, 2012.

[33] M. T. Faber, J. Chramiec, and M. Adamski, *Microwave and millimeter-wave diode frequency multipliers*. Artech House, 1995.

[34] A. V. Raisanen, "Frequency multipliers for millimeter and submillimeter wavelengths," *Proceedings of the IEEE*, vol. 80, no. 11, pp. 1842–1852, 1992.

[35] S. Martin, B. Nakamura, A. Fung, P. Smith, J. Bruston, A. Maestrini, F. Maiwald, P. Siegel, E. Schlecht, and I. Mehdi, "Fabrication of 200 to 2700 ghz multiplier devices using gaas and metal membranes," in *Microwave Symposium Digest, 2001 IEEE MTT-S International*, vol. 3. IEEE, 2001, pp. 1641–1644.

[36] A. Maestrini, B. Thomas, H. Wang, C. Jung, J. Treuttel, Y. Jin, G. Chattopadhyay, I. Mehdi, and G. Beaudin, "Schottky diode-based terahertz frequency multipliers and mixers," *Comptes Rendus Physique*, vol. 11, no. 7, pp. 480–495, 2010.

[37] B. J. Rizzi, T. Crowe, and N. Erickson, "A high-power millimeter-wave frequency doubler using a planar diode array," *Microwave and Guided Wave Letters, IEEE*, vol. 3, no. 6, pp. 188–190, 1993.

[38] A. Maestrini, J. Bruston, D. Pukala, S. Martin, and I. Mehdi, "Performance of a 1.2 thz frequency tripler using a gaas frameless membrane monolithic circuit," in *Microwave Symposium Digest, 2001 IEEE MTT-S International*, vol. 3. IEEE, 2001, pp. 1657–1660.

[39] F. Maiwald, S. Martin, J. Bruston, A. Maestrini, T. Crawford, and P. H. Siegel, "2. 7 thz waveguide tripler using monolithic membrane diodes," in *IEEE MTT S INT MICROWAVE SYMP DIG*, vol. 1, 2001, pp. 1637–1640.

[40] A. Maestrini, I. Mehdi, J. V. Siles, J. S. Ward, R. Lin, B. Thomas, C. Lee, J. Gill, G. Chattopadhyay, E. Schlecht *et al.*, "Design and characterization of a room temperature all-solid-state electronic source tunable from 2.48 to 2.75 thz," *Terahertz Science and Technology, IEEE Transactions on*, vol. 2, no. 2, pp. 177–185, 2012.

[41] E. Brown, F. Smith, and K. McIntosh, "Coherent millimeter-wave generation by heterodyne conversion in low-temperature-grown gaas photoconductors," *Journal of Applied Physics*, vol. 73, no. 3, pp. 1480–1484, 1993.

[42] E. Brown, K. McIntosh, K. Nichols, and C. Dennis, "Photomixing up to 3.8 thz in low-temperature-grown gaas," *Applied Physics Letters*, vol. 66, no. 3, pp. 285–287, 1995.

[43] K. Yang, P. Richards, and Y. Shen, "Generation of far-infrared radiation by picosecond light pulses in linbo3," *Applied Physics Letters*, vol. 19, no. 9, pp. 320–323, 1971.

[44] H. Luo, H. Liu, C. Song, and Z. Wasilewski, "Background-limited terahertz quantum-well photodetector," *Applied Physics Letters*, vol. 86, no. 23, p. 231103, 2005.

[45] B. Ferguson and X.-C. Zhang, "Materials for terahertz science and technology," *Nature materials*, vol. 1, no. 1, pp. 26–33, 2002.

[46] J. R. Tucker and M. J. Feldman, "Quantum detection at millimeter wavelengths," *Reviews of Modern Physics*, vol. 57, no. 4, p. 1055, 1985.

[47] E. L. Kollberg, "Microwave and millimeter-wave mixers," *New York, IEEE Press, 1984, 432 p. No individual items are abstracted in this volume.*, vol. 1, 1984.

[48] P. H. Siegel, "A planar log-periodic mixtenna for millimeter and submillimeter wavelengths," in *Microwave Symposium Digest, 1986 IEEE MTT-S International*. IEEE, 1986, pp. 649–652.

[49] B. J. Clifton, "Schottky diode receivers for operation in the 100-1000 ghz region," *Radio and Electronic Engineer*, vol. 49, no. 7, pp. 333–346, 1979.

[50] M. C. Gaidis, H. M. Pickett, C. Smith, S. C. Martin, R. P. Smith, and P. H. Siegel, "A 2.5-thz receiver front end for spaceborne applications," *Microwave Theory and Techniques, IEEE Transactions on*, vol. 48, no. 4, pp. 733–739, 2000.

[51] S. Weinreb and A. R. Kerr, "Cryogenic cooling of mixers for millimeter and centimeter wavelengths," *Solid-State Circuits, IEEE Journal of*, vol. 8, no. 1, pp. 58–63, 1973.

[52] G. Dolan, T. Phillips, and D. Woody, "Low-noise 115-ghz mixing in superconducting oxide-barrier tunnel junctions," *Applied Physics Letters*, vol. 34, no. 5, pp. 347–349, 1979.

[53] A. H. Dayem and R. J. Martin, "Quantum interaction of microwave radiation with tunneling between superconductors," *Phys. Rev. Lett.*, vol. 8, pp. 246–248, 1962.

[54] M. A. Barychev, "Superconductor-Insulator-Superconductor THz Mixer Integrated with a Superconducting Flux-Flow Oscillator," ph.D. Thesis, Technische Universiteit Delft,The Netherlands.

[55] G. M. Rebeiz, "Millimeter-wave and terahertz integrated circuit antennas," *Proceedings of the IEEE*, vol. 80, no. 11, pp. 1748–1770, 1992.

[56] N. Nishioka, P. Richards, and D. Woody, "Composite bolometers for submillimeter wavelengths," *Applied optics*, vol. 17, no. 10, pp. 1562–1567, 1978.

[57] S. M. Wentworth and D. P. Neikirk, "Composite microbolometers with tellurium detector elements," *Microwave Theory and Techniques, IEEE Transactions on*, vol. 40, no. 2, pp. 196–201, 1992.

[58] D. Neikirk, W. W. Lam, and D. Rutledge, "Far-infrared microbolometer detectors," *International journal of infrared and millimeter waves*, vol. 5, no. 3, pp. 245–278, 1984.

[59] D. M. Slocum, E. J. Slingerland, R. H. Giles, and T. M. Goyette, "Atmospheric absorption of terahertz radiation and water vapor continuum effects," *Journal of Quantitative Spectroscopy and Radiative Tryinganfer*, vol. 127, pp. 49–63, 2013.

[60] S. P. Voinigescu, A. Tomkins, E. Dacquay, P. Chevalier, J. Hasch, A. Chantre, and B. Sautreuil, "A study of sige hbt signal sources in the 220–330-ghz range," *Solid-State Circuits, IEEE Journal of*, vol. 48, no. 9, pp. 2011–2021, 2013.

[61] U. Pfeiffer, E. Ojefors, A. Lisauskas, and H. Roskos, "Opportunities for silicon at mmwave and terahertz frequencies," in *Bipolar/BiCMOS Circuits and Technology Meeting, 2008. BCTM 2008. IEEE.* IEEE, 2008, pp. 149–156.

[62] Y.-C. Ou and G. M. Rebeiz, "On-chip slot-ring and high-gain horn antennas for millimeter-wave wafer-scale silicon systems," *IEEE Trans. Microw. Theory Techniques*, vol. 59, no. 8, pp. 1963–1972, Aug. 2011.

[63] ——, "Differential microstrip and slot-ring antennas for millimeter-wave silicon systems," *IEEE Trans. Antennas Propag.*, vol. 60, no. 6, pp. 2611–2619, June 2012.

[64] K.-H. Tsai, L.-K. Yeh, P.-C. Kuo, and H.-R. Chuang, "Design of 60-ghz cpw-fed cmos on-chip integrated antenna-filter," in *Antennas and Propagation (EuCAP), 2010 Proceedings of the Fourth European Conference on.* IEEE, 2010, pp. 1–3.

[65] W. E. Kock, "Metallic delay lenses," *Bell System Technical Journal*, vol. 27, no. 1, pp. 58–82, 1948.

[66] W. H. Syed and A. Neto, "Front-to-back ratio enhancement of planar printed antennas by means of artificial dielectric layers," *IEEE Trans. Antennas Propag.*, vol. 61, no. 11, pp. 5408–5416, Nov. 2013.

[67] R. E. Collin, *Field theory of guided waves*, ser. IEEE/OUP series on electromagnetic wave theory. New York: IEEE Press, 1991.

[68] S. C. Saha, J. P. Grant, Y. Ma, A. Khalid, F. Hong, and D. R. Cumming, "Terahertz frequency-domain spectroscopy method for vector characterization of liquid using an artificial dielectric," *Terahertz Science and Technology, IEEE Transactions on*, vol. 2, no. 1, pp. 113–122, 2012.

[69] J. Zhang, P. Ade, P. Mauskopf, L. Moncelsi, G. Savini, and N. Whitehouse, "New artificial dielectric metamaterial and its application as a terahertz antireflection coating," *Applied optics*, vol. 48, no. 35, pp. 6635–6642, 2009.

[70] T. LaRocca, J.-C. Liu, and M.-C. Chang, "60 ghz cmos amplifiers using transformer-coupling and artificial dielectric differential transmission lines for compact design," *Solid-State Circuits, IEEE Journal of*, vol. 44, no. 5, pp. 1425–1435, 2009.

[71] N. Llombart, A. Neto, G. Gerini, and P. de Maagt, "Planar circularly symmetric ebg structures for reducing surface waves in printed antennas," *Antennas and Propagation, IEEE Transactions on*, vol. 53, no. 10, pp. 3210–3218, 2005.

[72] A. Neto, N. Llombart, G. Gerini, and P. De Maagt, "On the optimal radiation bandwidth of printed slot antennas surrounded by ebgs," *Antennas and Propagation, IEEE Transactions on*, vol. 54, no. 4, pp. 1074–1083, 2006.

[73] S. Raman and G. M. Rebeiz, "Single- and dual-polarized millimeter-wave slot-ring antennas," *IEEE Trans. Antennas Propag.*, vol. 44, no. 11, pp. 1438–1444, Nov. 1996.

[74] S. Raman, N. S. Barker, and G. M. Rebeiz, "A W-band dielectric-lens-based integrated monopulse radar receiver," vol. 46, no. 12, pp. 2308–2316, Dec. 1998.

[75] D. F. Filipovic, S. S. Gearhart, and G. Rebeiz, "Double-slot antennas on extended hemispherical and elliptical silicon dielectric lenses," *IEEE Trans. Microw. Theory Techniques*, vol. 41, no. 10, pp. 1738–1749, Oct. 1993.

[76] D. Cavallo, W. H. Syed, and A. Neto, "Closed-form analysis of artificial dielectric layers-Part I: Properties of a single layer under plane-wave incidence," *IEEE Trans. Antennas Propag.*, vol. 62, no. 12, Dec. 2014.

[77] ——, "Closed-form analysis of artificial dielectric layers-Part II: Extension to multiple layers and arbitrary illumination," *IEEE Trans. Antennas Propag.*, vol. 62, no. 12, Dec. 2014.

[78] T. Makita, I. Tamai, and S. Seki, "Coplanar waveguides on high-resistivity silicon substrates with attenuation constant lower than 1 db/mm for microwave and millimeter-wave bands," *IEEE Trans. Electron Devices*, vol. 58, no. 3, pp. 709–715, Mar. 2011.

[79] C. Schollhorn, W. Zhao, M. Morschbach, and E. Kasper, "Attenuation mechanisms of aluminum millimeter-wave coplanar waveguides on silicon," *IEEE Trans. Electron Devices*, vol. 50, no. 3, pp. 740–746, Mar. 2003.

[80] V. Ziebart, O. Paul, and H. Baltes, "Strongly buckled square micromachined membranes," *Microelectromechanical Systems, Journal of*, vol. 8, no. 4, pp. 423–432, 1999.

[81] M. J. Pelk, "Near field characterization of integrated antenna's at (sub)/mm-wave frequencies," in *Workshop WFS06 (EuMC/EuMIC) silicon characterization from MHz to THz*, vol. 90, no. 60, 2010, p. 30.

[82] G. F. Engen and C. A. Hoer, "Thru-reflect-line: An improved technique for calibrating the dual six-port automatic network analyzer," *IEEE Trans. Microw. Theory Techniques*, vol. 27, no. 12, pp. 987–993, Dec. 1979.

[83] S. Pan, F. Caster, P. Heydari, and F. Capolino, "A 94-GHz extremely thin metasurface-based bicmos on-chip antenna," *IEEE Trans. Antennas Propag.*, vol. 62, no. 9, pp. 4439–4451, Sept. 2014.

[84] S. Pan, L. Gilreath, P. Heydari, and F. Capolino, "Investigation of a wideband BiCMOS fully on-chip W -band bowtie slot antenna," *IEEE Antennas and Wireless Propag. Letters,*, vol. 12, pp. 706–709, June 2013.

[85] J. J. Lee, E. M. Ferren, D. P. Woollen, and K. M. Lee, "Near-field probe used as a diagnostic tool to locate defective elements in an array antenna," *IEEE Trans. Antennas Propag.*, vol. 36, no. 6, pp. 884–889, June 1988.

[86] G. Zhao, R. Schouten, N. Van der Valk, W. T. Wenckebach, and P. Planken, "Design and performance of a thz emission and detection setup based on a semi-insulating gaas emitter," *Review of Scientific Instruments*, vol. 73, no. 4, pp. 1715–1719, 2002.

[87] G. Pandraud, P. French, and P. Sarro, "Pecvd silicon carbide waveguides for multichannel sensors," in *Sensors, 2007 IEEE.* IEEE, 2007, pp. 395–398.

[88] B. Arango *et al.*, "Pecvd sic photonic crystal sensor," *2011 IEEE SENSORS Proceedings*, pp. 367–370, 2011.

[89] B. Morana, F. Santagata, L. Mele, M. Mihailovic, G. Pandraud, J. Creemer, and P. Sarro, "A silicon carbide mems microhotplate for nanomaterial characterization in tem," in *Micro Electro Mechanical Systems (MEMS), 2011 IEEE 24th International Conference on.* IEEE, 2011, pp. 380–383.

[90] P. M. Sarro, "Silicon carbide as a new mems technology," *Sensors and Actuators A: Physical*, vol. 82, no. 1, pp. 210–218, 2000.

[91] V. Rajaraman, L. Pakula, H. Pham, P. Sarro, and P. French, "Robust wafer-level thin-film encapsulation of microstructures using low stress pecvd silicon carbide," in *Micro Electro Mechanical Systems, 2009. MEMS 2009. IEEE 22nd International Conference on.* IEEE, 2009, pp. 140–143.

[92] M. Mehregany and C. A. Zorman, "Sic mems: opportunities and challenges for applications in harsh environments," *Thin Solid Films*, vol. 355, pp. 518–524, 1999.

[93] A. F. Flannery, N. J. Mourlas, C. W. Storment, S. Tsai, S. H. Tan, J. Heck, D. Monk, T. Kim, B. Gogoi, and G. T. Kovacs, "Pecvd silicon carbide as a chemically resistant material for micromachined transducers," *Sensors and Actuators A: Physical*, vol. 70, no. 1, pp. 48–55, 1998.

[94] C. Fung and J. Kopanski, "Thermal oxidation of 3c silicon carbide single-crystal layers on silicon," *Applied Physics Letters*, vol. 45, no. 7, pp. 757–759, 1984.

[95] G. Fiorentino, B. Morana, S. Forte, and P. M. Sarro, "Role of atomic layer deposited aluminum oxide as oxidation barrier for silicon based materials," *Journal of Vacuum Science & Technology A*, vol. 33, no. 1, p. 01A142, 2015.

[96] M. Mukherjee, N. Mazumder, and S. K. Roy, "Photosensitivity analysis of gallium nitride and silicon carbide terahertz impatt oscillators: comparison of theoretical reliability and study on experimental feasibility," *Device and Materials Reliability, IEEE Transactions on*, vol. 8, no. 3, pp. 608–620, 2008.

[97] F. Roozeboom, A. Kemmeren, J. Verhoeven, F. Van den Heuvel, J. Klootwijk, H. Kretschman, T. Frič, E. Van Grunsven, S. Bardy, C. Bunel *et al.*, "Passive and heterogeneous integration towards a si-based system-in-package concept," *Thin Solid Films*, vol. 504, no. 1, pp. 391–396, 2006.

[98] F. Roozeboom, J. Klootwijk, J. Verhoeven, E. van den Heuvel, W. Dekkers, S. Heil, H. van Hemmen, R. van de Sanden, E. Kessels, F. Le Cornec *et al.*, "Ald options for si-integrated ultrahigh-density decoupling capacitors in pore and trench designs," *ECS Transactions*, vol. 3, no. 15, pp. 173–181, 2007.

[99] P. Simon and Y. Gogotsi, "Materials for electrochemical capacitors," *Nature materials*, vol. 7, no. 11, pp. 845–854, 2008.

[100] Z. Yang, J. Zhang, M. C. Kintner-Meyer, X. Lu, D. Choi, J. P. Lemmon, and J. Liu, "Electrochemical energy storage for green grid," *Chemical Reviews*, vol. 111, no. 5, pp. 3577–3613, 2011.

[101] P. Sharma and T. Bhatti, "A review on electrochemical double-layer capacitors," *Energy Conversion and Management*, vol. 51, no. 12, pp. 2901–2912, 2010.

[102] B. Conway, V. Birss, and J. Wojtowicz, "The role and utilization of pseudocapacitance for energy storage by supercapacitors," *Journal of Power Sources*, vol. 66, no. 1, pp. 1–14, 1997.

[103] A. S. Aricò, P. Bruce, B. Scrosati, J.-M. Tarascon, and W. Van Schalkwijk, "Nanostructured materials for advanced energy conversion and storage devices," *Nature materials*, vol. 4, no. 5, pp. 366–377, 2005.

[104] C. Shen, X. Wang, W. Zhang, and F. Kang, "A high-performance three-dimensional micro supercapacitor based on self-supporting composite materials," *Journal of Power Sources*, vol. 196, no. 23, pp. 10 465–10 471, 2011.

[105] S. Boukhalfa, K. Evanoff, and G. Yushin, "Atomic layer deposition of vanadium oxide on carbon nanotubes for high-power supercapacitor electrodes," *Energy & Environmental Science*, vol. 5, no. 5, pp. 6872–6879, 2012.

[106] G. Fiorentino, S. Vollebregt, F. Tichelaar, R. Ishihara, and P. M. Sarro, "3d solid-state supercapacitors obtained by ald coating of high-density carbon nanotubes bundles," in *Micro Electro Mechanical Systems (MEMS), 2014 IEEE 27th International Conference on*. IEEE, 2014, pp. 342–345.

[107] D. Vega, J. Reina, R. Pavón, and A. Rodríguez, "High-density capacitor devices based on macroporous silicon and metal electroplating," 2014.

[108] A. Bajolet, J. Giraudin, C. Rossato, L. Pinzelli, S. Bruyère, S. Cremer, T. Jagueneau, P. Delpech, L. Montès, and G. Ghibaudo, "Three-dimensional 35 nf/mm 2 mim capacitors integrated in bicmos technology," in *Solid-State Device Research Conference, 2005. ESSDERC 2005. Proceedings of 35th European*. IEEE, 2005, pp. 121–124.

[109] J. I. Sohn, Y.-S. Kim, C. Nam, B. Cho, T.-Y. Seong, and S. Lee, "Fabrication of high-density arrays of individually isolated nanocapacitors using anodic aluminum oxide templates and carbon nanotubes," *Applied Physics Letters*, vol. 87, no. 12, p. 123115, 2005.

[110] A. Cortés, C. Celedón, P. Ulloa, D. Kepaptsoglou, and P. Häberle, "Capacitance of a highly ordered array of nanocapacitors: Model and microscopy," *Journal of Applied Physics*, vol. 110, no. 10, p. 104312, 2011.

[111] C. Marichy and N. Pinna, "Carbon-nanostructures coated/decorated by atomic layer deposition: Growth and applications," *Coordination Chemistry Reviews*, vol. 257, no. 23, pp. 3232–3253, 2013.

[112] "Technology Backgrounder: Atomic Layer Deposition." 2IC Knowledge LLC, 24 April 06.

[113] S. M. George, "Atomic layer deposition: an overview," *Chemical reviews*, vol. 110, no. 1, pp. 111–131, 2009.

[114] "International Technology Roadmap for Semiconductors."

[115] O. Sneh, R. B. Clark-Phelps, A. R. Londergan, J. Winkler, and T. E. Seidel, "Thin film atomic layer deposition equipment for semiconductor processing," *Thin Solid Films*, vol. 402, no. 1, pp. 248–261, 2002.

[116] "Atomic Layer Deposition cambridge nanotech,2006." http://http://www.cambridgenanotech.com.

[117] G. Chen, S. Bandow, E. Margine, C. Nisoli, A. Kolmogorov, V. H. Crespi, R. Gupta, G. Sumanasekera, S. Iijima, and P. Eklund, "Chemically doped double-walled carbon nanotubes: cylindrical molecular capacitors," *Physical review letters*, vol. 90, no. 25, p. 257403, 2003.

[118] S. Vollebregt, R. Ishihara, J. Derakhshandeh, J. van der Cingel, H. Schellevis, and C. Beenakker, "Integrating low temperature aligned carbon nanotubes as vertical interconnects in si technology," in *Nanotechnology (IEEE-NANO), 2011 11th IEEE Conference on*. IEEE, 2011, pp. 985–990.

[119] F. Tuinstra and J. L. Koenig, "Raman spectrum of graphite," *The Journal of Chemical Physics*, vol. 53, no. 3, pp. 1126–1130, 1970.

[120] P. Kumar, M. K. Wiedmann, C. H. Winter, and I. Avrutsky, "Optical properties of al< sub> 2</sub> o< sub> 3</sub> thin films grown by atomic layer deposition," *Applied optics*, vol. 48, no. 28, pp. 5407–5412, 2009.

[121] P. Patsalas and S. Logothetidis, "Optical, electronic, and transport properties of nanocrystalline titanium nitride thin films," *Journal of Applied Physics*, vol. 90, no. 9, pp. 4725–4734, 2001.

[122] H. Tiznado and F. Zaera, "Surface chemistry in the atomic layer deposition of tin films from ticl4 and ammonia," *The Journal of Physical Chemistry B*, vol. 110, no. 27, pp. 13 491–13 498, 2006.

[123] C. Ahn, S. Cho, H. Lee, K. Park, and S. Jeong, "Characteristics of tin thin films grown by ald using ticl4 and nh3," *Metals and Materials International*, vol. 7, no. 6, pp. 621–625, 2001.

[124] M. Vasile, A. Emerson, and F. Baiocchi, "The characterization of titanium nitride by x-ray photoelectron spectroscopy and rutherford backscattering," *Journal of Vacuum Science & Technology A*, vol. 8, no. 1, pp. 99–105, 1990.

[125] U. Diebold and T. Madey, "Tio2 by xps," *Surface Science Spectra*, vol. 4, no. 3, pp. 227–231, 1996.

[126] B. J. Hinds, N. Chopra, T. Rantell, R. Andrews, V. Gavalas, and L. G. Bachas, "Aligned multiwalled carbon nanotube membranes," *Science*, vol. 303, no. 5654, pp. 62–65, 2004.

[127] M. Groner, J. Elam, F. Fabreguette, and S. M. George, "Electrical characterization of thin al< sub> 2</sub> o< sub> 3</sub> films grown by atomic layer deposition on silicon and various metal substrates," *Thin Solid Films*, vol. 413, no. 1, pp. 186–197, 2002.

[128] J. Elam, D. Routkevitch, P. Mardilovich, and S. George, "Conformal coating on ultrahigh-aspect-ratio nanopores of anodic alumina by atomic layer deposition," *Chemistry of Materials*, vol. 15, no. 18, pp. 3507–3517, 2003.

[129] T. Mayer, J. Elam, S. George, P. Kotula, and R. Goeke, "Atomic-layer deposition of wear-resistant coatings for microelectromechanical devices," *Applied Physics Letters*, vol. 82, no. 17, pp. 2883–2885, 2003.

[130] L. F. Hakim, D. M. King, Y. Zhou, C. J. Gump, S. M. George, and A. W. Weimer, "Nanoparticle coating for advanced optical, mechanical and rheological properties," *Advanced Functional Materials*, vol. 17, no. 16, pp. 3175–3181, 2007.

Summary

High aspect-ratio MEMS devices for the next generation of THz/MHz passive components

The realization of efficient passive devices directly on chip represents one of the most intriguing challenges in IC fabrication processes. The performance of such devices are intrinsically determined by physical parameters that cannot be easily scaled, making the on-chip integration of such components a complex task to solve.

To pursue the envisioned scaling towards the realization of more compact and fast electronic devices, it is then clear that new, engineered materials and innovative device architectures have to be explored.

The aim of this dissertation is to provide the technological means to implement the fabrication of two particular type of passive components, integrated Terahertz (THz) planar antennas and solid state supercapacitors.

The first part of this thesis is dedicated to the realization of an efficient THz planar antenna, directly on chip. The realization of more efficient sensing devices working in the THz range of frequencies open the possibilities to exploit the enormous bandwith available for communication purposes. Moreover, an extremely large amount of physical phenomena can be explored by using this radiation, such as for cosmic back-ground radiation and molecular spectroscopy. However the sensing devices employed for these applications suffer from poor performance due to limited radiation efficiency and the lack of efficient power sources. These topics are discussed in **Chapter 2**.

As most relevant scientific contribution of this work, a new engineered anisotropic material, called Artificial Dielectric Layer (ADL) working in the THz frequencies is introduced in **Chapter 3**. By embedding a periodic

array of squared metal patches into a conventional dielectric host matrix, we demonstrate that it is possible to obtain a new material with high and anisotropic dielectric constant.

When placed on top a conventional planar antenna, this material enhances the front-to-back ratio of more than 10 dB, with almost no power dispersed in surface waves.

Due to scaling of the ADL parameters with the frequency, PCB technologies cannot be used to fabricate this component (and the antenna itself). For this reason we decided to employ integrated circuits fabrication technologies. This choice permits the possibility to use the large variety of materials available in a integrated circuits (IC) laboratory for the fabrication.

The use of different materials, with tunable mechanical properties, is fundamental to the realization of the antenna/ADL structure. This device basically consists of a large suspended membrane in which both the antenna and the ADL are integrated. Due to the high aspect ratio of the device, the stress of the deposited layers is tuned to achieve only minor buckling effects. Numerical simulations of ADL mechanical properties have been performed, showing that is possible to predict the deformation of the membrane by creating an effective layer that resembles the metal/oxide composite structure. With this technique, the computational time required to simulate the post-releasing buckling has been drastically reduced, while preserving a very good accuracy in the deformations calculation.

In **Chapter 4** the measurements of the ADL properties are reported. By measuring the antenna radiation pattern and the relative gain, the effectiveness of this material is demonstrated. As independent technique to confirm the obtained results, the ADL optical properties have also been investigated also by using a Time Domain Spectroscopy system.

In **Chapter 5** an alternative version of the ADL is proposed. As dielectric host material a layer of Silicon Carbide is used instead of the conventional silicon oxide. This choice allows a consistent reduction in the ADL final thickness, with obvious benefit for manufacturability.

In the first part of this thesis, it has been shown that a new, composite high aspect-ratio metamaterial for THz applications can be realized by using conventional IC technologies. The potential of this approach can be exploited also in the fabrication of other passive devices. In the second part of this thesis it is indeed shown that high aspect-ratio composite nanostructures can be used as to build a new generation of fully solid state supercapacitors.

In **Chapter** 6 the concept of supercapacitor is introduced and the applications in the IC industry discussed. Nowadays these components are

widely used in System in Package integration, as decoupling filters. Moreover, with the increasing demand of large power supply directly on chip, as for harvester and mobile systems, there is a growing interest in efficient and good performing integrated supercapacitors.

In **Chapter 7** a new type of nanostructured supercapacitor is discussed. This device is based on the use of metallic carbon nanotubes (CNTs) as high aspect-ratio nanoelectrodes. By coating these nanostructures with a dielectric and conductive layer, both deposited by Atomic Layer Deposition (ALD), the electrode surface area is greatly enhanced, leading to very large capacitance values.

The capacitor performance is evaluated by electrical impedance measurements. By fitting the obtained data with an analytical device model, the relevant capacitor parameters are extracted. As major scientific result, the presented devices retail their capacitance in a wide range of frequencies (1 Hz - 1 MHz), while similar devices presented by other groups fails already at 10 KHz.

To evaluate the coating of the CNTs by the ALD layers, high-resolution TEM analysis of the coated structures is performed. Moreover, the diffusion of the gas ALD precursors into the porous CNTs bundles is studied in detail, demonstrating that the coating efficiency decreases drastically after a depth of 400 nm. The obtained capacitance values are in a very good agreement with this theoretical model. Finally, the dielectric breakdown of the devices is studied, showing that the premature breaking at 1.1 Volt can be reasonably accountable to defects in the dielectric coating on the CNTs.

Samenvatting

Hoge aspectverhouding MEMS voor de volgende generatie van THz / MHz passieve componenten

Het realiseren van efficiënte passieve componenten direct op de chip is een van de meest intrigerende uitdagingen in IC fabricageprocessen. De eigenschappen van zulke apparaten zijn intrinsiek bepaald door fysieke parameters die niet eenvoudig kunnen worden geschaald. Dit maakt de op-chip integratie van deze componenten een complexe taak om op te lossen.

Om het beoogde schaling, voor de realisatie van compacter en snellere elektronische apparatuur, te behalen is het duidelijk dat nieuw ontwikkelde materialen en innovatieve apparaat constructies moeten worden onderzocht.

Het doel van dit proefschrift is het leveren van technologische middelen voor de fabricage van twee bepaalde soorten passieve componenten: geÃŕntegreerde terahertz (THz) vlakke antennes en vaste-stof supercondensatoren.

Het eerste deel van dit proefschrift is toegewijd aan de realisatie van een efficiënte THz vlakke antenne, direct op de chip. Het realiseren van efficiëntere sensoren werkzaam in het THz frequentiegebied, opent de mogelijkheid om de enorme bandbreedte, beschikbaar voor communicatiedoeleinden, te benutten. Bovendien kan een zeer grote hoeveelheid fysische verschijnselen worden onderzocht met deze straling, zoals kosmische achtergrondstraling en moleculaire spectroscopie. Helaas lijden de sensorapparatuur gebruikt voor deze toepassingen onder slechte eigenschappen vanwege de beperkte stralingsefficiäntie en het gebrek aan efficiënte vermogensbronnen. Deze onderwerpen worden besproken in **Hoofdstuk 2**.

Als de meeste relevante wetenschappelijke bijdrage aan dit werk, wordt een nieuw ontworpen anisotroop materiaal, de zogenaamde kunstmatige

diëlektrische laag (ADL) werkzaam in de THz frequenties geÃŕntroduceerd in **Hoofdstuk 3**. Door het inbedden van een periodieke reeks van vierkante metalen stukken in een conventionele diëlektrische gastheer matrix, tonen wij aan dat het mogelijk is om een nieuw materiaal te verkrijgen met een hoge en anisotropische diëlektrische constante.

Wanneer dit boven een gebruikelijke vlakke antenne is geplaatst, verhoogt dit materiaal de front-to-back-verhouding met meer dan 10 dB, met vrijwel geen stroom verspreidt in oppervlaktegolven.

Door het schalen van de ADL parameters met frequentie, kan PCB technologie niet worden gebruikt om deze component (en de antenne zelf) te fabriceren. Om deze reden hebben we besloten om geÃŕntegreerde-schakelingsfabricatietechnologieën te gebruiken. Deze keuze maakt het mogelijk om de grote verscheidenheid van materialen in een geÃŕntegreerde schakeling (IC) laboratorium voor de vervaardiging te gebruiken.

Het gebruik van verschillende materialen, met instelbare mechanische eigenschappen, is fundamenteel voor de verwezenlijking van de antenne / ADL structuur. Dit apparaat bestaat in principe uit een groot opgehangen membraan waarin zowel de antenne als de ADL is geÃŕntegreerd. Vanwege de hoge aspectverhouding van het apparaat, is de spanning van de gedeponeerde lagen afgestemd zodat alleen geringe knik effecten verkregen zijn. Numerieke simulaties van de mechanische eigenschappen van de ADL zijn uitgevoerd. Deze tonen aan dat het mogelijk is de vervorming van het membraan te voorspellen door het creëren van een effectieve laag die lijkt op het metaal/oxide samengestelde structuur. Met deze techniek is de rekentijd, die nodig is voor de simulatie van de verlossingsbuiging, drastisch verminderd met behoud van een zeer goede nauwkeurigheid in de vervormingsberekening.

In **Hoofdstuk 4** worden de metingen van de ADL eigenschappen gerapporteerd. Door het meten van de antenne stralingspatroon en de relatieve versterking wordt de effectiviteit van dit materiaal aangetoond. Als onafhankelijke techniek om de verkregen resultaten te bevestigen, zijn de optische eigenschappen van de ADL ook onderzocht met een tijddomeinspectroscopiesysteem.

In **Hoofdstuk 5** wordt een alternatieve versie van de ADL voorgesteld. Als diëlektrisch gastheermateriaal wordt een laag siliciumcarbide gebruikt in plaats van de gebruikelijke siliciumoxide. Deze keuze staat een consequente vermindering van de uiteindelijke dikte van de ADL toe, met duidelijke voordelen voor de produceerbaarheid.

In het eerste deel van dit proefschrift is aangetoond dat een nieuw samengestelde hoge aspectverhouding metamaterial voor THz doeleinden gerealiseerd kan worden door de toepassing van gebruikelijke IC technieken.

Deze methode kan ook worden benut bij de fabricage van andere passieve apparaten. In het tweede deel van het proefschrift wordt aangetoond dat hoge aspectverhouding van composiet nanostructuren kan worden gebruikt om een nieuwe generatie volledige vaste-stof- supercondensatoren te bouwen.

In **Hoofdstuk 6** wordt het begrip supercondensator geÃŕntroduceerd en de toepassingen in de IC industrie besproken. Tegenwoordig worden deze componenten veelal gebruikt in System-in-Package -integratie als ontkoppelingsfilters. Bovendien, met de toenemende vraag naar een grote voeding direct op de chip, zoals voor energie oogst-en mobiele systemen, is er een groeiende belangstelling voor efficiënte en goed presterende geÃŕntegreerde supercondensatoren.

In **Hoofdstuk 7** wordt een nieuw type nanogestructureerde supercondensator besproken. Dit apparaat is gebaseerd op het gebruik van metallische koolstofnanobuizen (CNTs) als hoge aspectverhouding nanoelectrodes. Door het bekleden van deze nanostructuren met een diëlectrische en geleidende laag, beide gedeponeerd met atomische laagdepositie (ALD), is het elektrodeoppervlaktegebied sterk vergroot, wat leidt tot zeer grote capaciteitswaarden.

De condensator wordt beoordeeld door elektrische impedantiemetingen. Door het passen van de verkregen gegevens met een analytische apparaatmodel, worden de relevante parameters van de condensator gewonnen. Als belangrijke wetenschappelijk resultaat, liggen de capaciteit van de voorgestelde apparaten in een breed frequentiegebied (1 Hz - 1 MHz), terwijl soortgelijke apparaten door andere groepen niet functioneren bij 10 KHz.

Om de bekleding van de CNTs door ALD lagen te evalueren, is een hoge resolutie TEM analyse van de beklede structuur uitgevoerd. Bovendien wordt de diffusie van het ALD voorlopergas in de poreuze CNT bundels in detail bestudeerd. Er wordt aangetoond dat het bekledingsvermogen drastisch daalt na een diepte van 400 nm. De verkregen condensatorwaarden zijn in een zeer goede overeenkomst met dit theoretisch model. Ten slotte wordt de diëlektrische doorslag van de apparaten bestudeerd, waaruit blijkt dat de voortijdige breuk van 1,1 Volt redelijkerwijs veroorzaakt wordt door defecten in de diëlektrische bekleding op de CNTs.

Journal Publications

[1] G. Fiorentino, S. Vollebregt, F. Tichelaar, R. Ishihara, and P. M. Sarro, "Impact of the atomic layer deposition precursors diffusion on solid-state carbon nanotube based supercapacitors performances," *Nanotechnology*, vol. 26, no. 6, p. 064002, 2015.

[2] W. H. Syed, G. Fiorentino, D. Cavallo, M. Spirito, P. M. Sarro, and A. Neto, "Design, fabrication and measurements of a 0.3 thz on-chip double sot antenna enhanced by artificial dielectrics," *IEEE Transactions on THz Science and Technology*, vol. Accepted for publication, 2015.

[3] G. Fiorentino, B. Morana, S. Forte, and P. M. Sarro, "Role of atomic layer deposited aluminum oxide as oxidation barrier for silicon based materials," *Journal of Vacuum Science & Technology A*, vol. 33, no. 1, p. 01A142, 2015.

[4] F. Buja, G. Fiorentino, J. Kokorian, and M. van Spengen, "Observation of nanoscale adhesion, friction and wear between ald al2o3 coated silicon mems sidewalls," *Nanotechnology*, vol. In press, 2015.

[5] B. Morana, R. H. Poelma, G. Fiorentino, J. Wei, J. F. Creemer, and P. M. Sarro, "Stiction-induced sealing of surface micromachined channels," *Microelectromechanical Systems, Journal of*, vol. 23, no. 2, pp. 459–470, 2014.

[6] F. Santagata, C. Farriciello, G. Fiorentino, H. Van Zeijl, C. Silvestri, G. Zhang, and P. Sarro, "Fully back-end tsv process by cu electro-less

plating for 3d smart sensor systems," *Journal of Micromechanics and Microengineering*, vol. 23, no. 5, p. 055014, 2013.

Conference proceedings

[1] G. Fiorentino, W. Syed, A. Adam, A. Neto, and P. Sarro, "Artificial dielectric layer based on pecvd silicon carbide for terahertz sensing applications," *Procedia Engineering*, vol. 87, pp. 1497–1500, 2014.

[2] G. Fiorentino, S. Vollebregt, F. Tichelaar, R. Ishihara, and P. M. Sarro, "3d solid-state supercapacitors obtained by ald coating of high-density carbon nanotubes bundles," in *Micro Electro Mechanical Systems (MEMS), 2014 IEEE 27th International Conference on.* IEEE, 2014, pp. 342–345.

[3] C. Silvestri, B. Morana, G. Fiorentino, S. Vollebregt, G. Pandraud, F. Santagata, G. Q. Zhang, and P. M. Sarro, "Cnt bundles growth on microhotplates for direct measurement of their thermal properties," in *Micro Electro Mechanical Systems (MEMS), 2014 IEEE 27th International Conference on.* IEEE, 2014, pp. 48–51.

[4] W. Syed, G. Fiorentino, D. Cavallo, M. Spirito, A. Neto, and P. Sarro, "Enhancement of front to back ratio of on chip antenna by artificial dielectrics at 300 ghz," in *Infrared, Millimeter, and Terahertz waves (IRMMW-THz), 2014 39th International Conference on.* IEEE, 2014, pp. 1–2.

[5] ——, "Front-to-back ratio enhancement of on-chip antenna using artificial dielectrics at 300 ghz," in *Radio Science Meeting (Joint with AP-S Symposium), 2014 USNC-URSI.* IEEE, 2014, pp. 140–140.

[6] G. Fiorentino, W. Syed, F. Santagata, M. Spirito, G. Pandraud, A. Neto, P. Sarro, and A. Adam, "A cmos-compatible metamaterial to enhance the front to back radiation ratio in terahertz antenna for sensing application," in *SENSORS, 2013 IEEE*. IEEE, 2013, pp. 1–4.

[7] B. Morana, G. Fiorentino, G. Pandraud, J. Creemer, and P. Sarro, "Ald aluminum oxide as protective coating against oxidation of lpcvd sic microhotplates," in *Micro Electro Mechanical Systems (MEMS), 2013 IEEE 26th International Conference on*. IEEE, 2013, pp. 484–487.

[8] D. Iero, F. G. Della Corte, G. Fiorentino, P. M. Sarro, and B. Morana, "Heat flux-based sensor for the measurement of the power dissipated by switching devices," in *Applied Measurements for Power Systems (AMPS), 2013 IEEE International Workshop on*. IEEE, 2013, pp. 19–23.

[9] ——, "Heat flux sensor for power loss measurements of switching devices," in *Thermal Investigations of ICs and Systems (THERMINIC), 2013 19th International Workshop on*. IEEE, 2013, pp. 327–330.

[10] G. Fiorentino, S. Vollebregt, R. Ishihara, and P. M. Sarro, "Multilayer conformal coating of highly dense multi-walled carbon nanotubes bundles," in *Nanotechnology (IEEE-NANO), 2012 12th IEEE Conference on*. IEEE, 2012, pp. 1–5.

[11] F. Santagata, G. Fiorentino, M. Nie, and P. Sarro, "Fully back-end tsv process by cu electro-less plating for 3d smart sensor systems," in *IEEE Sensor 2012*, 2012, p. 4.

Acknowledgements

As every long story goes to an end, I would like to close this book and my PhD with the best end possible. And the only way I see is to mention and thanks all the people that have been present in my life during these four years. No man is an island (*cit. J. Donne*), and while being far away from home, you learn it in many way, sometimes the toughest possible.

The first person I would like to thank is my promotor and supervisor, Prof. Lina Sarro. I remember four years ago when I arrived at your office for the first time, barely knowing anything about the group, TU-Delft and what would have been my project. You choosed to give me a chance and I am really grateful for it. For my part, I can truly say that having the honor of being part of your group and moving here to Netherlands, changed me in a better person, professionally and humanly. I can state to be among the luckiest PhD student I ever met, if not the luckiest one.

During these years you inspired my work every day, in every idea I was developing, with your smartness, wisdom, patience and trust in my capabilities. Even in the difficult moments, you always showed me the bright side of what was happening and to never, ever, give up. This has been one of the most important lesson I have ever learned. You always surprised me with your ability of understanding in few seconds very complex problems, a quality that I have never found in other scientists. You are the one that can always find five minutes for anybody, even though this would cost you to stay till evening in your office (practically every day). This is something I will never forget.

You have been a model to follow, a person to be inspired, a great mind. No words can truly express my gratitude for the time I have been your student. I hope that during my career there will be still a chance to collaborate

on new ideas and projects. Grazie!

When I began this project, it was clear from the very first moment that there was the need for a strong theoretical background work on electromagnetic field propagations. During these years, there have been moments in which the light was completely gone, the complexity of the problem was almost too great, simply nothing like this was never ever tried before. But in these moments, there was a person always ready to envision new scenarios, new possible applications, new way to solve problems, truly at the edge of the known science. This has been for me Prof. A. Neto. You have been my (not official) second supervisor in these amazing project and thanks to you I discover a complete new world, new fascinating problems and challenges. I remember the inspiring talks we had together, the challenging meeting while the antenna design was on going and finally your compliments when everything was working perfectly. Thanks to your ideas we complete an outstanding job widely recognized by the Terahertz scientific community and I am incredibly proud of being part of it.

The first non-Professor I would like here to mention here is the person that for four years worked with me on this project, developing the theoretical part of it, Waqas H. Syed. I have rarely met such a gentle and smart guy in my life. Working with you on this project has been a privilege. I learned a lot from your approach to life problems, your optimism and patience. Your skills will make you fly high in the scientific community, I am truly convinced about that. Thank you my friend, my colleague and fellow for all the amazing moments passed during this quest.

For all the time spent during the measurements sessions, the patience in designing together the best device, the long time requested for the post processing of the data, I have to deeply thank Prof. Marco Spirito and Prof. Aurele Adam. Thanks to your efforts, we demonstrate the potential of the IC fabrication technology for antenna THz applications and I am sure that more still has to come!

It is definitively for me important to mention my French colleague and friend, Dr. Gregory Pandraud. You are the person that can do thousands and thousands of fabrication process together, the *we-can-do-this* man. Having you as active part of the MEMS group and DIMES during these years made me a better researcher. I learned from you a straightforward approach to the problem solving and also how to push my limits a bit further to realize projects and ideas I would never thought I was able to do. Thanks Greg, you are a great person and friend and I will never forget all the time we spent together working on crazy ideas.

As the fabrication of the device here presented was accomplished in a high technology laboratory such as the DIMES (now ELK), it is manda-

tory to mention the amazing work done by the technicians and scientific personnel to support me and all the PhD students during the years of the doctorate. It would be impossible here to mention all the DIMES people I have been working with, all the funny and precious moments spent with all of you. Thank you guys and girls !!

However, among all of them I want to mention explicitly J.M.W. Laros, although I simply refer to him as SuperMario. During these years I can truly say that without his help and patience, the difficult etching and deposition process would have not been possible. I remember the late night in cleanroom while fixing all the possible tools. It was an outstanding example of job devotion and I will never thank you enough.

These years have been great because I worked with the best group I have ever met, but also because out of the University I could count on my family and on a solid group of friends, the one I have always wished to have.

First of all I want to thank my special paranymphs, Silvia and Cinzia. You have been my precious friends during my time spent here in Netherlands. I can not really explain how important was for me to know that you both were here when I needed. I hope I have been a good shoulder during these years. There will be always a place in my mind for both of you.

Among all the people I met, I have to mention my precious friend, valid colleague and crazy housemate, Federico Buja. Usually, we all meet our best friends during our youth and we continue attending them all life. Well, luckily, this rule has been broken, because late in my life I met a true friend, a person as good and gentle as I have never seen before. We passed through crazy adventures literally all over Netherlands and Europe. All the time spent with you made me a better person and I will never thank you enough.

Moving from the North, heading back to the deep Sicily, here I found Bruno Morana. A colleague of the MEMS group, one the most serious researcher I have ever met in my life, a person with a big heart. You teached me a lot of cleanroom secrets and tricks, it would have taken years for me to discover. Out of University, in Rotterdam, Hoevestraat 4, we did legendary parties, people will talk for years to come. Europe is large, we have to party still in many places !

Out of university after your PhD, now introduced in the evil banking world, my friend and housemate, Daniele Romano, it is now your turn. Thank you man, for all the time spend together, for the discussions we made on politics, for all the dinner prepared together for random friends coming in the weekend! You will move soon to Amsterdam, but the three of us, you, me and Federico created an indissoluble friendship and I am sure we will meet as soon as we can.

And moving to the end I can not forget a person I met during an amazing

trip in California, Massimiliano. Although you are now living quite far in Stuttgart, we write each other almost every day. I have been inspired by your strength, by your visionary talks and by your ability to explain complex concepts in a very simple way, even when at the edge of the known science. My friend over the Europe, I can not say how grateful I am to have met you.

A special thank goes to a valuable PhD student of the ECTM department, Miki Trifunovic, to be the patient translator of my summary and propositions. You literally saved me, so thanks a lot!

I would like to write more and more on this, but I see that time and space are flying out so : Andrea, the Marcos, Cristina, Thamar, Luigi, Agata, Sten, Rene, Violeta, Yelena, Silvana, Johan, Daniele...guys, thank you all.

Grazie Mamma e Papá. Grazie Luca, Paola e Ornella, my beloved brother and sisters. For your patience, your inesaurible strength. I would not be here without your support, your help, your inspiration. I may not be the most present son and brother, but I always have you all in my mind.

And thank you reader, to be so patient and come to this end. I will take live from you by wishing all the best in the best way I know : the Vulcan salute :

Live long and prosper.

Giuseppe Fiorentino, Naples, 19 May 2015.